

AN INVESTIGATION OF THE SOURCE OF THE FAR INFRARED  
RADIATION IN SPIRAL GALAXIES USING NEAR INFRARED HYDROGEN  
RECOMBINATION LINES AS A PROBE OF STAR FORMATION

By

LAUREN V. JONES

A DISSERTATION PRESENTED TO THE GRADUATE SCHOOL  
OF THE UNIVERSITY OF FLORIDA IN PARTIAL FULFILLMENT  
OF THE REQUIREMENTS FOR THE DEGREE OF  
DOCTOR OF PHILOSOPHY

UNIVERSITY OF FLORIDA

2000

Copyright 2000

by

Lauren V. Jones

This dissertation is dedicated to

my Mother,

my Nana

and

Lucy

## ACKNOWLEDGEMENTS

I am especially grateful to my mother for her continued support in any endeavor I choose to undertake.

I would like to thank my advisor, Richard Elston, for his guidance and support.

I am grateful to my graduate committee members for their comments and suggestions which have improved the final version of this work.

I would like to thank the Department of Astronomy for supporting me as a graduate teaching assistant.

I would like to thank the College of Liberal Arts and Sciences for awarding me a Dissertation Fellowship.

This work was supported by NASA in the form of a Graduate Student Research Program Fellowship from 1996-1999.

The National Optical Astronomy Observatories supported travel to and accommodations for all observations at Kitt Peak National Observatory and Cerro Tololo InterAmerican Observatory.

The National Science Foundation supported travel to Siding Spring Observatory for observations related to this dissertation. Accommodations there were provided by the University of New South Wales.

I would also like to thank the following people for their advice, support and friendship: Tarek Monowar, Katherine Wu, Joanna Levine, Tim Spahr, Karl Haisch, Pimol Moth, Beth Holmes, Elisha Polomski, Barbara Eckstein, Debbie Elmegreen, Michelle Wampler, Jenny Robinson, and Lisa Stevak.

## TABLE OF CONTENTS

ACKNOWLEDGEMENTS . . . . .	iv
LIST OF TABLES . . . . .	viii
LIST OF FIGURES . . . . .	x
ABSTRACT . . . . .	xiv
CHAPTERS	
1 INTRODUCTION . . . . .	1
1.1 Background . . . . .	1
1.2 The General Interstellar Radiation Field . . . . .	2
1.3 Previous Work on the Problem . . . . .	3
1.4 The Near Infrared Solution . . . . .	6
1.5 Objectives of This Study . . . . .	6
1.6 The Sample . . . . .	7
1.7 Observations . . . . .	9
1.8 Expected Results and Analysis . . . . .	9
1.9 Summary . . . . .	11
2 OBSERVATIONS . . . . .	13
2.1 Near Infrared Data . . . . .	13
2.1.1 Brackett Gamma Data . . . . .	14
2.1.2 Paschen Beta Data . . . . .	16
2.2 Optical Data . . . . .	19
2.2.1 The $H\alpha$ Data . . . . .	19
2.2.2 The [SII] Data . . . . .	23
2.2.3 The [OIII] Data . . . . .	26
2.2.4 The $H\beta$ data . . . . .	28
2.3 Far Infrared Data . . . . .	28
2.4 Ultraviolet Data . . . . .	31
3 DATA REDUCTION . . . . .	33
3.1 Near Infrared Data . . . . .	33
3.1.1 Linearization . . . . .	33
3.1.2 Darks . . . . .	35
3.1.3 Flats . . . . .	36
3.1.4 Sky Subtraction . . . . .	36

3.1.5	Masks . . . . .	37
3.1.6	Object Frames . . . . .	37
3.1.7	Standard Stars and Calibration . . . . .	38
3.2	Optical Data . . . . .	39
3.2.1	Kitt Peak MOSAIC Imager . . . . .	39
3.2.2	Cerro Tololo TEK 2K CCD . . . . .	39
3.2.3	Calibration and Standard Stars . . . . .	40
3.3	Far Infrared Data . . . . .	40
3.3.1	The Pixon Method . . . . .	41
3.4	Uniformity of Data from Different Wavelength Regimes . . . . .	46
4	ANALYSIS . . . . .	50
4.1	The Energy Budget . . . . .	50
4.1.1	Basic Formulation . . . . .	50
4.1.2	Model Populations . . . . .	51
4.1.3	Extinction Models . . . . .	52
4.1.4	Extinction Correction . . . . .	53
4.1.5	Comparison of Star Formation Indicators . . . . .	57
4.1.6	Bolometric Population Correction . . . . .	58
4.2	Aperture Photometry . . . . .	62
5	RESULTS . . . . .	63
5.1	NGC 2403 . . . . .	63
5.2	NGC 6946 . . . . .	73
5.3	NGC 300 . . . . .	80
5.4	NGC 628 . . . . .	87
5.5	NGC 1068 . . . . .	93
5.6	NGC 4725 . . . . .	102
5.7	NGC 3359 . . . . .	109
5.8	NGC 4535 . . . . .	117
6	DISCUSSION . . . . .	122
6.1	Comparison of Results With Previous Works . . . . .	122
6.1.1	Agreement . . . . .	123
6.1.2	Contradiction . . . . .	126
6.2	Summary of Our Results . . . . .	127
7	CONCLUSIONS . . . . .	135
7.1	Possible Sources of Error and Bias . . . . .	137
7.2	Improvements for Future Work . . . . .	139
APPENDICES		
A	NEAR INFRARED REDUCTION IMAGES . . . . .	140
B	OPTICAL REDUCTION IMAGES . . . . .	148

C APERTURES . . . . .	152
REFERENCES . . . . .	159
BIOGRAPHICAL SKETCH . . . . .	162

## LIST OF TABLES

1.1	The Sample . . . . .	8
1.2	Data for the Sample . . . . .	9
2.1	Standard Stars and Exposure Times for Near Infrared Data . . . . .	17
2.2	Signal-to-Noise Estimates . . . . .	18
2.3	Standard Stars and Exposure Times for Optical Data . . . . .	29
2.4	Signal-to-Noise Estimates . . . . .	30
3.1	Resolution of FIR Bands . . . . .	46
3.2	Resolution of Optical Bands . . . . .	48
3.3	Resolution of Other Optical Bands . . . . .	48
3.4	Resolution of Near Infrared Bands . . . . .	49
4.1	Correlation Coefficients . . . . .	60
4.2	Values of $N_A$ Relative to $N_{LyC}$ . . . . .	60
5.1	Positions and Fluxes for NGC 2403 . . . . .	64
5.2	Extinctions for NGC 2403 . . . . .	67
5.3	Population Ratios for NGC 2403 . . . . .	69
5.4	Positions and Fluxes for NGC 6946 . . . . .	74
5.5	Extinctions for NGC 6946 . . . . .	76
5.6	Population Ratios for NGC 6946 . . . . .	78
5.7	Positions and Fluxes for NGC 300 . . . . .	81
5.8	Extinctions for NGC 300 . . . . .	83



5.9	Population Ratios for NGC 300 . . . . .	85
5.10	Positions and Fluxes for NGC 628 . . . . .	88
5.11	Extinctions for NGC 628 . . . . .	90
5.12	Population Ratios for NGC 628 . . . . .	91
5.13	Positions and Fluxes for NGC 1068 . . . . .	95
5.14	Extinctions for NGC 1068 . . . . .	98
5.15	Population Ratios for NGC 1068 . . . . .	100
5.16	Positions and Fluxes for NGC 4725 . . . . .	103
5.17	Extinctions for NGC 4725 . . . . .	105
5.18	Population Ratios for NGC 4725 . . . . .	107
5.19	Positions and Fluxes for NGC 3359 . . . . .	110
5.20	Extinctions for NGC 3359 . . . . .	113
5.21	Population Ratios for NGC 3359 . . . . .	115
5.22	Positions and Fluxes for NGC 4535 . . . . .	117
5.23	Extinctions for NGC 4535 . . . . .	119
5.24	Population Ratios for NGC 4535 . . . . .	119
6.1	Energy Balance Analysis Using Global Extinction . . . . .	129
6.2	Summary Table Part 1 . . . . .	130
6.3	Summary Table Part 2 . . . . .	131

## LIST OF FIGURES

2.1	KPNO Br $\gamma$ and 2.14 $\mu$ m Filter Transmission Curves . . . . .	14
2.2	CTIO Br $\gamma$ and 2.14 $\mu$ m Filter Transmission Curves . . . . .	15
2.3	KPNO Pa $\beta$ and $J$ Filter Transmission Curves . . . . .	16
2.4	KPNO $R$ and H $\alpha$ Filter Transmission Curves used by Sharp . . . . .	19
2.5	KPNO H $\alpha$ Filter Transmission Curve used by Jacoby . . . . .	20
2.6	OdRd1M $R$ and H $\alpha$ Filter Transmission Curves . . . . .	20
2.7	CTIO $R$ and H $\alpha$ Filter Transmission Curves . . . . .	21
2.8	KPNO $R$ and H $\alpha$ Filter Transmission Curves . . . . .	21
2.9	KPNO [SII] and [SII] off Filter Transmission Curves . . . . .	23
2.10	CTIO [SII] and [SII] off Filter Transmission Curves . . . . .	24
2.11	KPNO [OIII] and [OIII] off Filter Transmission Curves used by Sharp . . . . .	24
2.12	KPNO [OIII] and [OIII] off Filter Transmission Curves used by Ciardullo, et al. . . . .	25
2.13	CTIO [OIII] and [OIII] off Filter Transmission Curves . . . . .	25
2.14	KPNO H $\beta$ and $B$ Filter Transmission Curves used by Sharp . . . . .	27
2.15	KPNO H $\beta$ Filter Transmission Curve used by Jacoby . . . . .	27
2.16	UIT Near Ultraviolet Filter Transmission Curves . . . . .	31
2.17	UIT Far Ultraviolet Filter Transmission Curves . . . . .	32
3.1	Linearity Sequence Plot . . . . .	34
4.1	Population Models . . . . .	52

4.2	Extinction Models . . . . .	53
4.3	$A_V$ plots for NGC 2403 - Cardelli Model . . . . .	58
4.4	$A_V$ plots for NGC 2403 - Calzetti Model . . . . .	59
5.1	$\frac{[SiII]}{H\alpha}$ Plot for NGC 2403 . . . . .	63
5.2	$\frac{[OIII]}{H\alpha}$ Plot for NGC 2403 . . . . .	63
5.3	Hydrogen Line Ratios for NGC 2403 . . . . .	65
5.4	Hydrogen Line Ratios vs. Distance for NGC 2403 . . . . .	66
5.5	Star Formation Rates for NGC 2403 . . . . .	68
5.6	Population vs. Color Temperature for NGC 2403 . . . . .	70
5.7	Color Temperature vs. Distance for NGC 2403 . . . . .	70
5.8	Luminosity Functions for NGC 2403 . . . . .	71
5.9	$\frac{[OIII]}{H\alpha}$ Plot for NGC 6946 . . . . .	73
5.10	Hydrogen Line Ratios for NGC 6946 . . . . .	75
5.11	Hydrogen Line Ratios vs. Distance for NGC 6946 . . . . .	75
5.12	Star Formation Rates for NGC 6946 . . . . .	77
5.13	Population Ratios vs. Color Temperatures for NGC 6946 . . . . .	79
5.14	Color Temperature vs. Distance for NGC 6946 . . . . .	79
5.15	Luminosity Function for NGC 6946 . . . . .	79
5.16	$\frac{[SiII]}{H\alpha}$ Ratios for NGC 300 . . . . .	80
5.17	$\frac{[OIII]}{H\alpha}$ Ratios for NGC 300 . . . . .	80
5.18	Hydrogen Line Ratio vs. Distance for NGC 300 . . . . .	82
5.19	Star Formation Rates for NGC 300 . . . . .	84
5.20	Population Ratio vs. Color Temperature for NGC 300 . . . . .	86
5.21	Color Temperature vs. Distance for NGC 300 . . . . .	86
5.22	Luminosity Function for NGC 300 . . . . .	86
5.23	$\frac{[SiII]}{H\alpha}$ Plot for NGC 628 . . . . .	87
5.24	$\frac{[OIII]}{H\alpha}$ Plot for NGC 628 . . . . .	87

5.25 Hydrogen Line Ratio vs. Distance for NGC 628 . . . . .	89
5.26 Star Formation Rates for NGC 628 . . . . .	89
5.27 Population Ratio vs. Color Temperature for NGC 628 . . . . .	92
5.28 Color Temperature vs. Distance for NGC 628 . . . . .	92
5.29 Luminosity Function for NGC 628 . . . . .	93
5.30 $\frac{[OIII]}{H\alpha}$ Plot for NGC 1068 . . . . .	94
5.31 Hydrogen Line Ratios for NGC 1068 . . . . .	96
5.32 Hydrogen Lines Ratios vs. Distance for NGC 1068 . . . . .	97
5.33 Star Formation Rates for NGC 1068 . . . . .	99
5.34 Population Ratio vs. Color Temperature for NGC 1068 . . . . .	101
5.35 Color Temperature vs. Distance for NGC 1068 . . . . .	101
5.36 Luminosity Functions for NGC 1068 . . . . .	101
5.37 Hydrogen Line Ratios for NGC 4725 . . . . .	102
5.38 Hydrogen Line Ratios vs. Distance for NGC 4725 . . . . .	104
5.39 Star formation Rates for NGC 4725 . . . . .	106
5.40 Population Ratio vs. Color Temperature for NGC 4725 . . . . .	108
5.41 Color Temperature vs. Distance for NGC 4725 . . . . .	108
5.42 Luminosity Function for NGC 4725 . . . . .	108
5.43 Hydrogen Line Ratios for NGC 3359 . . . . .	111
5.44 Hydrogen Line Ratios vs. Distance for NGC 3359 . . . . .	112
5.45 Star Formation Rates for NGC 3359 . . . . .	114
5.46 Population Ratio vs. Color Temperature for NGC 3359 . . . . .	116
5.47 Color Temperature vs. Distance for NGC 3359 . . . . .	116
5.48 Luminosity Functions for NGC 3359 . . . . .	116
5.49 Hydrogen Line Ratio vs. Distance for NGC 4535 . . . . .	118
5.50 Star Formation Rates for NGC 4535 . . . . .	120
5.51 Population Ratio vs. Color Temperature for NGC 4535 . . . . .	120

5.52 Color Temperature vs. Distance for NGC 4535 . . . . .	120
5.53 Luminosity Function for NGC 4535 . . . . .	121
A.1 Dark Frame . . . . .	140
A.2 Dark Mask Frame . . . . .	141
A.3 Flat Frame . . . . .	142
A.4 Flat Mask Frame . . . . .	143
A.5 Mask Frame . . . . .	144
A.6 Sky Frame . . . . .	145
A.7 Raw Frame . . . . .	146
A.8 Final Frame . . . . .	147
B.1 Bias Frame . . . . .	148
B.2 Flat Frame . . . . .	149
B.3 Raw Frame . . . . .	150
B.4 Final Frame . . . . .	151
C.1 Apertures for NGC 2403 . . . . .	152
C.2 Apertures for NGC 6946 . . . . .	153
C.3 Apertures for NGC 300 . . . . .	153
C.4 Apertures for NGC 628 . . . . .	154
C.5 Apertures for NGC 1068 . . . . .	155
C.6 Apertures for NGC 4725 . . . . .	156
C.7 Apertures for NGC 3359 . . . . .	157
C.8 Apertures for NGC 4535 . . . . .	158

Abstract of Dissertation Presented to the Graduate School  
of the University of Florida in Partial Fulfillment of the  
Requirements for the Degree of Doctor of Philosophy

AN INVESTIGATION OF THE SOURCE OF THE FAR INFRARED  
RADIATION IN SPIRAL GALAXIES USING NEAR INFRARED HYDROGEN  
RECOMBINATION LINES AS A PROBE OF STAR FORMATION

By

Lauren V. Jones

August 2000

Chairman: Dr. Richard J. Elston  
Major Department: Astronomy

The focus of this project is to determine whether or not far infrared radiation can be used as a direct indicator of present star formation. To do this we will study the nature of the heating sources of dust grains responsible for far infrared radiation. Specifically, we have obtained, for a small sample of galaxies, narrow-band observations in the near infrared regime and broad-band observations in the far infrared regime. The near infrared data were obtained from ground-based observatories around the world. The near infrared narrow-band imaging covers the Brackett Gamma ( $\lambda = 2.1650 \mu\text{m}$ ) and Paschen Beta ( $\lambda = 1.2818 \mu\text{m}$ ) recombination lines of hydrogen. The hydrogen lines serve as tracers of the location and rate of present star formation. The far infrared data are in the form of IRAS observations in the  $60 \mu\text{m}$  and  $100 \mu\text{m}$  regimes. In addition to these data, we have obtained optical  $\text{H}\alpha$ ,  $\text{H}\beta$ , ultraviolet, [OIII] and [SII] images to verify that the near infrared narrowband images are, in fact, tracing star formation and not some other physical process in

the interstellar medium. The analysis of these data involves a comparison of spatial correlations and the energy budget of the near infrared and far infrared data for the sample galaxies.

## CHAPTER 1 INTRODUCTION

### 1.1 Background

Far infrared ( $\lambda = 40\mu\text{m} - 120\mu\text{m}$ ) radiation is emitted by interstellar dust particles which are heated by stellar radiation. For many galaxies, the far infrared dominates the bolometric radiation; therefore, it is an important key to understanding the physical processes (e.g., star formation) occurring in galaxies. The heating processes of far infrared-emitting dust grains in the cases of active or starbursting galaxies are reasonably well understood; however, questions remain regarding these processes in the disks of normal galaxies far from star formation regions. A central question is what stellar populations are heating the dust in various regions of a galaxy's disk?

At first, it was thought that all far infrared radiation originated from dust heated by ultraviolet radiation. Since ultraviolet radiation comes primarily from young (OB) stars, far infrared radiation was thought to be a star formation indicator (Rieke & Lebofsky 1979; Telesco & Harper 1980). Shortly after the Infrared Astronomical Satellite (IRAS) data became available, it was noted that a significant amount of the far infrared radiation originating in our Galaxy was coming from a diffuse infrared source, now known as cirrus (Low et al. 1984; Boulanger & Perault 1988; Bothun, Lonsdale and Rice 1989; and references therein). Cirrus is a wispy diffuse component of far infrared emission seen nearly everywhere in our Galaxy; it is interstellar dust heated by the general interstellar radiation field. In the solar vicinity, cirrus emission is estimated to contribute 70% of the total far infrared radiation from the disk (Boulanger & Perault 1988).



## 1.2 The General Interstellar Radiation Field

The interstellar radiation field (ISRF) heats the cirrus which is a major component of the local far infrared radiation. Mathis, Mezger & Panagia 1983 (hereafter, MMP) describe the components of the ISRF as follows: (1) ultraviolet ( $0.09\mu\text{m}$  -  $0.25\mu\text{m}$ ) radiation from early type (main sequence OBA) stars modeled from observations of the interstellar ultraviolet radiation (from Gondhalekar et al. 1980), (2) visible radiation from middle-aged disk stars (main sequence FG) simulated by blackbody radiation from a source with temperature 7500 K with dilution factor  $10^{-14}$ , (3) visible radiation from older disk stars (main sequence KM and dwarf stars) simulated by blackbody radiation from a source with temperature 4000 K with dilution factor  $10^{-13}$ , and (4) optical and near infrared radiation from Red Giants simulated by blackbody radiation from a source with temperature 3000 K with dilution factor  $4 \times 10^{-13}$ . (The dilution factor accounts for the fact that the ISRF is far from the stellar sources.) In the solar vicinity, the ultraviolet radiation comprises 60% (see Tables A3 and B1 of MMP) of the ISRF (96% of which is from the young stellar component).

Clearly what comprises the ISRF varies considerably with position in a galaxy. Near OB associations or H II regions, we expect the ISRF to be dominated by UV radiation from the youngest stellar populations. However, far from such regions, the ISRF must be more dilute. So, one can say that far infrared radiation from cirrus heated by the ISRF is primarily *not* associated with recent star formation (in the last  $10^7$  years), provided it is far from regions of ongoing star formation.

Mezger, Mathis & Panagia (1982) predicted that, to a distant observer, our Galaxy would have 90% of its far infrared emission originating in its disk at distances beyond 4 kpc from its center. Boulanger & Perault (1988) hold that two thirds of the far infrared radiation in the solar neighborhood is due to “young” stars ( $< a$  few  $10^8$  years old) heating local dust. Extrapolating the conclusion of Boulanger

& Perault (1988) to the entire disk of the Galaxy and employing the conclusion of Mezger, Mathis & Panagia (1982), this implies that nearly 60% of the total far infrared radiation from the Galaxy is due to stars younger than a few  $10^8$  years. This implies that far infrared radiation is *not* a good indicator of *recent* star formation (occurring  $\leq 10^7$  years ago).

On the other hand, Walterbos & Greenawalt (1996) claim that about 50% of the far infrared radiation in normal spiral galaxies can be attributed to the ISRF. Further, they state that ultraviolet photons from OB stars which become part of the ISRF will account for not more than 25% of the far infrared radiation. They assert that the contribution to the ISRF by OB stars depends on the wavelength being considered, the recent and past star formation history, the Initial Mass Function and the metallicity of the stars. They investigate a general case (see their Appendix) and show that although ionizing stars contribute about 50% of the ultraviolet component of the ISRF, these stars can account for only about 27% of the  $60\mu\text{m}$  emission and 20% of the  $100\mu\text{m}$  emission from dust heated only by the ISRF. This calculation is made assuming the models of Desert, Boulanger & Puget (1990) for the emission expected in the IRAS bands of  $60\mu\text{m}$  and  $100\mu\text{m}$  for dust heated by an ISRF with the same color as the ISRF in the solar neighborhood. The analysis of Walterbos & Greenawalt (1996), therefore, attributes *75% of the far infrared radiation to ultraviolet radiation from OB stars*, via the ISRF ( $\approx 25\%$ ) or directly ( $\approx 50\%$ ). Such an analysis indicates that far infrared radiation *may* be a good indicator of present star formation.

### 1.3 Previous Work on the Problem

The question of which stellar populations are heating the dust in various regions of a galaxy's disk has been addressed using both global and spatial methods. Each method tests mainly whether the far infrared radiation has one or two different dust temperature components. The warm component is associated with recent star formation processes (i.e., dust in compact H II regions or in diffuse extended

H II regions heated by stars younger than a few  $10^8$  years). The cold component is associated with cirrus-like emission (dust heated by an interstellar radiation field dominated by old disk stars).

The global method (cf., Young et al. 1984; Lonsdale Persson & Helou 1987; Jones & Zasov 1995; and references therein) involves a search for statistically significant correlations among global (integrated over the whole galaxy) properties representative of different-aged stellar populations (i.e., H $\alpha$  emission to trace ongoing star formation, broad band optical emission to trace old populations, 21-cm emission to trace neutral hydrogen gas which is not uniquely associated with star formation on the global scale, and CO emission to trace molecular gas which is associated with star formation processes). This type of analysis is performed on a large, multi-wavelength sample of galaxies. Comparing the results to known correlations in various types of astrophysical sources (e.g., H II regions), conclusions are drawn about the age of the stellar population heating the dust. Since this method is applied to the entire galaxy, it may not uniquely determine the contributions from the various sources. It is expected that the heating source of the far infrared-emitting dust is different in different regions of a galaxy. The global analysis might indicate which is the dominant heating source, but if that changes with time or within a galaxy, the results may be difficult to interpret. Another problem with the global method of analysis is that correlations may be related to the size of the galaxy and not the physical processes producing far infrared radiation.

The spatial method (cf., Walterbos & Schwing 1987; Devereux & Scowen 1994; Jones & Keel 2000; and references therein) involves a search for spatial correlations among emission components representative of different-aged stellar populations (e.g., H $\alpha$  for the ongoing star formation population, near-ultraviolet for the recent star formation population, and broad band optical for the old population). This type of analysis can only be performed on galaxies of large angular size due to the limited

resolution of the far infrared data. A comparison is made between the input energy (derived from  $H\alpha$ , optical or near-ultraviolet fluxes, assuming some global extinction law) and the output energy (taken from far infrared flux) in a given resolved region of a galaxy. For example, a region which has a larger  $H\alpha$ /far infrared ratio than optical/far infrared or near-ultraviolet/far infrared ratio is assumed to be powered by the stellar source related to  $H\alpha$  (OB stars). These ratios are also compared to normal H II regions and cirrus patches in our Galaxy to determine whether the far infrared radiation is primarily related to cirrus or H II regions.

No study can attribute the heating of the far infrared-emitting grains to a single stellar population in all galaxies. In all cases, the best conclusions indicate a *dominant* heating source for some subsample of galaxies. In some galaxies, it appears that the far infrared radiation is primarily associated with regions of star formation, as indicated by ultraviolet and  $H\alpha$  images (Devereux & Scowen 1994), while in other galaxies, the far infrared radiation in some regions seems to originate from sources *other* than star formation regions which *do not* emit primarily in  $H\alpha$  or ultraviolet (Jones & Keel 2000). The disagreement in results can be attributed to (a) the use of star formation indicators (such as ultraviolet emission and  $H\alpha$ ) which are extremely sensitive to extinction due to dust and (b) the use of a global extinction law.

In the  $H\alpha$  and UV regimes, the problem is the large uncertainty in extinction of radiation due to dust. More importantly, the *degree* of extinction *changes* from region to region in our Galaxy (Israel & Kennicutt 1980) and in the Small Magellanic Cloud (SMC) (Caplan et al. 1996) and, therefore, presumably in all galaxies. This variation in extinction occurs on a scale smaller than the resolution of the IRAS data. Thus, it is easy to confuse possible heating sources in a region of a galaxy. The most obvious way to eliminate this problem is to observe star formation indicators in these regions at wavelengths for which the extinction is much smaller. By observing

at longer wavelengths, it is possible to greatly reduce the sensitivity of the data to variations in extinction.

#### 1.4 The Near Infrared Solution

There are several bright hydrogen recombination lines in the near infrared regime that can be used to solve the problem outlined above (e.g.,  $\text{Br}\gamma$ ,  $\lambda = 2.165 \mu\text{m}$ ; and  $\text{Pa}\beta$ ,  $\lambda = 1.2818 \mu\text{m}$ ). The extinction at  $\text{Br}\gamma$  is  $\approx 5.2$  times lower than at  $\text{H}\alpha$ ; at  $\text{Pa}\beta$  it is  $\approx 2.7$  times lower (Scheffler & Elsässer 1988). If we take the visual extinction ( $A_V$ ) due to dust in an H II region as 1.1 magnitudes (N.B. the H II region is therefore optically thick), as in Israel & Kennicutt (1980), this means that, in the  $\text{Br}\gamma$  and  $\text{Pa}\beta$  regimes, the same H II region will be optically thin.

While the near infrared lines experience less extinction, they are not as bright as the  $\text{H}\alpha$  line. Assuming Baker-Menzel case B recombination (Baker & Menzel 1938), a hydrogen column density of  $10^4 \text{ cm}^{-2}$ , and a source temperature of  $10^4 \text{ K}$ , the ratio of  $\text{H}\alpha$  to  $\text{Br}\gamma$  flux is  $\approx 104$ , and the ratio of  $\text{H}\alpha$  to  $\text{Pa}\beta$  flux is  $\approx 17.7$  (Hummer & Storey 1987).

We probe a sample of galaxies (see Table 1.1) using these lines as indicators of star formation as well as measures of extinction. The extinction from our Galaxy is known in the direction of each of the galaxies in our sample (Giovanelli et al. 1995). We have imaged each of the galaxies shown in Table 1.1 in  $\text{Br}\gamma$  and  $\text{H}\alpha$ . Additionally, we have  $\text{Pa}\beta$  and  $\text{H}\beta$  images for some galaxies. Using two or more hydrogen emission lines, we have a measure of both the present star formation rate and the extinction. We use these data to determine whether far infrared radiation is a good star formation indicator for the galaxies in our sample.

#### 1.5 Objectives of This Study

The primary objective of this study is to determine whether far infrared radiation ( $\lambda = 40 \mu\text{m} - 120 \mu\text{m}$ ), derived from  $60 \mu\text{m}$  and  $100 \mu\text{m}$  band IRAS images, is

a reliable star formation indicator in all regions of a normal disk galaxy (of type Sab to Scd). A secondary objective is to learn about the variation of extinction within the disks of galaxies.

We met our objectives by imaging several galaxies using star formation indicators in wavelength bands where extinction due to dust is low compared to that in H $\alpha$  (the usual star formation indicator). We use two or more bands in order to evaluate the extinction in each region. We compare our near infrared images to high resolution ( $\approx 11''$ ) far infrared data. In addition, we correlate the near infrared and far infrared morphologies to determine whether they are spatially coincident. Lastly, we compare the extinguished near infrared flux to the reprocessed far infrared flux to determine whether the near infrared source is responsible for heating the far infrared-emitting dust.

If we find that far infrared radiation is a good star formation indicator, the IRAS and future SIRTf data will become much more useful to those who study star formation in our Galaxy and in other galaxies. In this case, astronomers could use far infrared radiation to compare, on a global scale, the star formation rates in other galaxies to our Galaxy.

## 1.6 The Sample

The main criteria for choosing a sample for this project are (1) the galaxy should be large and close enough that the IRAS data show some structure, (2) the galaxy should be a face-on spiral galaxy with distinct arm and interarm regions so that different heating sources are easily distinguishable, and (3) the galaxy should have been observed by IRAS in the 60  $\mu\text{m}$  and 100  $\mu\text{m}$  bands. Initially, we intended to use data from the Infrared Space Observatory (ISO). For this reason, our sample originally included galaxies which were not observed by IRAS. We eliminated those galaxies and replaced them with others which were available during the observing

Table 1.1: The Sample

Object Name	Right Ascension	Angular Size	m <sub>B</sub>
Morph. Class.	Declination	V <sub>helio</sub> (km/sec)	A <sub>B</sub>
NGC 300	00 <sup>h</sup> 54 <sup>m</sup> 53.5 <sup>s</sup>	21.9 × 15.5	8.95
SA(s)d	-37°41'00"	144 ± 1	0.055
NGC 628	01 <sup>h</sup> 36 <sup>m</sup> 41.7 <sup>s</sup>	10.5 × 9.5	9.95
SA(s)c	+15°46'59"	657 ± 1	0.301
NGC 1068	02 <sup>h</sup> 42 <sup>m</sup> 40.7 <sup>s</sup>	7.1 × 6.0	9.61
(R)SA(rs)b; Sy1 Sy2	-00°00'48"	1137 ± 3	0.145
NGC 2403	07 <sup>h</sup> 36 <sup>m</sup> 51.4 <sup>s</sup>	21.9 × 12.3	8.93
SAB(s)cd	+65°36'09"	131 ± 3	0.172
NGC 3359	10 <sup>h</sup> 46 <sup>m</sup> 36.7 <sup>s</sup>	7.2 × 4.4	11.03
SB(rs)c	+63°13'27"	1014 ± 1	0.036
NGC 4535	12 <sup>h</sup> 34 <sup>m</sup> 20.3 <sup>s</sup>	7.1 × 5.0	10.59
SAB(s)c	+08°11'54"	1961 ± 3	0.084
NGC 4725	12 <sup>h</sup> 50 <sup>m</sup> 26.6 <sup>s</sup>	10.7 × 7.6	10.11
SAB(r)ab pec Sy2	+25°30'06"	1206 ± 3	0.051
NGC 6946	20 <sup>h</sup> 34 <sup>m</sup> 52.3 <sup>s</sup>	11.5 × 9.8	9.61
SAB(rs)cd	+60°09'14"	48 ± 2	1.475

All the data in this table come from the NASA/IPAC Extragalactic Database (NED is operated by the Jet Propulsion Laboratory, California Institute of Technology, under contract with the National Aeronautics and Space Administration). Column (1) lists the NGC number of each object and its morphological classification. Column (2) lists the right ascension and declination of the object (2000.0 equinox). Column (3) lists the angular extent of the object (in arcminutes) and the heliocentric radial velocity of the object. Column (4) lists the apparent blue magnitude and the galactic extinction in the blue band.

Table 1.2: Data for the Sample

Object Name	Bands
NGC 300	[OIII],[OIII]off,R,H $\alpha$ , [SII],[SII]off,2.14 $\mu$ m,Br $\gamma$ , 60 $\mu$ m,100 $\mu$ m
NGC 628	[OIII],[OIII]off,R,H $\alpha$ , [SII],[SII]off,2.14 $\mu$ m,Br $\gamma$ , 60 $\mu$ m,100 $\mu$ m
NGC 1068	B,H $\beta$ , [OIII], V, R, H $\alpha$ , J, Pa $\beta$ , 2.14 $\mu$ m, Br $\gamma$ , 60 $\mu$ m, 100 $\mu$ m
NGC 2403	B,H $\beta$ , [OIII],[OIII]off,R,H $\alpha$ , [SII], J, Pa $\beta$ , 2.14 $\mu$ m, Br $\gamma$ , 60 $\mu$ m, 100 $\mu$ m
NGC 3359	R, H $\alpha$ , J, Pa $\beta$ , 2.14 $\mu$ m, Br $\gamma$ , 60 $\mu$ m, 100 $\mu$ m
NGC 4535	R, H $\alpha$ , 2.14 $\mu$ m, Br $\gamma$ , 60 $\mu$ m, 100 $\mu$ m
NGC 4725	R, H $\alpha$ , J, Pa $\beta$ , 2.14 $\mu$ m, Br $\gamma$ , 60 $\mu$ m, 100 $\mu$ m
NGC 6946	[OIII], V, R, H $\alpha$ , J, Pa $\beta$ , 2.14 $\mu$ m, Br $\gamma$ , 60 $\mu$ m, 100 $\mu$ m

Column (1) lists the NGC number of each object. Column (2) lists the bands in which data were collected for each object.

times we were granted and which met the above criteria. Table 1.1 lists the galaxies which make up our sample.

### 1.7 Observations

We have observed all the galaxies listed in Table 1.2 in the bands indicated. Additionally, we have data in the UV, [SII] 6727 Å and [OIII] 5007 Å bands. The details of the data acquisition are described in Chapter 2.

### 1.8 Expected Results and Analysis

We compare the morphology observed in the Pa $\beta$  and Br $\gamma$  images with that of the 60  $\mu$ m and 100  $\mu$ m regime images. The the Br $\gamma$  images indicate the distribution of ionized hydrogen, while far infrared images show the distribution of heated dust grains. If the source responsible for heating the dust grains is physically the same



as the source responsible for ionizing the hydrogen, we expect that the maps will match spatially, and that the energetics will balance (input and output bolometric luminosity) reflecting a single physical heating source. We do expect a slight offset in spatial coordinates since the dust near H II regions should be hotter than the dust elsewhere. However, the far infrared images should show sources which surround the ionized regions in a fairly clumpy manner since the dust should be located in regions just outside the H II regions. Given our underlying assumption, we do not expect that far infrared-bright regions will extend significantly (1 kiloparsec) beyond regions of ionized hydrogen.

In order to test whether far infrared radiation is a good indicator of present star formation, we will examine the images obtained in  $\text{Br}\gamma$  and  $\text{Pa}\beta$  and compare them to the  $60\ \mu\text{m}$  and  $100\ \mu\text{m}$  images from IRAS. The process of analysis for each object involves several steps:

- identify flux peaks in each of the images
- translate the peaks in each image onto a master and draw from that a set of apertures which does not include duplicates or overlapping apertures
- measure the flux in each aperture on each image
- compare the spatial distribution of flux peaks
- determine the extinction in the near infrared emission bands by comparing ratios of fluxes with expected ratios (e.g., from case B recombination)
- compare energy input (from extinguished flux in near infrared emission bands) to energy output (from far infrared radiation, which is calculated from a combination of the  $60\ \mu\text{m}$  and  $100\ \mu\text{m}$  fluxes).

The details of this analysis are described in Chapter 3.

We expect that our results will show that far infrared radiation can be used as an tracer of present star formation. Even though our sample is relatively small, we are confident that it is representative.

If our assumption is correct and the sources are the same, global far infrared luminosities can be used to extrapolate global star formation rates. Such studies will give astronomers a better understanding of the formation and evolution processes in galaxies. If our assumption is incorrect and the sources are distinguishably different, we must conclude that the source of the far infrared radiation is more complex than previously thought and astronomers would have to reassess their entire understanding of far infrared radiation and dust emission.

### 1.9 Summary

This project is specifically designed to acquire the data needed to answer the question: “What is the source of the energy which powers the far infrared radiation in spiral galaxies?” Eight representative galaxies properly analyzed will allow us to test whether star formation is the dominant source of the far infrared radiation in normal disk galaxies.

This undertaking is important to extragalactic astronomy because it will improve the understanding of the physical process of star formation. In determining whether there is a connection between far infrared radiation and star formation, we will gain insight into the connections between gas and dust in the process of star formation in our Galaxy and other galaxies. If other galaxies vary among themselves in star formation and evolutionary processes, it is important to understand why this is so. This project is also important for the study of star formation and interstellar medium in our own Galaxy because we assume that star formation processes in our Galaxy are not significantly different from other, nearby spiral galaxies.

If our results are inconclusive, they will indicate a complexity in this problem that has, to date, been overlooked. If our analysis proves our assumption, this will

enhance our understanding of the details involved in heating interstellar dust in galaxies. In addition, such a result would confirm the utility of global far infrared properties in the analysis of star formation processes. On the other hand, if our analysis disproves our initial assumption, it will drastically change our understanding of grain-heating processes in galaxies.

## CHAPTER 2 OBSERVATIONS

In this chapter, we describe the observational techniques and sources of the data used in this dissertation project. Also, we describe the instruments and filters used to take the data. A summary of the key points (calibration stars, total exposure times, signal-to-noise obtained) can be found in tables at the end of each section. We present the data by wavelength. The details of the basic data reduction are described in the next chapter, Data Reduction.

### 2.1 Near Infrared Data

The near infrared data were acquired at various locations. A log of filters, locations, dates, exposure times and standard stars is provided in Table 2.1.2. The average signal-to-noise achieved in each image is presented in Table 2.1.2. This was calculated in the following way: the signal is the average of the signal in the smallest aperture taken on the unblurred images at all positions evaluated; the noise is the root mean square in the same sized aperture taken in nearly 100 off-source positions in the image.

The near infrared observations included both on-source and off-source integrations with dithers around both positions. It is necessary to take off-source frames frequently to adequately sample the sky since the sky varies in brightness on a timescale of the order of a few minutes. For point sources it is possible to use the object frame to sample the sky. However, our galaxies are extended objects, so we took off-source frames to sample the sky. Sky sampling is very important in the near infrared regime and will be discussed in more detail in Chapter 3. The main advantage of using the

# KPNO Br $\gamma$ and 2.14 $\mu$ m Filter Transmission Curves

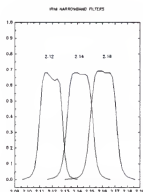


Figure 2.1: The transmission curves for the narrow band filters used on the InfraRed IMager (IRIM) with the 2.1-meter telescope at Kitt Peak National Observatory.

observing method described above is that one avoids having a bright star land on the same place in an image multiple times which can cause oversubtractions in the data reduction. Also, this method allows the bad pixels to move with respect to the source so that the same part of the source does not land on bad pixels all the time.

## 2.1.1 Brackett Gamma Data

The Brackett Gamma (Br $\gamma$ ) data for NGC 4725, NGC 4535, NGC 6946, NGC 1068, NGC 2403, NGC 3359 and NGC 628 were taken at Kitt Peak National Observatory (KPNO) in February 1998, and November 1998, using the Infrared IMager (IRIM) on the 2.1-meter telescope. These data were taken using two narrow band filters. The 2.16 filter and the 2.14 filter (see Figure 2.1). These are 1% filters (they have a width which is 1% of their central wavelength) centered at 2.16  $\mu$ m and 2.14  $\mu$ m, respectively.

IRIM is a wide-field imager which functions in the 1-2.5  $\mu$ m regime. It uses a 256  $\times$  256 HgCdTe NICMOS3 array cooled with LN $_2$ . Used on the 2.1-m telescope at KPNO, the field of view is 280  $\times$  280 arcseconds, with a pixel size of

### CTIO Br $\gamma$ and 2.14 $\mu$ m Filter Transmission Curves

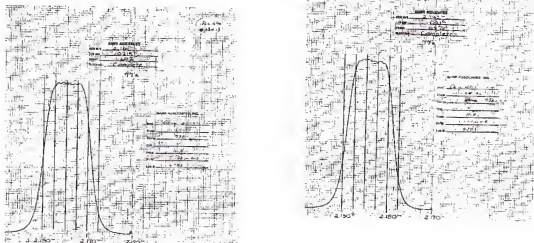


Figure 2.2: The transmission curves for the narrowband filters used on the Cerro Tololo InfraRed IMager (CIRIM) with the 1.5-meter telescope at Cerro Tololo InterAmerican Observatory.

1.09/prime/prime/pixel. The detector array reads out in quadrants and is operated in a double correlated sampling mode which means it performs multiple nondestructive reads both at the end and at the beginning of an integration. This mode of sampling allows the detector to adjust the levels it detects by any offset of charge which may accumulate on the chip between integrations or any charge left on the chip after readout. The sensitivity depends largely on the band in which one operates. At 2.16  $\mu$ m, the signal from a 10.0 magnitude star is 840 ADU/s (where ADU stands for Analog Digital Unit, or counts measured by IRIM), whereas the sky brightness is 50 ADU/s-pixel. This information is not available for the 2.14  $\mu$ m filter.

The Br $\gamma$  data for NGC 300, NGC 628 and NGC 4725 were taken at Cerro Tololo InterAmerican Observatory (CTIO) in July 1998 and December 1998, using the Cerro Tololo InfraRed IMager (CIRIM) on the 1.5-meter telescope. These data were taken using the 2.166w and 2.144w narrow band filters (see Figure 2.2). These are 1% filters centered at 2.166  $\mu$ m and 2.144  $\mu$ m, respectively.

## KPNO $\text{Pa}\beta$ and $J$ Filter Transmission Curves

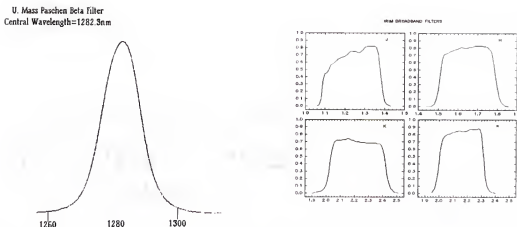


Figure 2.3: The transmission curves for the narrowband filters used on the Infrared Imager (IRIM) with the 2.1-meter telescope at Kitt Peak National Observatory.

CIRIM is CTIO's IRIM; it is the same instrument. Used on the 1.5-m telescope at CTIO at the  $f/8$  focal position, the field of view is  $297 \times 297$  arcseconds, with a pixel size of  $1.16''/\text{pixel}$ . The detector array is also operated using double correlated sampling to reduce its read noise.

Exposure times for all images were 100 seconds. This exposure was chosen because it is the longest possible time allowed between sky frames. Sky subtraction is a serious issue in the regime near  $\text{Br}\gamma$  because of the numerous telluric OH lines which vary in both relative and overall brightness on a timescale of the order of several minutes. More detailed discussion of sky subtraction is in the Data Reduction chapter.

### 2.1.2 Paschen Beta Data

The Paschen Beta ( $\text{Pa}\beta$ ) data for NGC 3359, NGC 4725, NGC 1068, NGC 6946 and NGC 2403 were taken at KPNO in November, 1998 using IRIM. These data were taken using the UMASS  $1.28 \mu\text{m}$  filter and the  $J$  filter (see Figure 2.3). The Paschen Beta filter is centered at  $1.2823 \mu\text{m}$  with a width of  $0.0146 \mu\text{m}$ . The  $J$  filter is centered at  $1.2375 \mu\text{m}$  with a width of  $0.285 \mu\text{m}$ .

Table 2.1: Standard Stars and Exposure Times for Near Infrared Data

Object Name	Filter	Observatory	Date	Exp Time	Standard Star
NGC 300	Br $\gamma$	CTIO	07/98	4800 sec	HD 2811
	Br $\gamma$	CTIO	11/98	4800 sec	HD 19904
	2.14 $\mu$ m	CTIO	07/98	3200 sec	HD 2811
	2.14 $\mu$ m	CTIO	11/98	4800 sec	HD 19904
NGC 628	Br $\gamma$	KPNO	02/98	3200 sec	HD 225023
	Br $\gamma$	KPNO	10/98	4800 sec	HD 225023
	Br $\gamma$	CTIO	11/98	1600 sec	HD 1160
	2.14 $\mu$ m	KPNO	02/98	3200 sec	HD 225023
	2.14 $\mu$ m	KPNO	10/98	4800 sec	HD 225023
	2.14 $\mu$ m	CTIO	11/98	1600 sec	HD 1160
	2.14 $\mu$ m	CTIO	11/98	1600 sec	HD 1160
NGC 1068	Br $\gamma$	KPNO	11/98	3200 sec	HD 22686
	2.14 $\mu$ m	KPNO	11/98	3200 sec	HD 22686
	Pa $\beta$	KPNO	11/98	320 sec	HD 22686
	J	KPNO	11/98	80 sec	HD 22686
NGC 2403	Br $\gamma$	KPNO	02/98	4800 sec	HD 84800
	Br $\gamma$	KPNO	11/98	1600 sec	HD 44612
	2.14 $\mu$ m	KPNO	02/98	4800 sec	HD 84800
	2.14 $\mu$ m	KPNO	11/98	1600 sec	HD 44612
	Pa $\beta$	KPNO	10/98	960 sec	HD 44612
	J	KPNO	10/98	240 sec	HD 44612
NGC 3359	Br $\gamma$	KPNO	01/98	1600 sec	HD 84800
	Br $\gamma$	KPNO	11/98	2400 sec	HD 84800
	2.14 $\mu$ m	KPNO	01/98	1600 sec	HD 84800
	2.14 $\mu$ m	KPNO	11/98	1600 sec	HD 84800
	Pa $\beta$	KPNO	11/98	320 sec	HD 84800
	J	KPNO	11/98	80 sec	HD 84800
NGC 4535	Br $\gamma$	KPNO	02/98	3200 sec	HD 106965
	2.14 $\mu$ m	KPNO	02/98	3200 sec	HD 106965
NGC 4725	Br $\gamma$	CTIO	07/98	4800 sec	HD 101452
	2.14 $\mu$ m	CTIO	07/98	4800 sec	HD 101452
	Pa $\beta$	KPNO	11/98	320 sec	HD 84800
	J	KPNO	11/98	80 sec	HD 84800
NGC 6946	Br $\gamma$	KPNO	10/98	8000 sec	HD 203856
	2.14 $\mu$ m	KPNO	10/98	8000 sec	HD 203856
	Pa $\beta$	KPNO	11/98	320 sec	FS 30
	J	KPNO	11/98	80 sec	FS 30

The columns are as follows: (1) the object name, (2) the filter used, (3), the observatory at which the data were taken, (4) the date (month and year) of the observation, (5) the total on source exposure time, and (6) the standardstar used for calibration.



Table 2.2: Signal-to-Noise Estimates

Object Name	Filter	Exp Time	S/N
NGC 300	Br $\gamma$	9600 sec	205.2
	2.14 $\mu$ m	8000 sec	58.7
NGC 628	Br $\gamma$	9600 sec	166.1
	2.14 $\mu$ m	9600 sec	173.7
NGC 1068	Br $\gamma$	3200 sec	2.4
	2.14 $\mu$ m	3200 sec	2.2
	Pa $\beta$	320 sec	2.2
	J	80 sec	3.7
NGC 2403	Br $\gamma$	6400 sec	60.0
	2.14 $\mu$ m	6400 sec	134.9
	Pa $\beta$	960 sec	60.4
	J	240 sec	46.6
NGC 3359	Br $\gamma$	4000 sec	203.6
	2.14 $\mu$ m	3200 sec	41.9
	Pa $\beta$	320 sec	66.4
	J	80 sec	86.5
NGC 4535	Br $\gamma$	3200 sec	139.6
	2.14 $\mu$ m	3200 sec	116.5
NGC 4725	Br $\gamma$	4800 sec	161.7
	2.14 $\mu$ m	4800 sec	239.2
	Pa $\beta$	320 sec	197.6
	J	80 sec	235.8
NGC 6946	Br $\gamma$	8000 sec	128.9
	2.14 $\mu$ m	8000 sec	148.7

The columns are as follows: (1) the object name, (2) the filter used, (3) the total exposure time of the final image, and (4) the average signal-to-noise achieved in the smallest aperture evaluated; this was calculated by taking the average signal from all positions evaluated in the unblurred images at the smallest aperture size and dividing by the root mean square noise in the smallest of several background apertures.

# KPNO $R$ and $H\alpha$ Filter Transmission Curves used by Sharp

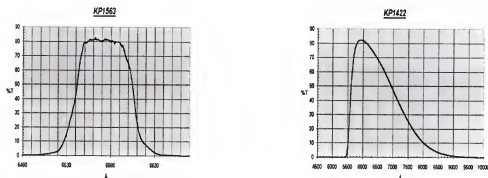


Figure 2.4: The transmission curves for the optical filters used on the CCD MOSAIC imager with the 0.9-meter telescope at Kitt Peak National Observatory for the data taken by Nigel Sharp.

## 2.2 Optical Data

The optical data were taken at several locations by several different observers. As before, the data are divided up by wavelength. In each section we describe the instruments and filters used to take the data. A log of filters, locations, dates, exposure times and standard stars is available in Table 2.3. Table 2.4 lists the average signal-to-noise achieved in each image.

### 2.2.1 The $H\alpha$ Data

The  $H\alpha$  data for NGC 1068 and NGC 6946 were taken at KPNO in November 1998 by Nigel Sharp on the 0.9-meter using the CCD MOSAIC imager. These data were taken using an  $H\alpha$  filter with central wavelength of 6573 Å and full width at half maximum (FWHM) of 67 Å. An  $R$  band filter (central wavelength 6425 Å and FWHM 1541 Å) was used for continuum subtraction. The transmission curves for these filters are shown in Figure 2.4. For NGC 1068 the final  $H\alpha$  image has a total exposure time of 5400 seconds and the final  $R$  band image has a total exposure time

### KPNO $H\alpha$ Filter Transmission Curve used by Jacoby

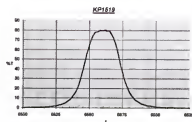


Figure 2.5: The transmission curve for the optical filter used on the CCD MOSAIC imager with the 0.9-meter telescope at Kitt Peak National Observatory for the data taken by George Jacoby.

### OdRdlM $R$ and $H\alpha$ Filter Transmission Curves

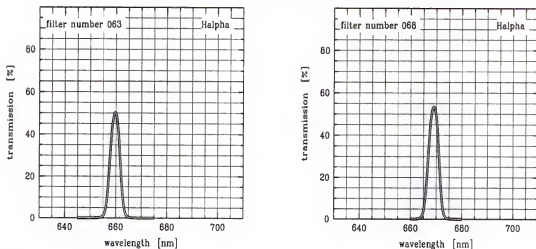


Figure 2.6: The transmission curves for the optical filters used on the Cassegrain Focus CCD imager with the 2.5-meter Isaac Newton Telescope at the Observatorio del Roque de los Muchachos.

### CTIO $R$ and $H\alpha$ Filter Transmission Curves

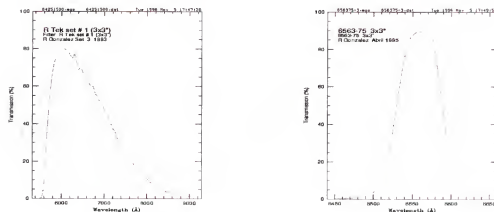


Figure 2.7: The transmission curves for the optical filters used on the Cassegrain Focus CCD imager with the 1.5-meter telescope at Cerro Tololo InterAmerican Observatory.

### KPNO $R$ and $H\alpha$ Filter Transmission Curves

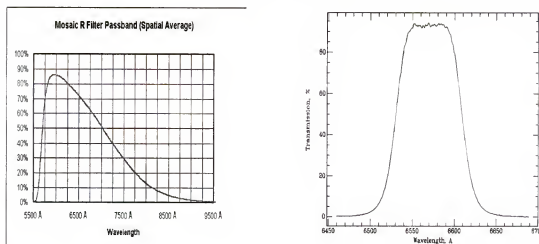


Figure 2.8: The transmission curves for the optical filters used on the CCD MOSAIC Imager with the 4-meter telescope at Kitt Peak National Observatory by George Jacoby.

of 180 seconds. For NGC 6946 the final H $\alpha$  image has a total exposure time of 1800 seconds and the final  $R$  band image has a total exposure time of 225 seconds.

Data for NGC 2403 in the H $\alpha$  regime were taken by George Jacoby in January 1999 on the 0.9-meter using the CCD MOSAIC imager. These data were taken using an H $\alpha$  filter with a central wavelength of 6567 Å and a FWHM of 29 Å. The transmission curve for this filter is plotted in Figure 2.5. The same  $R$  band filter used above was used for this data set. The final H $\alpha$  image has a total exposure time of 4800 seconds and the final  $R$  image has a total exposure time of 600 seconds.

For NGC 3359, the H $\alpha$  and offband data were taken at the Observatorio del Roque de los Muchachos at the Isaac Newton Telescope by Beckman et al. in February 1996, using the prime focus CCD TEK-7. These data were taken with an H $\alpha$  filter with central wavelength of 6594 Å and FWHM of 44 Å. The offband filter has a central wavelength of 6686 Å and FWHM of 44 Å. The transmission curves of these filters are shown in Figure 2.6. The exposure time in both H $\alpha$  and the offband was 1800 seconds.

For NGC 300 and NGC 628, the H $\alpha$  and  $R$  data were taken at CTIO in December 1998 by Lauren Jones on 1.5-meter telescope using the Cassegrain Focus CCD imager. These data were taken with an H $\alpha$  filter with central wavelength of 6559 Å and FWHM of 64 Å and an  $R$  filter with central wavelength of 6425 Å and FWHM of 1500 Å. The transmission curves for these filters are shown in Figure 2.7. For both NGC 300 and NGC 628, the final H $\alpha$  and  $R$  images have total exposure times of 1200 seconds.

For NGC 4535 and NGC 4725, the H $\alpha$  and  $R$  data were taken at KPNO in February 2000 by George Jacoby on the 4-meter telescope using the CCD MOSAIC Imager. These data were taken with an H $\alpha$  filter with central wavelength of 6559 Å and FWHM of 80 Å and an  $R$  filter with central wavelength of 6440 Å and FWHM of 1510 Å. The transmission curves for these filters are shown in Figure 2.8. For

### KPNO [SII] and [SII]off Filter Transmission Curves

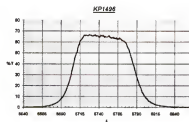


Figure 2.9: The transmission curve for the [SII] filter used on the CCD MOSAIC imager with the 0.9-meter telescope at Kitt Peak National Observatory for the data taken by George Jacoby.

NGC 4535 the final  $H\alpha$  and  $R$  images have total exposure times of 600 and 360 seconds, respectively. For NGC 4725, the final  $H\alpha$  and  $R$  images have total exposure times of 600 and 180 seconds, respectively.

#### 2.2.2 The [SII] Data

Data for NGC 2403 were taken in the [SII] ( $\lambda=6726 \text{ \AA}$ ) line by George Jacoby in January 1999 on the 0.9-meter using the CCD MOSAIC imager. These data were taken using a filter with a central wavelength of  $6746 \text{ \AA}$  and FWHM of  $83 \text{ \AA}$ ; the transmission curve is shown in Figure 2.9. The final [SII] image has a total exposure time of 3600 seconds. The  $R$  band image described in the previous section for this galaxy was used for continuum subtraction.

For NGC 300 and NGC 628, the [SII] and offband data were taken at CTIO in December 1998 by Lauren Jones on the 1.5-meter telescope using the Cassegrain Focus CCD imager. These data were taken with an [SII] filter with a central wavelength of  $6746 \text{ \AA}$  and FWHM of  $91 \text{ \AA}$  and an offband filter with a central wavelength of  $6425 \text{ \AA}$  and FWHM of  $1500 \text{ \AA}$ . The transmission curves for these filters are shown in Figure 2.10. For both NGC 300 and NGC 628, the final [SII] and offband images have total exposure times of 1200 seconds.

### CTIO [SII] and [SII] off Filter Transmission Curves

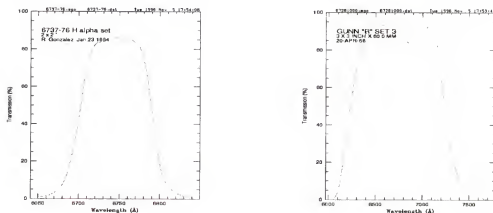


Figure 2.10: The transmission curves for the [SII] and offband filters used on the Cassegrain Focus CCD imager with the 1.5-meter telescope at Cerro Tololo InterAmerican Observatory.

### KPNO [OIII] and [OIII] off Filter Transmission Curves used by Sharp

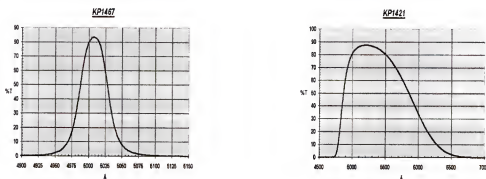


Figure 2.11: The transmission curves for the [OIII] and offband filters used on the CCD MOSAIC imager with the 0.9-meter telescope at Kitt Peak National Observatory for the data taken by Nigel Sharp.

KPNO [OIII] and [OIII] off Filter Transmission Curves used by Ciardullo, et al.

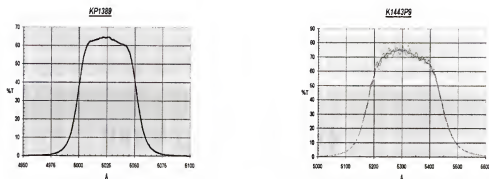


Figure 2.12: The transmission curves for the [OIII] and offband filters used on the CCD MOSAIC imager with the 4-meter telescope at Kitt Peak National Observatory for the data taken by Ciardullo, Jacoby and Feldmeier.

CTIO [OIII] and [OIII] off Filter Transmission Curves

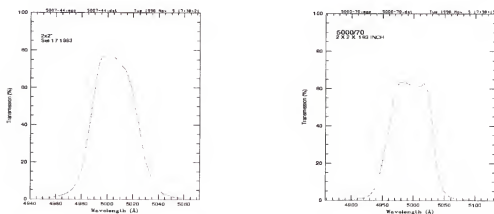


Figure 2.13: The transmission curves for the [OIII] and offband filters used on the Cassegrain Focus CCD imager with the 1.5-meter telescope at Cerro Tololo InterAmerican Observatory.



### 2.2.3 The [OIII] Data

Data for NGC 1068 and NGC 6946 in the [OIII] ( $\lambda=5007$  Å) line were taken at KPNO in November 1998 by Nigel Sharp on the 0.9-meter using the CCD MOSAIC imager. These data were taken using a filter with a central wavelength of 5008 Å and a FWHM of 45 Å. The transmission curve for this filter is shown in Figure 2.11. For continuum subtraction, a filter with central wavelength 5397 Å and FWHM 1059 Å, the *V* band, was used. The transmission curve for this filter is also shown in Figure 2.11. For NGC 1068, the final [OIII] image has a total exposure time of 2400 seconds; the final *V* image has a total exposure time of 320 seconds. For NGC 6946, the final [OIII] image has a total exposure time of 1200 seconds and the final *V* image has a total exposure time of 300 seconds.

For NGC 2403, data were taken in the [OIII] line at KPNO in December 1996 by Ciardullo, Jacoby & Feldmeier on the 4-meter using the CCD MOSAIC Imager. These data were taken using a filter with a central wavelength of 5026 Å and a FWHM of 53 Å. The continuum data for this object were taken with the filter with a central wavelength of 5311 Å and a FWHM of 265 Å. The transmission curves of both filters are shown in Figure 2.12. The final image has a total exposure time of 2700 seconds in [OIII] and 450 seconds in the offband.

For NGC 300 and NGC 628, the [OIII] and offband data were taken at CTIO in December, 1998 by Lauren Jones using the 1.5-meter telescope using the Cassegrain Focus CCD imager. These data were taken with an [OIII] filter with a central wavelength of 5005 Å and a FWHM of 39 Å and an offband filter with a central wavelength of 4994 Å and a FWHM of 77 Å. The transmission curves for these filters are shown in Figure 2.13. For both NGC 300 and NGC 628, the final [OIII] and offband images have total exposure times of 1200 seconds.

### KPNO $H\beta$ and $B$ Filter Transmission Curves used by Sharp

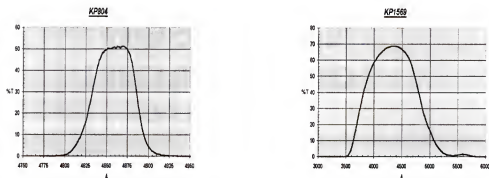


Figure 2.14: The transmission curves for the  $H\beta$  and  $B$  band filters used on the CCD MOSAIC Imager with the 0.9-meter telescope at Kitt Peak National Observatory for the data taken by Nigel Sharp.

### KPNO $H\beta$ Filter Transmission Curve used by Jacoby

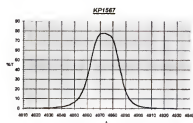


Figure 2.15: The transmission curve for the  $H\beta$  filter used on the CCD MOSAIC Imager with the 0.9-meter telescope at Kitt Peak National Observatory for the data taken by George Jacoby.

### 2.2.4 The H $\beta$ data

Data for NGC 1068 and NGC 6946 in the H $\beta$  ( $\lambda=4860$  Å) regime were taken at KPNO in November 1998 by Nigel Sharp on the 0.9-meter using the CCD MOSAIC Imager. These data were taken using a filter with a central wavelength of 4859 Å and a FWHM of 57 Å (for transmission curve, see Figure 2.14). For continuum subtraction the *B* band, a filter with a central wavelength of 4994 Å and a FWHM of 1061 Å, was used. The transmission curve for this filter is shown in Figure 2.14. For both NGC 1068 and NGC 6946, the final H $\beta$  images have a total exposure time of 1200 seconds and the final *B* images have a total exposure time of 600 seconds.

The H $\beta$  data for NGC 2403 were taken at KPNO in January 1999 by George Jacoby on the 0.9-meter using the CCD MOSAIC Imager. The transmission curve of the H $\beta$  filter used is shown in Figure 2.15. This filter has a central wavelength of 4876 Å and a FWHM of 25 Å. For continuum subtraction, the same *B* filter as Sharp was used. The final H $\beta$  image has a total exposure time of 2400 seconds; the final *B* image has a total exposure time of 600 seconds.

### 2.3 Far Infrared Data

The Far Infrared data were obtained by the Infrared Astronomical Satellite (IRAS) which was launched in January 1983 and stayed in orbit for eleven months. During this time, IRAS detected over 350,000 sources, 6 new comets and 75,000 starburst galaxies.

The data used in this study were taken with the survey array which had detectors sensitive in four bands. These were the 12  $\mu\text{m}$ , 25  $\mu\text{m}$ , 60  $\mu\text{m}$  and 100  $\mu\text{m}$  bands. We use only the 60 and 100  $\mu\text{m}$  data for our analysis. The 60  $\mu\text{m}$  data were taken by 15 detectors with a field of view of  $1.5 \times 4.7$  arcminutes. The effective bandpass of these detectors is 40 $\mu\text{m}$ -80 $\mu\text{m}$  with an average 10- $\sigma$  sensitivity of 0.85 Jy

Table 2.3: Standard Stars and Exposure Times for Optical Data

Object Name	Filter	Observatory	Date	Exp Time	Standard Star
NGC 300	R	CTIO	12/98	1200 sec	LTT 745
	H $\alpha$	CTIO	12/98	1200 sec	LTT 745
	[SII]	CTIO	12/98	1200 sec	LTT 745
	[SII]off	CTIO	12/98	1200 sec	LTT 745
	[OIII]	CTIO	12/98	1200 sec	LTT 745
	[OIII]off	CTIO	12/98	1200 sec	LTT 745
NGC 628	R	CTIO	12/98	1800 sec	F 11
	H $\alpha$	CTIO	12/98	1800 sec	F 11
	[SII]	CTIO	12/98	1200 sec	F 11
	[SII]off	CTIO	12/98	1200 sec	F 11
	[OIII]	CTIO	12/98	1200 sec	F 11
	[OIII]off	CTIO	12/98	1200 sec	F 11
NGC 1068	R	KPNO	11/98	180 sec	Landolt SA 94
	H $\alpha$	KPNO	11/98	5400 sec	Landolt SA 94
	[OIII]	KPNO	11/98	2400 sec	Landolt SA 94
	V	KPNO	11/98	320 sec	Landolt SA 94
	B	KPNO	11/98	600 sec	Landolt SA 94
	H $\beta$	KPNO	11/98	1200 sec	Landolt SA 94
NGC 2403	R	KPNO	01/99	600 sec	L 104-456
	H $\alpha$	KPNO	01/99	4200 sec	HZ 44 & F 34
	[SII]	KPNO	01/99	3600 sec	HZ 44 & F 34
	B	KPNO	01/99	600 sec	L 104-456
	H $\beta$	KPNO	01/99	2400 sec	HZ 44 & F 34
	[OIII]	KPNO	12/96	2700 sec	HZ 44 & F 34
NGC 3359	[OIII]off	KPNO	12/96	450 sec	HZ 44 & F 34
	R	OdRdlM	02/96	600 sec	unknown
NGC 4535	H $\alpha$	OdRdlM	02/96	1800 sec	unknown
	R	KPNO	02/00	360 sec	unknown
NGC 4725	H $\alpha$	KPNO	02/00	600 sec	unknown
	R	KPNO	02/00	180 sec	unknown
NGC 6946	H $\alpha$	KPNO	02/00	600 sec	unknown
	R	KPNO	11/98	225 sec	Landolt SA 112
	H $\alpha$	KPNO	11/98	2400 sec	Landolt SA 112
	V	KPNO	11/98	300 sec	Landolt SA 112
	[OIII]	KPNO	11/98	1200 sec	Landolt SA 112
	B	KPNO	11/98	600 sec	Landolt SA 112
	H $\beta$	KPNO	11/98	1200 sec	Landolt SA 112

The columns are as follows: (1) the object name, (2) the filter used, (3), the observatory at which the data were taken, (4) the date (month and year) of the observation, (5) the total on source exposure time, and (6) the standard star used for calibration. OdRdlM stands for Observatorio del Roque de los Muchachos. The observations for which the standard star is unknown were calibrated when we got them or were calibrated using published H $\alpha$  aperture photometry. A discussion of calibration procedures can be found in Chapter 3.

Table 2.4: Signal-to-Noise Estimates

Object Name	Filter	Total Exposure Time	S/N
NGC 300	R	1200 sec	49.3
	H $\alpha$	1200 sec	67.9
	[SII]	1200 sec	65.7
	[SII]off	1200 sec	50.1
	[OIII]	1200 sec	54.0
	[OIII]off	1200 sec	51.7
NGC 628	R	1800 sec	1307.7
	H $\alpha$	1800 sec	1252.3
	[SII]	1200 sec	789.1
	[SII]off	1200 sec	987.9
	[OIII]	1200 sec	2583.1
	[OIII]off	1200 sec	2535.2
NGC 1068	R	180 sec	50.0
	H $\alpha$	5400 sec	30.8
	[OIII]	2400 sec	47.3
	V	320 sec	67.9
	B	600 sec	108.7
	H $\beta$	1200 sec	93.0
NGC 2403	R	600 sec	773.7
	H $\alpha$	4200 sec	814.5
	[SII]	3600 sec	726.3
	B	600 sec	17.2
	H $\beta$	2400 sec	1293.7
	[OIII]	2700 sec	88.7
NGC 3359	[OIII]off	450 sec	84.9
	R	600 sec	65.9
	H $\alpha$	1800 sec	270.0
NGC 4535	R	360 sec	45.7
	H $\alpha$	600 sec	59.4
NGC 4725	R	180 sec	520.9
	H $\alpha$	600 sec	830.2
NGC 6946	R	225 sec	300.0
	H $\alpha$	2400 sec	290.1
	V	300 sec	477.8
	[OIII]	1200 sec	625.1
	B	600 sec	893.0
	H $\beta$	1200 sec	840.0

The columns are as follows: (1) the object name, (2) the filter used, (3), the total exposure time of the final image, (4) the average signal-to-noise achieved in the smallest aperture evaluated; this was calculated by taking the average signal from all positions evaluated in the unblurred images at the smallest aperture size and dividing that by the root mean square noise in the smallest aperture from a list of a large number of apertures selected to represent the background noise of the image.

### UIT Near Ultraviolet Filter Transmission Curves

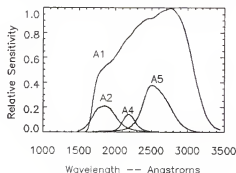


Figure 2.16: The transmission curves for the Near Ultraviolet filters used on the UIT.

for a point source. The  $100\text{ }\mu\text{m}$  data were taken by 13 detectors with a field of view of  $3.0 \times 5.0$  arcminutes. The effective bandpass of these detectors is  $83\text{ }\mu\text{m}$ - $120\text{ }\mu\text{m}$  with an average  $10\text{-}\sigma$  sensitivity of  $3.0\text{ Jy}$  for a point source.

Each of the galaxies in our sample were mapped by this survey array. Different galaxies have different amounts of actual coverage. Initial processing of all IRAS data was done by the Infrared Processing and Analysis Center (IPAC).

### 2.4 Ultraviolet Data

The ultraviolet data were obtained by the Ultraviolet Imaging Telescope (UIT). UIT is a 38-cm aperture,  $f/9$  Ritchey-Chretien telescope with an angular resolution of 2-4 arcseconds over a 40 arcminute diameter field of view. UIT has two selectable cameras, consisting of magnetically-focused, two-stage image intensifiers coupled by optical fibets to 70-mm film. The cameras employ CsTe (camera A) and CsI (camera B) photocathodes, and each one has a 6-piston filter wheel. The photocathode-filter combinations yield excellent long-wave rejection. Camera A has a wavelength range of  $1150\text{-}3500\text{ }\text{\AA}$ ; and Camera B has a wavelength range of  $1150\text{-}2000\text{ }\text{\AA}$ . UIT was launched on the Space Shuttle on two missions, ASTRO-1 (2-10 December, 1990) and ASTRO-2 (3-17 March, 1995).

## UIT Far Ultraviolet Filter Transmission Curves

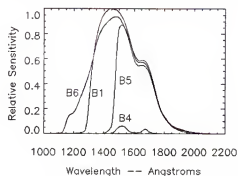


Figure 2.17: The transmission curves for the Far Ultraviolet filters used on the UIT.

Data for NGC 2403 were obtained on the ASTRO-2 mission using the B1 (far ultraviolet) filter; data for NGC 628 and NGC 1068 were obtained from the ASTRO-1 mission using the A1 (near ultraviolet) filter.

## CHAPTER 3 DATA REDUCTION

In this chapter we describe the methods of basic data reduction used for the data used in this dissertation project. The chapter is divided into sections by instrument and wavelength. A description of the data manipulation for analysis is described in the Analysis Chapter.

### 3.1 Near Infrared Data

All the near infrared data were taken in the same manner. The object was imaged along with the sky in an ABBA pattern for a total of 32 images per sequence. In some cases, only 16 images were taken due to time constraints. Below, we describe the method of reduction used for a 32-image sequence (the 16-image sequences were reduced in the same way). Samples of the reduction frames (i.e., dark, dark mask, flat, flat mask, mask, sky, raw and reduced images) are displayed in Appendix A.

#### 3.1.1 Linearization

The following information was taken from the manual for the InfraRed IMager (IRIM) and applies to the data from both IRIM and CIRIM.

Near infrared detectors utilize hybrid architecture in which each pixel has an associated unit cell which controls the biasing and readout of that pixel; each pixel is essentially independent of the others. For this reason, effects seen in CCDs, such as charge bleeding or trailing from saturated pixels are not present. However, this independence also means that properties such as linearity and dark current can vary from pixel to pixel. It is necessary to calibrate these effects for optimum scientific performance.



Linearity Sequence Plot

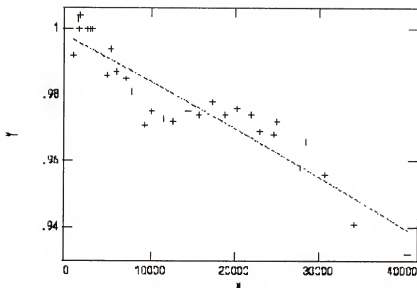


Figure 3.1: The linearity sequence for the InfraRed IMager (IRIM) at Kitt Peak National Observatory. The x-axis is the actual measured number of counts and the y-axis is the actual number of counts divided by the expected number of counts. In this image, one can see that, while the points do not appear very well fit by a line, the deviation from a good linear fit is very small.

The linearity of a pixel changes because when a pixel is reset, the voltage difference between the pixel and detector substrate creates a depletion region which acts as a potential well for the collection of photogenerated carriers. As charge accumulates in the pixel, the depletion region fills in, increasing its capacitance and that of the entire pixel node. Coupled with the steadily decreasing bias on the pixel, this yields a sublinear voltage-charge relationship, which quickly saturates when the pixel voltage reaches that of the zero bias. Technically, a pixel will continue to accumulate charge even into forward bias, but its response by that time will be significantly nonlinear.

The linearity correction is particularly important for observations through broad band filters where the integration time on most objects is limited by the sky background, and one is operating at a significant fraction of the full well capacity. A linearity sequence is taken to determine the linearity properties for a given chip.

The NICMOS detector, used in both the IRIM and CIRIM instruments, shows a significant temperature dependence of quantum efficiency and, presumably, related properties, such as linearity and dark current. A linearity relation is determined by a series of images taken at increasing exposure times. The actual/expected counts are then plotted versus the actual counts and a line is fit to the data (see Figure 3.1).

The first step in the data reduction process is to linearize the data. We do this using the parameters given in the manual. The linearization of all images is done using the IRAF task `irlincor`, built specifically for this procedure.

### 3.1.2 Darks

In the absence of exposure to photons, an accumulation of charge still occurs in each pixel. There are four sources for this dark current:

- diffusion of charge
- thermal generation-recombination of charges in the semiconductor
- leakage currents
- photons emitted by the array readout

Both diffusion and thermal generation-recombination of charges are exponential functions of temperature and can be reduced by maintaining the detector at a low temperature through a dewar. Leakage currents are determined by the manufacturing process and the applied (bias) voltage. This is what is observed in a dark current frame.

The dark current (of IRIM and CIRIM) has a complex character which cannot be simply scaled with exposure time. Therefore, it is necessary to take dark frames for each exposure length at which a science object was observed. We took 5 to 10 dark frames per exposure time twice each night; once at sunset and once at sunrise. To construct an average dark, we used all darks taken on a given night (both sunset

and sunrise). Generally, there was no difference between these two sets unless there was a problem with the coolant in the detector. Neither darks, nor any science frames should be taken just before or just after coolant is added to the detector since the detector is usually very hot at those times.

### 3.1.3 Flats

To take into account the chip's spatially varying response to light, flat fields are needed. The simplest and most efficient way to account for a sensitivity gradient across the chip of a near infrared detector is to use sky flats. We took dome flats for comparison, but in all data reductions chose to use the sky flats since they were sufficient to reduce the data. The advantages of sky flats over dome flats are (1) the sky images are taken in the same sequence as the object data so that if there is any temperature change (which can effect linearity and dark current) it will be inherent in the data, and (2) it is an effective use of the data frames since every frame is used to its fullest capacity. As long as the sky flat produced has the same features as the dome flat, it is most advantageous to utilize it, rather than a dome flat for the reasons described above.

We made flats from the sky frames by combining the set of 16 dark- subtracted sky frames (per 32-frame sequence; 8 sky frames are produced in the 16-image sequences) using `imcombine` with a median filter, allowing for pixel clipping (at the 3-sigma level) and median scaling so that all sky features (i.e., stars and brightness gradients not inherent to the chip) disappear and we are left with features unique to the imaging array. We then normalize the flats so that the intensity range is from 0 to 1 and average them together.

### 3.1.4 Sky Subtraction

At the short wavelength end of the near infrared regime ( $\lambda \leq 2.3\mu\text{m}$ ), sky subtraction is a tricky business. This is mainly due to emission lines from OH in the upper atmosphere (airglow). These lines can vary over the course of a night and

upper level winds can create inhomogeneity and motion of the airglow so that the sky brightness can vary in time on the order of the length of our exposures. Therefore, it is important to sky subtract carefully.

For each 32-frame sequence, we make 13 sky frames, each of which is a combination of the closest (in time to the object frame being analyzed) four sky frames. The sky frames are combined using a median filter. This eliminates features like stars and bad pixels without eliminating other sky features, like brightness variations and gradients not inherent to the chip.

#### 3.1.5 Masks

Near infrared arrays are notorious for their numerous bad pixels, in addition to the above-mentioned problems with linearity. To offset these effects we strategically dithered around the position of the object being observed to avoid always landing the same feature on a bad pixel or low-sensitivity region of the chip. In order to fully account for the bad pixels, which cannot be taken out of dithered data in the usual way, however, it is necessary to use masks.

We create two masks, one from the dark frame and one from the flat for each sequence analyzed. In the dark frame, we identify hot pixels which will make features appear brighter than they really are. In the flat frame, we identify dead pixels which are not registering flux. In both cases, we set the bad pixels to zero and the good pixels to one using the IRAF task, `imreplace`. A mask for each object image is created by multiplying the two masks together so that all bad pixels (hot or dead) have a value of zero and all good pixels have a value of one. These masks are then included in the final combination of the reduced data to mark any bad pixels that are not wiped out by the median filter.

#### 3.1.6 Object Frames

Each raw object frame in a 32-image sequence is sky-subtracted using the sky frame created from the four sky frames closest in time to the object frame. This

operation removes sky features and dark current, since the sky frames have not been dark-subtracted. After this, the object frame is flat-fielded by dividing the object frame by the normalized average sky flat for the sequence. Lastly, the flat-fielded, sky-subtracted object frames are stacked together to make one image with signal-to-noise equivalent to a 1600 second exposure.

### 3.1.7 Standard Stars and Calibration

To calibrate the frames, we use standard stars taken in a 9-grid pattern (no independent sky measurements). The reduction of these images is similar to that described above except that flats and sky frames are created by combining all nine images using a median filter to eliminate stars and bad pixels.

Since very few stars are calibrated spectrophotometrically in the near infrared regime, our reduced standard star frames (in both continuum and line bands) were calibrated primarily using models from the Kurucz Stellar Atmospheres Atlas (1996). To do this, we took a model of a star of the same spectral type and luminosity class as our standard star. We calculated the flux at  $2.2\mu\text{m}$  from the  $K$  magnitude of the standard star from Elias et al. (1982) then, using the model, we calculated the flux at the central wavelengths of our two narrowband filters. In this way, our images were calibrated in both the line and continuum bands. As a check, we calibrated the standard stars using the  $K$  band magnitude from Elias et al. (1982), and calculated the  $J$  band magnitude from the model. The model always gave a flux within 0.01% of that derived from the Elias et al. (1982)  $J$  band magnitude.

Generally, we observed the standard stars and objects in an SOOS pattern as well. Thus, two standard star nine-grid observations bracket two object 32-image sequences. When calibrating data for a night, we may have several ( $n$ ) 32-image sequences for a given object in a given band. We calibrate each 32-image sequence with the two nearest standard star observations and then combine all reduced images to form a final image which will have a signal-to-noise equivalent to a  $n \times 1600$  second

exposure with some edges of lower signal-to-noise. Of course, the final image looks much smoother and highlights the features of the galaxy more clearly.

## 3.2 Optical Data

Samples of the reduction frames (i.e., bias, flat, raw and reduced) are displayed in Appendix B.

### 3.2.1 Kitt Peak MOSAIC Imager

Several optical images used in this analysis were taken at the Kitt Peak National Observatory using the MOSAIC Imager at both the 4-m telescope (Feldmeier, Jacoby and Ciardullo, personal communication) and at the 0.9-m telescope (Sharp 1998, personal communication; Jacoby 1999, personal communication). Most of these data were reduced afterwards, but some of these data (from Feldmeier et al. and Sharp) were received in reduced, but not calibrated, form.

We used the IRAF task `ccdproc` to process these data. This task bias-subtracts, dark-subtracts and flat-fields the raw images; the task also trims the image and removes the overscan regions. The data were then calibrated using standard stars taken in the same bands at the same airmasses.

### 3.2.2 Cerro Tololo TEK 2K CCD

Some optical images used in this analysis were taken at the Cerro Tololo InterAmerican Observatory using the TEK 2K CCD. This was done as a result of the failure of the InfraRed Imager (CIRIM) in the middle of the last observing run dedicated to this dissertation research.

We used the IRAF task `quadproc` to process the data. The only difference between `quadproc` and `ccdproc` is that `quadproc` is designed specifically to deal with the four amplifier readout method used by the TEK 2K CCD. `Quadproc` bias-subtracts, dark-subtracts and flat-fields the raw images; the task also trims the image and removes the overscan regions.

### 3.2.3 Calibration and Standard Stars

We used spectrophotometrically calibrated standard stars, when available, to calibrate the optical data. When such standard stars were not available, we were forced to resort to the method used above, for the near infrared standard stars. In those cases, we used models from the Kurucz Stellar Atmospheres Atlas (1996). As before, we used broad band magnitudes to calibrate the models and then calculated the flux in the narrow bands needed.

### 3.3 Far Infrared Data

The far infrared data were obtained from the Infrared Processing and Analysis Center (IPAC)<sup>1</sup>. For each galaxy, we requested the High Resolution (HIRES) processed IRAS images for the 60 and 100  $\mu\text{m}$  bands. IRAS HIRES processed images have already undergone an image deconvolution process called the Maximum Correlation Method (Aumann, Fowler & Melnyk 1990). This is a linear image deconvolution method which uses no input low resolution image, but rather, reconstructs the image recursively, so that in each image, pixels separated by more than the mean correlation length become increasingly decorrelated until the maximum correlation consistent with the measurements and the measurement uncertainties is achieved. We have taken the image from the 20th such iteration.

At the 20th iteration in the HIRES processing, the finest resolution at 100  $\mu\text{m}$  is  $1'$ . In order to compare to our near infrared and optical data, it was in our best interest to try to obtain reliable data with resolution better than  $1'$ . We chose to use Pixon-based image reconstruction to improve the resolution of the IRAS HIRES images.

---

<sup>1</sup>IPAC serves to carry out data-intensive processing tasks of vital importance to NASA's infrared astronomy program, maintain data archives and access tools, offer scientific expertise on various projects to scientific investigators, and to conduct education and outreach efforts aimed at the general public.

Instead of working in pixels, or mean correlation lengths, the Pixon method works in the fundamental information elements of a data set. These elements, pixons, are derived from information theory and Bayesian probability theory. As such, they are elements in a minimal coordinate system and describe an image in terms of its “algorithmic information content” – they have no fixed size, but instead their size depends on the information they represent. Previous techniques, such as the Maximum Likelihood and Maximum Entropy methods, are less versatile subsets of the Pixon approach. Additionally, the Pixon method conserves flux; whereas, some deconvolution methods (notably the Richardson-Lucy Method used for HST pre-repair data) do not.

### 3.3.1 The Pixon Method

Pixon image reconstruction is a process used to increase resolution in an image in the same way a deconvolution would. In a deconvolution, the data  $D(\mathbf{x})$ , is defined as

$$D(\mathbf{x}) = (HI)(\mathbf{x}) + N(\mathbf{x}) \quad (3.1)$$

where  $H(\mathbf{x})$  is the point spread function,  $I(\mathbf{x})$  is the true image,  $N(\mathbf{x})$  is the noise, and  $\mathbf{x}$  is an  $n$ -dimensional vector. The solution to the problem of deconvolution is the inverse of the above equation. In Pixon image reconstruction, Bayesian Estimation is used and the above equation is expressed in terms of probability.

$$p(D, I, M) \quad (3.2)$$

where the above statement reads: “the probability that the data, true image and model are related”. So,  $D$  represents the data,  $I$  is the true image and  $M$  is the model, which is given as  $H(\mathbf{x})$ , the point spread function, above. Of course, in the Pixon method, the noise,  $N(\mathbf{x})$  is folded in to the model,  $M$ .

One can write the above statement in many ways:



$$p(D, I, M) = p(D|I, M)p(I, M) \quad (3.3)$$

$$= p(D|I, M)p(I|M)p(M) \quad (3.4)$$

$$= p(I|D, M)p(D, M) \quad (3.5)$$

$$= p(I|D, M)p(D|M)p(M) \quad (3.6)$$

equating several of these restatements of the problem, one can derive two different approaches to solving the problem.

$$p(I|D, M) = \frac{p(D|I, M)p(I|M)}{p(D|M)} \quad (3.7)$$

and

$$p(I, M|D) = \frac{p(D|I, M)p(I|M)p(M)}{p(D)} \quad (3.8)$$

Equation 3.7 describes the method used in Maximum Likelihood and Maximum Entropy deconvolution methods. In those methods, one maximizes the probability that the true image is related to the data and the model. Since the model is the point spread function with the noise folded in, we have no prior knowledge of the model.

If, however, we use equation 3.8, we will maximize the probability that the image and model are related to the data. Now, both unknowns are on the same side of the probability assessment and we are calculating the *a posteriori*. Equation 3.8 describes the Pixion method. Thus, the first obvious difference between the two methods (i.e., Equations 3.7 and 3.8) is the quantity which is maximized.

Looking at the right hand sides of Equations 3.7 and 3.8, we notice that both numerators contain the quantity  $p(D|I, M)$ . This is known as the "Goodness of Fit". A typical expression of this term is

$$p(D|I, M) = e^{-\chi^2/2} \quad (3.9)$$

This is the standard chi-square distribution. While this assumption assures a faithful rendition of the data, it typically produces images with spurious low signal-to-noise features.

Another quantity common to both Equations 3.7 and 3.8 is  $p(I|M)$ . This is known as the “prior”. In Maximum Entropy deconvolution methods, the prior is expressed as

$$p(I|M) = e^{\alpha S} \quad (3.10)$$

where  $\alpha$  is an adjustable constant used to weight the relative significance of “Goodness of Fit” and the image “prior” and  $S$  is the entropy of the image. The Maximum Entropy method, however, is fundamentally flawed in that it presumes that entropy is maximized in the true image. If that were so, one would derive a featureless true image. Further, in the Maximum Entropy and Maximum Likelihood methods, the number of degrees of freedom is equal to the number of pixels in the image.

The Pixon method, therefore, defines the “prior” in a completely different way; one which is inversely proportional to the number of pixels in the image. This way, *maximizing* the “prior” is the same as *minimizing* the number of degrees of freedom in the problem.

$$p(I|M) = p(\{N_i\}, n, N) = \frac{N!}{n^N \prod N_i!} \quad (3.11)$$

where  $\{N_i\}$  is the set of the counts in all pixels,  $i$ , and  $N$  is the total counts in the image (i.e.,  $N = \sum N_i$ ).

Defining the “prior” as in Equation 3.11, one can easily see that the solution to Equation 3.8 is now found by decreasing the total number of pixels,  $n$ , and by

making the  $\{N_i\}$  as large as possible. That is, we use the fewest number of cells and fill each one with the maximum number of counts. These new elements are called pixons.

One final difference between Equations 3.7 and 3.8 is that in the latter equation, one must evaluate  $p(M)$ . This quantity is crucial to the relative balance between the “Goodness of Fit” and the “prior”.

In summary, the Pixon method assumes no model, but rather tests the probability that the model and true image result in the data that you see. Also, the Pixon method defines the “prior” such that the solution to the problem results in a minimization of the number of elements considered; hence, the pixons. Finally, an evaluation of the quantity  $p(M)$ , the probability that the model is correct, is performed to balance the “Goodness of Fit” and the “prior”. These aspects of the Pixon method reduce the production of spurious low signal-to-noise features in the true image.

### Procedure

After acquiring the pixon program from the public website, we ran the programs needed to determine the number of pixon elements deemed necessary for image reconstruction. We used 20 pixon elements for our reconstruction runs. The four input parameters are

- the data image
- the point spread function
- the pixon map (a minimum resolution map)
- sigma (a measure of the noise level)

The data image was the HIRES processed IRAS image. We trimmed the image so that it was 100 pixels on a side (to reduce the number of pixels in the final

image). We then magnified the image by a factor of three to decrease the pixel size to 5" per pixel.

For the point spread function, we used the "flat reduced" beam image which is produced as a part of the HIRES processing of IRAS data. The beam image is essentially a point spread function for a simulated point source with the flux of the galaxy, knowing the limitations of IRAS. HIRES processing produces a beam image with 25 beams of strength equal to that of the peak flux of the galaxy at different locations in the image. This beam image was trimmed to include only one beam; often after trimming we used the `fixpix` function in IRAF which replaces the selected pixels with an average value of the surrounding pixels to eliminate all traces of the adjacent beams. The beam images were also magnified by a factor of three so that they have the same pixel size as the data images.

For the pixon map or minimum resolution map, we created a signal-to-noise image and inverted it. To do this, we measured the average noise in the image by summing all lines and picking an area in the image where there were no known sources and the image looked flat. We then multiplied the inverted image by the average noise level. In doing this, we allow the minimum resolution to be achieved where the signal-to-noise is highest. For sigma, the level of the noise, we used the average noise measurement described above.

## Results

Our IRAS HIRES images start with 1' resolution and 15" pixels. In Table 3.1, we show the number of iterations for which each image was run along with the final percent convergence achieved. Usually, the program stopped itself at some convergence. Sometimes, however, the program ran for a long time (several hundred iterations) while the convergence bounced around some low number. In these cases, we stopped the program manually.

Table 3.1: Resolution of FIR Bands

Object Name	60 $\mu\text{m}$ ( $''$ )	Iter.	Conv.	100 $\mu\text{m}$ ( $''$ )	Iter.	Conv.
NGC 300	13.1	427	0.012	8.4	22	0.000
NGC 628	25.46	126	0.056	53.51	120	0.122
NGC 1068	4.75	155	0.122	11.22	83	3.223
NGC 2403	17.15	164	0.236	27.56	121	0.008
NGC 3359	12.0	482	0.005	11.5	213	0.037
NGC 4535	5.1	118	0.010	20.9	131	0.050
NGC 4725	5.95	70	0.008	4.95	131	0.009
NGC 6946	16.94	351	0.008	27.75	164	0.000

The columns are as follows: (1) the object name, (2) resolution achieved in 60  $\mu\text{m}$  image in arcseconds, (3) number of iterations of Pixon processing of 60  $\mu\text{m}$  image, (4) final percent convergence measure for 60  $\mu\text{m}$  image, (5) resolution achieved in 100  $\mu\text{m}$  image in arcseconds, (6) number of iterations of Pixon processing of 100  $\mu\text{m}$  image, and (7) final percent convergence measure for 100  $\mu\text{m}$  image.

After processing the images using the Pixon method described above, we also processed the beam images, used as point spread functions. This resulted in a beam image reconstructed in the same way as the galaxy image. We measure this reconstructed beam image to determine the resolution in the reconstructed galaxy image. The measurement of the beam was done using the `imfit` task in AIPS. It was difficult for the tasks available in IRAF to perform this task consistently and effectively; the IRAF task `fitpsf` usually gave a singularity error. Since most reconstructed beam images were ellipsoidal and rotated, as in radio images, we turned to the tasks in AIPS for this special assessment. The final resolutions of our images are given in Table 3.1. Recalling that these images began with resolutions of 60'', it is easy to see that the improvement is significant, in most cases.

### 3.4 Uniformity of Data from Different Wavelength Regimes

Finally, to compare all the data from the various wavelength regimes, it is necessary to convolve them to the same resolution and trim them to the same coverage

range. The point spread functions of the images in all bands were measured (non-IRAS data using the `fitpsf` task in IRAF, and IRAS data using the `imfit` task in AIPS as described above). Each image was blurred using the `gauss` task in IRAF. This task requires the following inputs:

- the sigma of the gaussian
- the ratio of sigma in y to x
- the position angle of the ellipse

The sigma of the gaussian was calculated as follows:

$$\sigma = \frac{\sqrt{\sigma_{100}^2(\prime\prime) - \sigma_{\lambda}^2(\prime\prime)}}{(\prime\prime/\text{pixel})_{\lambda}} \quad (3.12)$$

where  $\sigma$  is the sigma of the gaussian in pixels,  $\sigma_{100}$  is the length of the major axis of the point spread function in the 100  $\mu\text{m}$  image in arcseconds,  $\sigma_{\lambda}$  is the radius of the point spread function in the image taken at wavelength  $\lambda$  in arcseconds, and the denominator is the scale of the image taken at wavelength  $\lambda$  in arcseconds/pixel.

The rotation angle of the ellipsoidal point spread function, theta, is the supplement of the angle, beta, measured by `imfit` in AIPS (e.g., theta = 180 - beta). The ratio of the minor to major axes is that of the point spread function for the 100  $\mu\text{m}$  image.

Images were trimmed to the same coverage area using the tasks `geomap` and `geotran` in IRAF which rotate and geometrically transform one image to resemble another in coverage area and orientation. Since identification of stars is impossible due to the poor resolution of the IRAS images, direct orientation of the non-IRAS images to the IRAS images was not possible. We know, however, that the Digital Sky Survey images are produced with a standard orientation, as are the IRAS HIRES images. We chose, therefore, to geometrically transform all non-IRAS images to

Table 3.2: Resolution of Optical Bands

Object Name	H $\beta$	$B$	H $\alpha$	$R$
NGC 300	...	...	1.248	1.248
NGC 628	...	...	$0.384 \pm 0.002$	$2.328 \pm 0.038$
NGC 1068	1.250	1.250	1.250	1.250
NGC 2403	$1.253 \pm 0.034$	$1.660 \pm 0.001$	$1.556 \pm 0.001$	$3.033 \pm 0.001$
NGC 3359	...	...	$0.595 \pm 0.001$	$0.680 \pm 0.033$
NGC 4535	...	...	$0.903 \pm 0.001$	$0.951 \pm 0.001$
NGC 4725	...	...	$0.932 \pm 0.003$	$1.031 \pm 0.002$
NGC 6946	$1.111 \pm 0.002$	$1.215 \pm 0.002$	$1.091 \pm 0.001$	$1.559 \pm 0.0019$

The average FWHM in arcseconds for the images taken in the bands listed in columns 2 through 5.

Table 3.3: Resolution of Other Optical Bands

Object Name	[OIII]	$V/[\text{OIII}]_{\text{off}}$	[SII]	[SII] <sub>off</sub>
NGC 300	1.248	1.248	1.248	1.248
NGC 628	$0.524 \pm 0.008$	$0.612 \pm 0.010$	$0.881 \pm 0.007$	$0.718 \pm 0.008$
NGC 1068	1.250	1.250	...	...
NGC 2403	$1.977 \pm 0.001$	$1.253 \pm 0.034$	$1.358 \pm 0.037$	$1.140 \pm 0.001$
NGC 3359	...	...	...	...
NGC 4535	...	...	...	...
NGC 4725	...	...	...	...
NGC 6946	$1.025 \pm 0.002$	$1.318 \pm 0.001$	...	...

The average FWHM in arcseconds for the images taken in the bands listed in columns 2 through 5.

resemble a Digital Sky Survey image. From the Digital Sky Survey images which were retrieved with a global coordinate system, we were able to translate the positions of apertures chosen on the ultraviolet, optical, or near infrared image to positions on the IRAS image and vice versa.

In Tables 3.1 (FIR), 3.2 (Optical), 3.3 (Optical) and 3.4 (Near Infrared) we show the full width at half maximum (FWHM) measured for each galaxy at each wavelength. For some galaxies, the FWHM is identical across many bands; this indicates that the data were taken together, by the same observer on one night.

Table 3.4: Resolution of Near Infrared Bands

Object Name	$J$	$\text{Pa}\beta$	$2.14\mu\text{m}$	$\text{Br}\gamma$
NGC 300	. . .	. . .	1.254	1.254
NGC 628	. . .	. . .	$1.417 \pm 0.017$	$2.328 \pm 0.038$
NGC 1068	1.254	1.254	1.254	1.254
NGC 2403	$2.362 \pm 0.038$	$1.327 \pm 0.002$	$2.336 \pm 0.024$	$1.949 \pm 0.005$
NGC 3359	1.254	1.254	1.254	1.254
NGC 4535	. . .	. . .	1.254	1.254
NGC 4725	2.006	2.006	2.006	2.006
NGC 6946	. . .	. . .	$1.157 \pm 0.008$	$1.113 \pm 0.001$

The average FWHM in arcseconds for the images taken in the bands listed in columns 2 through 5.



## CHAPTER 4 ANALYSIS

In this chapter we discuss the analysis used to determine which stellar population dominates the heating of dust in spiral galaxies. To do this, we must first lay out the groundwork for the energy budget of dust heating and reradiation.

### 4.1 The Energy Budget

In order to determine which stellar population is dominating the heating process, we analyze the input and output energies of each population. The input energy is the absorbed light from a population of stars; the output energy is the far infrared light emitted by dust.

In this model, we assume that the energy absorbed by the dust is *proportional* to the energy emitted by the dust in the far infrared regime. We will also assume that the fraction of the extinguished light which is absorbed is the same for each population once we have taken into account the total (bolometric) contribution from each population. These are simplifying assumptions which we are forced to make since there are no models which take other possible scenarios into account for this type of analysis. Also, these assumptions are typical and are not contradictory to what we know about the interstellar medium in galaxies. If these assumptions are wrong, it would affect the outcome of our analysis.

#### 4.1.1 Basic Formulation

To evaluate the input energy we assess the extinction in a given region. Using the following relationship, we can determine the true emitted flux knowing the observed flux and the amount of extinction.

$$F(\lambda)_{\text{obs}} = F(\lambda)_{\text{true}} \times e^{-\tau_\lambda} \quad (4.1)$$

Here,  $F(\lambda)_{\text{obs}}$  is the observed flux at a given wavelength,  $F(\lambda)_{\text{true}}$  is the true emitted flux at that wavelength, and  $\tau_\lambda$  is the extinction at that wavelength. Again, we are using a simplifying assumption, here; namely, that the extinction that a certain wavelength light experiences can be represented by a single value for  $\tau_\lambda$ . In reality, extinction is probably not constant over the areas we are examining; however, we are limited by the resolution of our PIXON-enhanced HIRES IRAS images. Thus, while this assumption is not realistic, it probably will not affect our results since our resolution in the far infrared is so poor. Using the following simple relationship, we can find the amount of extinguished light.

$$F(\lambda)_{\text{obs}} = F(\lambda)_{\text{true}} - F(\lambda)_{\text{ext}} \quad (4.2)$$

Here,  $F(\lambda)_{\text{obs}}$  and  $F(\lambda)_{\text{true}}$  are as described above, and  $F(\lambda)_{\text{ext}}$  is the extinguished flux at a given wavelength.

#### 4.1.2 Model Populations

To learn which population of stars is responsible for heating the dust which produces far infrared light, we use STARBURST99 software (Leitherer et al. 1999) to model three populations: an “old”, “young” and “very young” population. These populations are each formed from  $106 M_\odot$  of gas. The “old” population is 12 Gyr old, formed by a single, instantaneous burst of star formation. The “young” population is 12 Gyr old, with a constant star formation rate. The “very young” population is 1 Myr old. A plot of the energy vs. wavelength for each of these populations is shown in Figure 4.1. We use the continuum ( $2.14 \mu\text{m}$ ) band to trace the “old” population which is dominated by giant stars. When available, we use the ultraviolet ( $2200 \text{ \AA}$ ) data to trace the “young” population which is dominated by stars of spectral type A and later. We use the Brackett Gamma ( $2.165 \mu\text{m}$ ) data to trace the “very young”

population which is dominated by stars of spectral types O and B. For each model population, therefore, we have a spectral energy distribution. We chose to set the stellar flux shortward of  $912 \text{ \AA}$  to zero, thus assuming that those photons are absorbed and reprocessed by the gas.

### Population Models

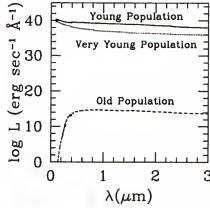


Figure 4.1: The spectral energy distributions of the three model populations. The x-axis is the wavelength in microns and the y-axis is the log of the luminosity density in  $\text{erg sec}^{-1} \text{ \AA}^{-1}$ .

#### 4.1.3 Extinction Models

In order to assess the extinction in a region of a galaxy, we must assume an extinction model. We use the model described by Cardelli et al. (1989) for the Very Young Population, where we measure reprocessed starlight through gas emission lines. We use the model described by Calzetti et al. (2000) for the Young Population and the Old Population, where we measure starlight directly. The Cardelli Model uses the galactic extinction law and assumes that the dust is concentrated in a thin layer above and below the disk of the galaxy – the foreground screen model. While this model is simplistic, it does seem to be effective for predicting extinction in regions where gas emission lines are used to measure reprocessed starlight (see Calzetti et al. 1996). The Calzetti Model is a theoretically derived model which uses the assumption that the dust is mixed with the gas and dust in the middle of the disk of the galaxy.

### Extinction Models

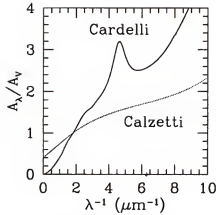


Figure 4.2: The two extinction models used in the analysis described in this section. The x-axis is the inverse wavelength in  $\mu\text{m}^{-1}$  and the y-axis is the extinction at a wavelength relative to the the extinction for the  $V$  band.

It is more effective at modelling extinction for stars. These models are plotted in Figure 4.2.

Both the Cardelli and Calzetti Models are limited in wavelength scope. The Cardelli Model extends from  $1000 \text{ \AA}$  in the UV to  $8 \mu\text{m}$  in the near infrared. The Calzetti Model extends from  $915 \text{ \AA}$  in the UV to  $2.2 \mu\text{m}$  in the near infrared. For the purposes of this study, we have extended both models to cover the range from  $915 \text{ \AA}$  to  $8 \mu\text{m}$ . To make sure this would not affect our analysis, we ran the analysis with the limited models and the results do not change.

#### 4.1.4 Extinction Correction

We will measure extinction using the narrowband images taken at the wavelengths of recombination lines of hydrogen (e.g.,  $H\alpha$ ,  $H\beta$ ,  $\text{Pa}\beta$ , and  $\text{Br}\gamma$ ). For this reason, the extinction we measure will follow the Cardelli Model. Later, we will derive a relationship between this extinction and that which will follow the Calzetti Model.

In order to assess the extinction in a region, we use case B recombination theory as laid out by Baker & Menzel (1938). In case B recombination, the  $\text{H II}$

region is optically thick to Lyman lines (except Lyman  $\alpha$  which is a special case). In other words, for all excited levels, except the second level, transitions to ground state are balanced by photoexcitation from ground to the given level. The Lyman  $\alpha$  line (level 2 to level 1 transition) is scattered and absorbed out, so that no Lyman lines escape the H II region.

Making the above assumptions along with typical assumptions of gas density ( $10^4 \text{ cm}^{-2}$ ) and temperature ( $10^4 \text{ K}$ ), we can calculate theoretical line ratios which can be used to compare to the observations. Knowing the theoretical line ratios, and assuming an extinction model (which is wavelength dependent), we can compare the observed ratios to the theoretical ratios and determine the extinction through this simple relation:

$$A_V = \frac{2.5 \times \log(\frac{R_o}{R_p})}{\frac{A_{\lambda_1}}{A_V} - \frac{A_{\lambda_2}}{A_V}} \quad (4.3)$$

For each observed line ratio,  $R_o$ , we have a predicted line ratio  $R_p$ , where each line ratio is given by  $\frac{F_{\lambda_2}}{F_{\lambda_1}}$ . The values of  $\frac{A_{\lambda_1}}{A_V}$  and  $\frac{A_{\lambda_2}}{A_V}$  are taken from the Cardelli Model.

For cases where we have more than one observed line ratio (i.e., three or more hydrogen recombination line narrow band images), we use a slightly different method to determine the extinction which uses all available data (Petersen & Gammelgaard 1996). We calculate a value  $y$  using the following relation

$$y = 2.5 \times \log(\frac{R_o}{R_p}) \quad (4.4)$$

which is just the numerator of the right hand side of Equation 4.3. The variable  $x$  is given by

$$x = \frac{A_{\lambda_2}}{A_V} \quad (4.5)$$

where  $\lambda_2$  is wavelength of the hydrogen recombination line in the ratio  $\frac{F_{\lambda_2}}{F_{\lambda_1}}$ . To determine the extinction,  $A_V$ , a linear regression is done on  $x$  and  $y$  so that the slope of the line fit is the negative of the extinction.

$$y = ax + b \quad (4.6)$$

and

$$A_V = -a \quad (4.7)$$

To calculate slope of the line fit, we used a weighted linear fit so that the errors in the line ratios are accounted for in the solution (e.g., a line ratio with large error will not influence the value of  $A_V$  as much as a line ratio with small error).

In order to correct the flux in the Br $\gamma$  band for extinction, we use the Cardelli Model and calculate the extinction at the central wavelength of the Br $\gamma$  band. To deredden the light in the Br $\gamma$  band, we solve Equation 4.1 for  $F(\lambda)_{\text{true}}$ , which gives the relation

$$F(\text{Br}\gamma)_{\text{true}} = F(\text{Br}\gamma)_{\text{obs}} \times e^{\tau_{\text{Br}\gamma}} \quad (4.8)$$

where

$$\tau_{\text{Br}\gamma} = A_{\text{Br}\gamma}/1.086 \quad (4.9)$$

and

$$A_{\text{Br}\gamma} = \frac{A_{\text{Br}\gamma}}{A_V} \times A_V \quad (4.10)$$

and  $A_V$  is derived from Equation 4.7 above. For the Cardelli Model,  $\frac{A_{\text{Br}\gamma}}{A_V}$  is known.

For the UV and 2.14 $\mu\text{m}$  bands (which represent the “young” and “old” populations, respectively), we use the empirical relation given in Calzetti et al. (2000)

between the extinction measured from reprocessed starlight,  $E_g(B-V)$ , and the extinction measured from direct starlight,  $E_s(B-V)$ ,

$$E_s(B-V) = 0.44 \times E_g(B-V) \quad (4.11)$$

where  $E_s(B-V)$  is given by

$$E(B-V) = A_B - A_V \quad (4.12)$$

and

$$A_B = \frac{A_B}{A_V} \times A_V \quad (4.13)$$

Using the Cardelli Model to represent the extinction measured using the gas lines and the Calzetti Model to represent the extinction of the stars, we can rewrite Equation 4.11 to read

$$\frac{A_{B_{Cs}}}{A_{V_{Cs}}} \times A_{V_{Cs}} - A_{V_{Cs}} = 0.44 \times \left( \frac{A_{B_{Cd}}}{A_{V_{Cd}}} \times A_{V_{Cd}} - A_{V_{Cd}} \right) \quad (4.14)$$

Replacing  $\frac{A_{B_{Cs}}}{A_{V_{Cs}}}$  and  $\frac{A_{B_{Cd}}}{A_{V_{Cd}}}$  with the numerical values from the Calzetti and Cardelli Models, respectively, (see Figure 4.2) we have

$$1.1229 \times A_{V_{Cs}} - A_{V_{Cs}} = 0.44 \times (1.3245 \times A_{V_{Cd}} - A_{V_{Cd}}) \quad (4.15)$$

which is finally reduced to the simple relation

$$A_{V_{Cs}} = 1.1618 \times A_{V_{Cd}} \quad (4.16)$$

Finally, assuming the Calzetti Extinction Model, we calculate  $\frac{A_\lambda}{A_V}$  for the values of  $\lambda$  used in the population models. From this, we can calculate  $\tau_\lambda$  using the relationship in Equation 4.9.

Ultimately, what we really want to compare for the energy balance is the light which has been absorbed by the dust, the extinguished light, not the unextinguished light. We find the extinguished light by solving Equation 4.2 for  $F(\lambda)_{\text{ext}}$  which gives us the following relation

$$F(\lambda)_{\text{ext}} = F(\lambda)_{\text{true}} - F(\lambda)_{\text{obs}} \quad (4.17)$$

so that

$$F(\lambda)_{\text{ext}} = F(\lambda)_{\text{obs}} \times (e^{\tau_\lambda} - 1) \quad (4.18)$$

Knowing  $F(\lambda)_{\text{obs}}$  and  $\tau_\lambda$  (from Equation 4.9 above), we calculate  $F(\lambda)_{\text{ext}}$ . We will use this quantity,  $F(\lambda)_{\text{ext}}$ , as the input for our energy balance analysis.

#### 4.1.5 Comparison of Star Formation Indicators

To proceed at this point, it is necessary to prove that  $\text{Br}\gamma$  is the best star formation indicator. For this reason, we perform a test on a galaxy in our sample which should allow us to demonstrate that  $\text{Br}\gamma$  is the superior star formation indicator. We perform this part of the analysis on the galaxy for which we have the most complete data set (i.e., the galaxy for which the largest number of different hydrogen emission line images are available): NGC 2403.

For NGC 2403, we identified as many H II regions as we can in the  $\text{H}\alpha$  images. We used data from the study by Sivan et al. (1990) to verify the identities of the 200 regions we found. In Figures 4.3 and 4.4, we show several plots which demonstrate that  $\text{Br}\gamma$  is the best star formation indicator. Plotted on the x-axis is the  $A_V$  determined using all hydrogen emission lines, as described above. On the y-axis is the  $A_V$  determined from a single hydrogen line ratio. It is easy to see that the correlation is best when comparing the  $A_V$  determined from all line ratios to that determined from the  $\text{Br}\gamma/\text{H}\beta$  line ratio. We show this comparison for both the Cardelli (Figure 4.3) and the Calzetti Models (Figure 4.4) to demonstrate that  $\text{Br}\gamma$  is the better tracer



### $A_V$ plots for NGC 2403 - Cardelli Model

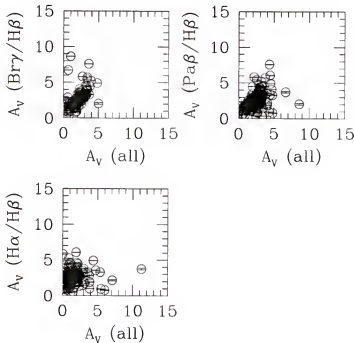


Figure 4.3: The x-axis is the  $A_V$  determined using all hydrogen emission lines; on the y-axis is the  $A_V$  determined from a single hydrogen line ratio. Note that in the  $A_V(\text{Br}\gamma/\text{H}\beta)$  vs.  $A_V(\text{all})$  plot (upper left) the scatter is the lowest of all three plots.

of star formation independent of the extinction law used. This is also easily seen in Table 4.1 since the correlation is best for the  $A_V$  determined from the  $\text{Br}\gamma/\text{H}\beta$  ratio than for the  $A_V$  determined from any other ratio.

#### 4.1.6 Bolometric Population Correction

In order to complete the Energy Balance Analysis, we now need to define the quantities we will compare. To adequately compare input and output energies, we want each band to represent the extinguished bolometric flux of a *population* of stars. We have shown how we calculated the extinguished flux for a given band in section 4.1.4 above. Now we will show how we correct this flux to represent the bolometric flux of a population. We call this correction the bolometric population correction.

$A_V$  plots for NGC 2403 - Calzetti Model

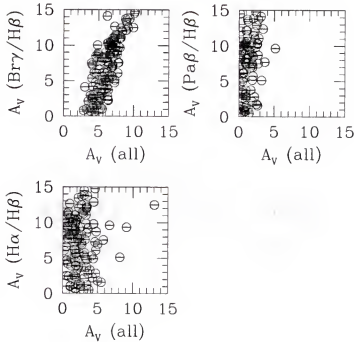


Figure 4.4: This is the same plot as in Figure 4.3, but for the Calzetti Model. Again, note that in the  $A_V(\text{Br}\gamma/\text{H}\beta)$  vs.  $A_V(\text{all})$  plot (upper left) the scatter is the lowest of all three plots.

For the “very young” population, since we are using reprocessed starlight in the form of gas emission lines to assess the stellar population content, we must convert the observed emission line fluxes into stellar fluxes which can be represented by the model. We start with a relationship between the number of line photons and the number of Lyman Continuum photons. The canonical relationship is

$$N_{\text{LyC}} = 1.5 \times N_{\text{H}\alpha} \quad (4.19)$$

To derive the relationship between  $N_{\text{LyC}}$  and the other hydrogen emission lines, we use the relationship

$$F_\lambda = N_\lambda \times E_\lambda \quad (4.20)$$

Table 4.1: Correlation Coefficients

Ratio	Cardelli	Calzetti
$\frac{H\alpha}{H\beta}$	0.565	0.506
$\frac{Pa\beta}{H\beta}$	0.458	0.243
$\frac{Br\gamma}{H\beta}$	0.048	0.008

The Correlation coefficients for the relationship between  $A_V$  determined from all three ratios vs.  $A_V$  determined from the ratio indicated in column (1) for the Cardelli Model in column (2) or the Calzetti Model in column (3).

Table 4.2: Values of  $N_\lambda$  Relative to  $N_{LyC}$ 

$\lambda$	$N_{LyC}/N_\lambda$	$F_{LyC}/F_\lambda$
H $\alpha$	1.5	24.044
H $\beta$	5.8	263.733
Pa $\beta$	13.6	3874.429
Br $\gamma$	47.1	78289.9

Derived values for the ratio of the number of Lyman Continuum photons to the number of photons at the wavelength of the line given in column (1) and the ratio of the flux of the Lyman Continuum to the flux of the line given in column (1).

where  $F_\lambda$  is the flux at a wavelength,  $\lambda$ ,  $N_\lambda$  is the number of photons at that wavelength, and  $E_\lambda$  is the energy of a photon of that wavelength. We know that

$$E_\lambda = \frac{h c}{\lambda} \quad (4.21)$$

where  $h$  is Planck's constant and  $c$  is the speed of light. Knowing these simple relations and knowing the theoretical line ratios for the hydrogen emission lines we observed, we can derive the relationship between  $N_{LyC}$  and  $N_{H\beta}$ ,  $N_{Pa\beta}$  and  $N_{Br\gamma}$  (see Table 4.2).

With the above information, we can derive values for the Lyman Continuum flux,  $F_{\text{LyC}}$ , using the relation

$$F_{\text{LyC}} = 2.18 \times 10^{-11} \times N_{\text{LyC}} \frac{\text{ergs}}{\text{sec cm}^2} \quad (4.22)$$

where the factor is the average energy of a Lyman Continuum photon. In Table 4.2, we have also listed the values of  $F_{\text{LyC}}/F_{\lambda}$  for each of the hydrogen lines studied. To convert this to a bolometric flux, we simply normalize the Lyman Continuum flux of the model to the Lyman Continuum flux calculated from the relation above.

For the old and young populations, we convert the extinguished flux into a bolometric flux using the population models discussed in section 4.1.2. These models are simply energy distributions with respect to wavelength for the different model stellar populations. We can normalize these distributions to  $F(\lambda)_{\text{obs}}$ , convert to extinguished flux and integrate over all wavelengths to arrive at a bolometric extinguished flux which represents an entire population (see Equation 4.23, below).

$$F_{\text{ext,bol,pop}} = \frac{F(\lambda_c)_{\text{obs}}}{F(\lambda_c)_{\text{pop}}} \times \int F(\lambda)_{\text{pop}} \times (e^{\tau_{\lambda}} - 1) d\lambda \quad (4.23)$$

Here,  $F_{\text{ext,bol,pop}}$  is the extinguished, bolometric, population corrected flux.  $F(\lambda_c)_{\text{obs}}$  is the observed flux at the central wavelength ( $\lambda_c$ ) of the band in question.  $F(\lambda_c)_{\text{pop}}$  is the flux at the central wavelength of the band in question given by the population model. (N.B. The population model is a spectral energy distribution with units of luminosity density, so to convert to a flux, we must multiply by the width of the band in which the observation is taken, to get a luminosity; then we must multiply by the factor  $4\pi D^2$  to go from luminosity to flux.) These two fluxes are used to normalize the energy distribution so that it will represent the observed data.  $F(\lambda)_{\text{pop}}$  is the flux at a given wavelength defined by the population model and  $\tau_{\lambda}$  is the extinction at a given wavelength.

We calculate a flux from each band considered which is the extinguished bolometric flux representative of the corresponding population. This is the input into the energy balance analysis. We will compare this to the far infrared flux in each region. We assume that the flux which is extinguished is completely absorbed, which, of course, is not truly the case. Much of the flux will be scattered, not absorbed and reradiated in the far infrared. However, since we are looking at the bolometric extinguished flux, the conversion from extinguished to absorbed flux will be the same for each population. This way, we do not have to make any assumptions about how the dust absorbs light or what fraction of the extinguished light is absorbed. What we are studying is a limiting case; if all the extinguished light were re-radiated in the far infrared, our results would be exactly correct.

#### 4.2 Aperture Photometry

To eliminate any bias that might be introduced through aperture selection, aperture selection was performed separately on each of the hydrogen line, ultraviolet, continuum and far infrared images. We chose apertures to be located on or near bright regions. We checked to make sure that no apertures overlapped and that apertures were not coincident (i.e., apertures found in more than one image were used only once). The size of an aperture was set by the radius at which the peak flux of the feature identified decreased by  $1/e$ . In cases where multiple apertures were coincident, the largest non-overlapping aperture was used.

In Appendix B, we have shown the unblurred  $H\alpha$  image of each galaxy with the apertures discussed above overlayed so that one can see where they lie.

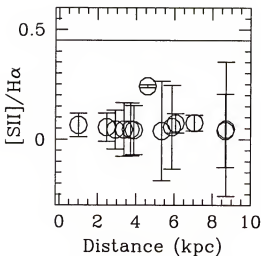
In order to measure the noise in the blurred near infrared and optical images, we took many (80 to 250) apertures in areas where there were no apparent features and averaged the counts detected for each aperture size. We used the root mean square (rms) noise of the counts in the apertures as the noise for a given aperture size.

## CHAPTER 5 RESULTS

In this chapter we present the results of the energy balance analysis for each galaxy. The data for each galaxy are presented together, for continuity. Some plots may be duplicated later in another chapter for comparison.

### 5.1 NGC 2403

$\frac{[\text{SII}]}{\text{H}\alpha}$  Plot for NGC 2403



$\frac{[\text{OIII}]}{\text{H}\alpha}$  Plot for NGC 2403

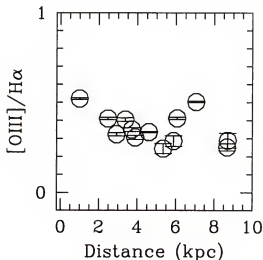


Figure 5.1: The ratio of [SII] to  $\text{H}\alpha$  fluxes for the 13 regions analyzed in NGC 2403. Regions above the line ( $\frac{[\text{SII}]}{\text{H}\alpha} = 0.45$ ), contain supernova remnants. Galactocentric distance is in kiloparsecs.

Figure 5.2: The ratio of [OIII] to  $\text{H}\alpha$  fluxes for each of the 13 regions analyzed in NGC 2403. This ratio is used to trace metallicity gradients and ionization levels. Galactocentric distance is given in kiloparsecs.

This galaxy has the most complete data set. We have data for each of the four hydrogen recombination lines, as well as [OIII], [SII] and UV data.

Table 5.1: Positions and Fluxes for NGC 2403

Region	Position	$F_{\text{Br}\gamma}$	$F_{\text{UV}}$	$F_{2.14\mu\text{m}}$
1	-382.57, 16.90	136811.	24622.4	264494.
2	-350.66, -135.88	82838.6	16781.5	392233.
3	-339.95, -22.61	219789.	20144.8	643069.
4	-305.37, -167.77	165459.	25561.3	834566.
5	-149.16, -305.51	. . .	440.555	235944.
6	-124.42, -240.45	50849.1	4514.35	300628.
7	-117.37, 48.42	403722.	74315.2	0.412175E+07
8	-19.41, 0.10	133934.	13924.1	607016.
9	68.54, 69.72	. . .	. . .	. . .
10	-382.93, 606.24	15823.3	310.217	. . .
11	-370.58, 137.75	. . .	. . .	. . .
12	-364.87, 134.28	. . .	. . .	. . .
13	-361.37, 208.76	437112.	54880.1	0.238468E+07
14	-277.30, 227.92	47712.4	6192.78	188671.
15	-181.10, 203.44	530094.	17755.3	0.209907E+07
16	-126.89, 499.58	23957.2	19376.8	83233.4
17	-113.07, 328.90	61232.5	22748.2	509873.
18	-69.14, 508.67	15692.9	1824.99	4167.13

The columns are as follows: (1) the region number of each object, (2) the position offset from the center in arcseconds for each region (x, y), (3) the Br $\gamma$  flux observed in  $10^{18}$  erg sec $^{-1}$  cm $^{-2}$ , (4) the UV flux observed in  $10^{18}$  erg sec $^{-1}$  cm $^{-2}$ , (5) the 2.14  $\mu\text{m}$  flux observed in  $10^{18}$  erg sec $^{-1}$  cm $^{-2}$ .

After blurring the images, we identified 18 regions for analysis (see Table 5.1).

Of these, 13 had data in the three bands used in our analysis (Br $\gamma$ , UV, 2.14  $\mu\text{m}$  continuum, 60  $\mu\text{m}$  and 100  $\mu\text{m}$  bands). We also analyzed the [SII] data for these regions, using  $\frac{[\text{SII}]}{\text{H}\alpha}$  as an indicator for supernova remnants (see Figure 5.1). Here, it is clear that all of the regions analyzed have a  $\frac{[\text{SII}]}{\text{H}\alpha}$  ratio which is lower than expected for a supernova remnant. (For a supernova remnant  $\frac{[\text{SII}]}{\text{H}\alpha} \geq 0.45$ .)

Looking at the [OIII] data for the same 13 regions (Figure 5.2), the  $\frac{[\text{OIII}]}{\text{H}\alpha}$  ratios are comparable to those of typical H II regions ( $0.0 \leq \frac{[\text{OIII}]}{\text{H}\alpha} \leq 1.0$ ).

## Hydrogen Line Ratios for NGC 2403

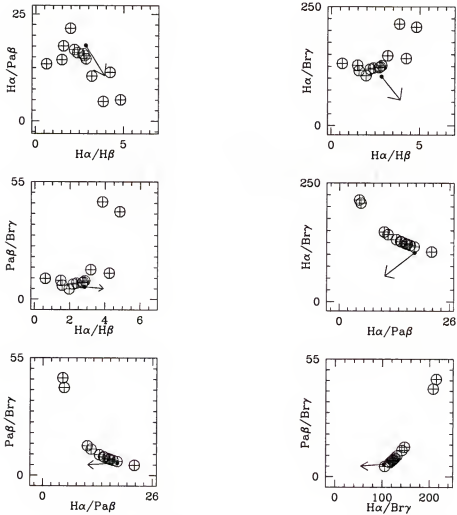


Figure 5.3: The hydrogen recombination line ratios used in determining the extinction. The filled circles with arrows are the theoretical expected values for the ratios, assuming case B (Baker & Menzel 1938) recombination. The arrows indicate the direction in which reddening would change the ratios.

Since we have data for all four hydrogen emission lines, we have plotted the line ratios relative to one another to investigate the problem of larger and smaller than expected ratios. In Figure 5.3, we have a montage of several possible ratios plotted against one another. We can see that there are several regions for which the ratios are larger and smaller than expected. In Figure 5.4, we show each of the four analytical ratios ( $\frac{H\alpha}{H\beta}$ ,  $\frac{H\alpha}{Pa\beta}$ ,  $\frac{H\alpha}{Br\gamma}$ , and  $\frac{Pa\beta}{Br\gamma}$ ) plotted versus galactocentric distance to



show that there does seem to be a trend of increasing value for increasing distance for three of the ratios studied:  $\frac{H\alpha}{H\beta}$ ,  $\frac{H\alpha}{Br\gamma}$ , and  $\frac{Pa\beta}{Br\gamma}$ .

From the above ratios, we can calculate extinction, as described in Chapter 4. In Table 5.2, we have listed the extinctions derived for each of the 18 regions analyzed.

Additionally, we have calculated the star formation rates for each of the four hydrogen emission lines. To do this, we took the equation from Kennicutt (1983)

#### Hydrogen Line Ratios vs. Distance for NGC 2403

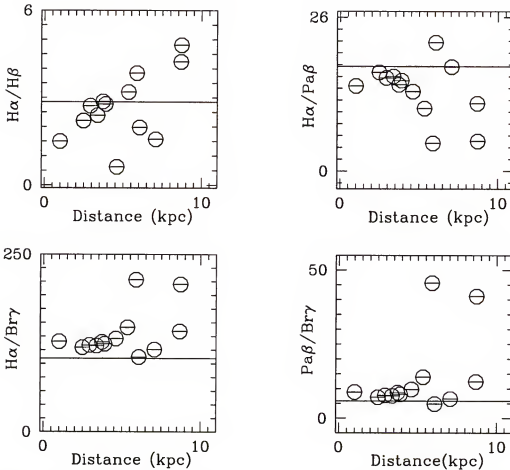


Figure 5.4: The hydrogen recombination line ratios versus galactocentric distance in kiloparsecs. Some ratios are nonphysical; this may be due to the large apertures we use in our analysis. Such large apertures imply a constant extinction over a physically large region, which is not realistic. Some of the ratios exhibit a trend with distance.

Table 5.2: Extinctions for NGC 2403

Region	$A_V$	Error	N
1	2.646	0.00007	3.0
2	2.671	0.00011	3.0
3	3.100	0.00008	3.0
4	2.864	0.00009	3.0
5	2.720	0.00000	2.0
6	2.035	0.00025	3.0
7	3.265	0.00012	3.0
8	3.245	0.00005	3.0
9	2.720	0.00000	0.0
10	2.564	0.00066	3.0
11	2.720	0.00000	0.0
12	2.720	0.00000	0.0
13	3.623	0.00003	3.0
14	3.360	0.00006	3.0
15	4.344	0.00015	3.0
16	1.352	0.00057	3.0
17	1.752	0.00060	3.0
18	2.397	0.00022	3.0

The columns are as follows: (1) the region number, (2) the extinction,  $A_V$  in magnitudes, (3) the error in  $A_V$ , and (4) the the number of ratios used in the calculation. In cases where this number is zero, we have substituted an average value for  $A_V$ .

$$\text{SFR}(M \geq 10 M_{\odot}) = \frac{L_{\text{H}\alpha}}{7.02 \times 10^{41}} (M_{\odot} \text{ yr}^{-1}) \quad (5.1)$$

In Figure 5.5, we show the star formation rate for  $\text{H}\beta$ ,  $\text{H}\alpha$ ,  $\text{Pa}\beta$  and  $\text{Br}\gamma$  plotted versus galactocentric distance. In each band, there is no trend in star formation rate with distance from the center. Also, the star formation rates, as calculated from the  $\text{H}\beta$  data, are higher than those calculated using the other hydrogen emission lines. This is most likely due to the fact that  $\text{H}\beta$  is the line with the shortest wavelength and is, therefore, most sensitive to overestimates in extinction. If the star formation

rates are high when calculated using  $H\beta$  due to an overestimate in extinction, it does not affect our results since the overestimate in extinction will carry into every population we evaluate.

### Star Formation Rates for NGC 2403

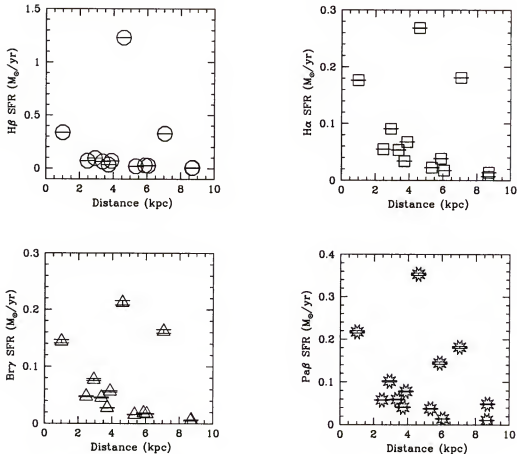


Figure 5.5: The star formation rates calculated from each of the three hydrogen recombination lines. It is easy to see that the star formation rates are similar, for the  $H\alpha$ ,  $Pa\beta$  and  $Br\gamma$  data. Note, however, that the star formation rates derived from the  $H\beta$  data are almost an order of magnitude higher than the others.

The energy balance analysis, using the  $Br\gamma$  flux to represent the very young population, involves a comparison of the population ratios. We define a population ratio as the bolometric extinguished flux over the flux in far infrared for a given band. That is, the “very young” population ration (VYP) is given by:

Table 5.3: Population Ratios for NGC 2403

Region	VYP	YP	OP
1	0.106682E+09	62.3078	422.338
2	0.381002E+09	125.238	1847.07
3	0.204362E+09	20.2618	408.137
4	0.468306E+09	58.6955	1209.25
5	. . .	25.6092	8654.41
6	0.861265E+09	45.1158	1895.81
7	0.187557E+09	17.2369	603.246
8	0.522028E+09	23.4829	645.974
9	. . .	. . .	. . .
10	. . .	. . .	. . .
11	. . .	. . .	. . .
12	. . .	. . .	. . .
13	0.931299E+08	18.9725	520.202
14	0.126083E+10	177.025	3403.18
15	0.141393E+10	38.4224	2866.27
16	0.366494E+09	192.391	521.475
17	0.123737E+09	24.8632	351.645
18	0.711771E+10	383.746	552.906

The columns are as follows: (1) the region number, (2) the “very young” population ratio,  $(\frac{F_{\text{bol,ext}}(\text{Br}\gamma)}{F_{\text{FIR}}})$ , (3) the “young” population ratio  $(\frac{F_{\text{bol,ext}}(\text{UV})}{F_{\text{FIR}}})$ , (4) the “old” population ratio  $(\frac{F_{\text{bol,ext}}(2.14 \mu\text{m})}{F_{\text{FIR}}})$

$$\text{VYP} = \frac{F_{\text{bol,ext}}(\text{Br}\gamma)}{F_{\text{FIR}}} \quad (5.2)$$

and the “young” population ratio (YP) is given by

$$\text{YP} = \frac{F_{\text{bol,ext}}(\text{UV})}{F_{\text{FIR}}} \quad (5.3)$$

and the “old” population ratio (OP) is given by

$$OP = \frac{F_{\text{bol,ext}}(2.14 \mu\text{m})}{F_{\text{FIR}}} \quad (5.4)$$

A comparison of the population ratios for the 13 regions considered results in the conclusion that all regions are heated predominantly by a “very young” population. This may seem contradictory, given the finding that most of the regions have  $\frac{[\text{SII}]}{\text{H}\alpha}$  ratios indicative of supernova remnants; however, it is likely that in the case of this galaxy, the supernova remnants are from the same recent epoch of star formation which is producing the Br $\gamma$  radiation. Also, one can see from Table 5.3 that the “very young” population is dominant over the other populations by several orders of magnitude so that a small error in extinction or in our assumptions would not change the outcome of this analysis. If we use H $\alpha$  instead of Br $\gamma$  to represent

Population vs. Color Temperature

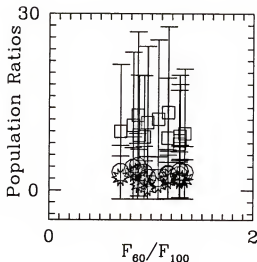


Figure 5.6: The population ratios versus color temperature for each region for NGC 2403. The triangles represent the H $\alpha$  data, the squares represent the Br $\gamma$  data, the stars represent the UV data and the circles represent the continuum (2.14  $\mu\text{m}$ ) data.

Color Temperature vs. Distance

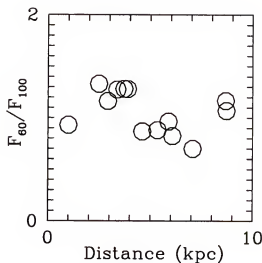


Figure 5.7: The color temperature for each region versus distance for NGC 2403. Color temperature is calculated using the ratio of the flux at 60  $\mu\text{m}$  to the flux at 100  $\mu\text{m}$ . The galactocentric distance is given in kiloparsecs.

the “very young” population, we find that 14 regions have data in the three bands used for the analysis. The dominance in  $H\alpha$  is of the same order of magnitude as that seen in  $Br\gamma$ .

In addition to the above energy balance analyses, we examine the relationship between dominant heating population and the temperature of the dust. A measure of the dust temperature can be derived from color temperature which is derived from and directly proportional to the ratio of  $60\ \mu\text{m}$  to  $100\ \mu\text{m}$  IRAS fluxes. In Figure 5.6, we plot the population ratios for each region versus the  $60\ \mu\text{m}$  to  $100\ \mu\text{m}$  flux ratio. In this plot, the triangles represent the  $H\alpha$  data, the squares represent the  $Br\gamma$  data, the stars represent the UV data, and the circles represent the continuum ( $2.14\ \mu\text{m}$ ) data. Clearly, the range in color temperature is large; whereas, the dominant heating population is always the “very young” population by several *orders of magnitude*.

#### Luminosity Functions for NGC 2403

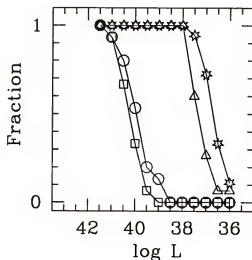


Figure 5.8: The luminosity functions for the four different recombination lines of hydrogen used in the analysis for NGC 2403. The circles represent the  $H\beta$  data, the squares represent the  $H\alpha$  data, the stars represent the  $Pa\beta$  data, and the triangles represent the  $Br\gamma$  data.

The fact that we don't see a trend in color temperature could be due to many possible factors. First, it may be that this galaxy has a range of sizes of dust grains. If this is so, we would expect to see an essentially uniform temperature distribution throughout the galaxy. Another reason might be the size of the regions we are evaluating. They may still be too large to really see a trend in color temperature.

Further, we have plotted in Figure 5.7 the  $60\ \mu\text{m}$  to  $100\ \mu\text{m}$  flux ratio versus galactocentric distance to examine the possibility of a trend of cooling with increasing galactocentric distance. We would expect such a trend if the dust grains which emitted far infrared radiation were all the same size. For NGC 2403, there may be a *slight* decrease in color temperature with increasing radial distance from the center. The slope of a linear fit is  $-0.029 \pm 0.001$ ; so while it is slightly negative, it is nearly flat, also.

Finally, we compare the luminosity functions for the different hydrogen recombination line bands. We plot the luminosity functions for the 13 regions in Figure 5.8. The circles represent the  $\text{H}\beta$  data, the squares represent the  $\text{H}\alpha$  data, the stars represent the  $\text{Pa}\beta$  data, and the triangles represent the  $\text{Br}\gamma$  data. We expect that, the  $\text{Br}\gamma$  data must be  $\approx 100$  times deeper than the  $\text{H}\alpha$  data since the expected  $\frac{\text{H}\alpha}{\text{Br}\gamma}$  theoretical ratio is 104. If the  $\text{Br}\gamma$  data is *not* 104 times deeper than the  $\text{H}\alpha$  data, we did not detect all the H II regions in  $\text{Br}\gamma$  that we did in  $\text{H}\alpha$ . Thus, the data farthest to the left in Figure 5.8 should be the  $\text{H}\alpha$  data. Following that, moving to the right, should be the  $\text{H}\beta$  data at least 3 times fainter in luminosity. The  $\text{Pa}\beta$  data should be at least 17.7 times fainter in luminosity and  $\text{Br}\gamma$  should be at least 104 times fainter. For NGC 2403, the  $\text{Br}\gamma$  data is actually 1000 times fainter than the  $\text{H}\alpha$  data, and the  $\text{Pa}\beta$  data is even better than that.

### 5.2 NGC 6946

For NGC 6946, we have  $H\beta$ ,  $H\alpha$  and  $Br\gamma$  data, as well as  $[OIII]$  data. After blurring the images, we identified 14 regions for analysis (see Table 5.4). Of these, 13 had data in the two bands used in our analysis ( $Br\gamma$  and  $2.14 \mu m$  continuum).

$\frac{[OIII]}{H\alpha}$  Plot for NGC 6946

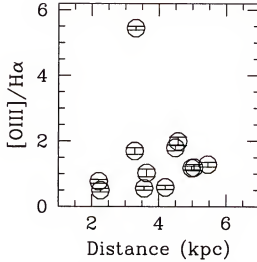


Figure 5.9: The ratio of the  $[OIII]$  to  $H\alpha$  fluxes for each of the 13 regions analyzed in NGC 6946.

The  $[OIII] / H\alpha$  ratios for these 13 regions (Figure 5.9) are high for typical H II regions ( $0.0 \leq \frac{[OIII]}{H\alpha} \leq 1.0$ ). The highest  $\frac{[OIII]}{H\alpha}$  ratio one might expect for an H II region is about 3.0. Only one of the regions analyzed falls above this mark. However, the high  $\frac{[OIII]}{H\alpha}$  ratio is indicative of either a high ionization state or high metallicity. Unfortunately, we had no  $[SII]$  data for this galaxy to compare the values for supernova remnants.

Since we have data for three hydrogen emission lines, we have plotted the values of the two ratios used for calculating the extinction ( $\frac{H\alpha}{H\beta}$  and  $\frac{H\alpha}{Br\gamma}$ ) for each of the 13 regions used in the analysis in Figure 5.10. Here we can see that while the  $\frac{H\alpha}{H\beta}$  ratios are systematically low, the  $\frac{H\alpha}{Br\gamma}$  ratios are systematically higher than expected.



Table 5.4: Positions and Fluxes for NGC 6946

Region	Position	$F_{\text{Br}\gamma}$	$F_{2.14\mu\text{m}}$
1	160.14, 84.98	0.404038E-10	0.138155E-09
2	290.94, 99.77	0.259763E-11	0.341133E-10
3	95.08, 193.66	0.209876E-11	0.672685E-10
4	338.76, 1.38	0.262433E-11	0.236460E-10
5	274.69, -19.89	0.340309E-11	0.385734E-10
6	171.50, 175.24	0.426981E-11	0.333136E-10
7	30.07, 130.88	0.466744E-12	0.174662E-10
8	178.82, 0.83	0.386058E-11	0.403327E-10
9	305.85, 185.11	0.796588E-12	0.118921E-10
10	386.65, 83.21	...	...
11	95.35, 133.26	0.507261E-11	0.246611E-10
12	103.21, 43.47	0.391104E-11	0.198234E-10
13	310.15, 50.86	0.126789E-11	0.173589E-10
14	209.75, 143.31	0.406205E-11	0.215151E-10

The columns are as follows: (1) the region number of each object, (2) the position offset from the center in arcseconds for each region (x, y), (3) the Br $\gamma$  flux observed in  $\text{erg sec}^{-1} \text{cm}^{-2}$ , (4) the 2.14  $\mu\text{m}$  flux observed in  $\text{erg sec}^{-1} \text{cm}^{-2}$ .

In Figure 5.11 we show each of the two analytical ratios plotted versus distance to show that there is no trend of these values with distance.

In Table 5.5 we list the extinction calculated for each region as well as the number of ratios used in the calculation. In cases where the number of ratios is zero, we have substituted the average value of the extinctions calculated for the regions analyzed. Since we are using only three lines (two ratios) for this calculation, and since two of the three lines are in the optical regime, our calculation of extinction is strongly influenced by extinction in the optical. As a result, we may have systematically overestimated the extinction which would effectively increase the H $\alpha$  and H $\beta$  fluxes. Extinction should decrease in effect with increasing galactocentric distance, due to decreasing amounts of dust (Keel & White 1999). We do not see this effect.

## Hydrogen Line Ratios for NGC 6946

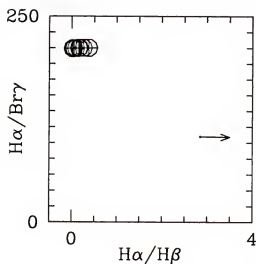


Figure 5.10: The  $\frac{H\alpha}{H\beta}$  and  $\frac{H\alpha}{Br\gamma}$  ratios used in determining the extinction. The filled circle with and arrow is the theoretical expected value for both ratios, assuming case B recombination. The arrows indicated the direction in which reddening would change the ratios.

## Hydrogen Line Ratios vs. Distance for NGC 6946

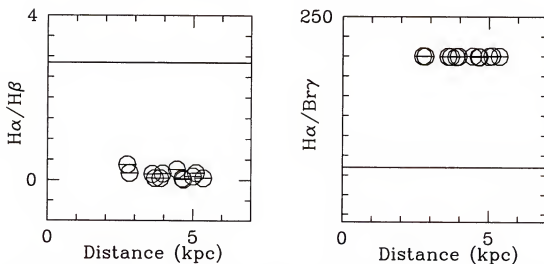


Figure 5.11: The two hydrogen recombination line ratios plotted versus galactocentric distance in kiloparsecs. While some ratios are systematically high and others are systematically low, neither of the ratios exhibit a trend with distance.

Table 5.5: Extinctions for NGC 6946

Region	$A_V$	Error	N
1	9.403	0.0000	2.0
2	6.343	0.0000	2.0
3	6.813	0.0000	2.0
4	7.475	0.0000	2.0
5	5.973	0.0000	2.0
6	7.331	0.0000	2.0
7	5.134	0.0000	2.0
8	6.905	0.0000	2.0
9	8.126	0.0000	1.0
10	8.126	0.0000	0.0
11	9.804	0.0000	2.0
12	8.893	0.0000	2.0
13	6.899	0.0000	2.0
14	8.742	0.0000	2.0

The extinctions calculated for each region in NGC 6946. The columns are as follows: (1) the region number, (2) the extinction,  $A_V$  in magnitudes, (3) the error in  $A_V$ , and (4) the number of ratios used in the calculation. In cases where this number is zero, we have substituted an average value for  $A_V$ .

Therefore, we can infer that our data for this galaxy do not indicate a decrease in dust content with increasing galactocentric distance.

Additionally, we have calculated the star formation rates for each of the three hydrogen emission lines as described in Section 5.1. In Figure 5.12, we show the log of the star formation rate for  $H\beta$ ,  $H\alpha$  and  $Br\gamma$  plotted versus galactocentric distance. While the star formation rates calculated using the  $H\alpha$  and  $Br\gamma$  data give similar results, the star formation rates calculated from the  $H\beta$  data are much higher. This may be indicative of a poor estimate for extinction.

The energy balance analysis, using the  $Br\gamma$  flux to represent the “very young” population, through a comparison of population ratios defined in Section 5.1, results

## Star Formation Rates for NGC 6946

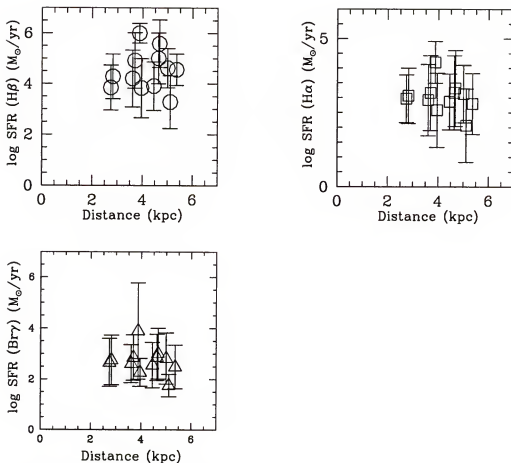


Figure 5.12: The logs of the star formation rates calculated from each of the three hydrogen recombination lines. It is easy to see that the star formation rates are similar, regardless of which line is used for the calculation. Note, however, that the star formation rates derived from the  $H\beta$  data are almost an order of magnitude higher than the others.

in the conclusion that all 13 regions are heated by a “very young” population. We have listed the population ratios for each of the regions analyzed in Table 5.6. If we use  $H\alpha$  instead of  $Br\gamma$  to represent the “very young” population, we still find that all 13 regions are heated by the “very young” population.

In addition to the energy balance analysis, we examine the relationship between dominant heating population and color temperature. In Figure 5.13, we plot the population ratios for each region versus color temperature. The squares represent

Table 5.6: Population Ratios for NGC 6946

Region	VYP	OP
1	0.876960E+26	0.136727E+07
2	0.927057E+17	44477.4
3	0.662965E+19	672427.
4	0.522785E+21	476436.
5	0.199223E+17	56428.0
6	0.152164E+21	253138.
7	0.211914E+15	154766.
8	0.760328E+19	156173.
9	0.243455E+23	0.124461E+07
11	0.358449E+28	0.999323E+07
12	0.881604E+25	0.285487E+07
13	0.567480E+19	157480.
14	0.113294E+25	839764.

The columns are as follows: (1) the region number, (2) the “very young” population ratio, ( $\frac{F_{\text{bol,ext}}(\text{Br}\gamma)}{F_{\text{FIR}}}$ ), (3) the “old” population ratio ( $\frac{F_{\text{bol,ext}}(2.14 \mu\text{m})}{F_{\text{FIR}}}$ )

the “very young” population data, the circles represent the “old” population data. It is easy to see that the range in color temperature is large; whereas, the dominant heating population is always the “very young” population by *several orders of magnitude* (see Table 5.6). For NGC 6946, we do not see a trend in color temperature with dominant heating population. As mentioned above, this could be due to several possible factors including the size of the dust grains and the sizes of our apertures.

Further, we have plotted in Figure 5.14 the color temperature versus galactocentric distance to investigate the possibility of a trend of cooling with increasing galactocentric distance. For NGC 6946, there may be an increase in color temperature with increasing distance. The slope of a linear fit is  $0.075 \pm 0.005$ ; so while the slope is slightly positive, it is nearly flat, also.

Lastly, we compare the luminosity functions for the different hydrogen recom-

## Color Temperature vs. Distance for NGC 6946

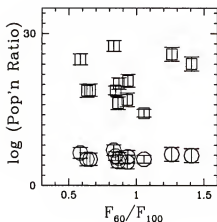


Figure 5.13: The log of the population ratios versus color temperature for NGC 6946.

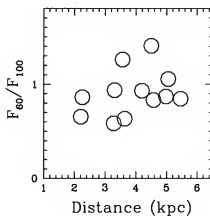


Figure 5.14: The color temperature versus galactocentric distance for NGC 6946.

## Luminosity Function for NGC 6946

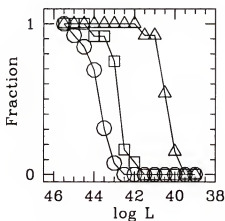


Figure 5.15: Plotted above are the luminosity functions for the three different recombination lines of hydrogen used in the analysis for NGC 6946. The circles represent the  $H\beta$  data, the squares represent the  $H\alpha$  data, the stars represent the  $Pa\beta$  data and the triangles represent the  $Br\gamma$  data.

bination line bands. We plot the luminosity functions for the 13 regions in Figure 5.15. The circles represent the  $H\beta$  data, the squares represent the  $H\alpha$  data, and the triangles represent the  $Br\gamma$  data. As expected, the  $Br\gamma$  data are  $\approx 100$  times deeper than the  $H\alpha$  data. However, we also see that the  $H\beta$  data is not complete enough. This explains the problems noted earlier with the  $\frac{H\alpha}{H\beta}$  flux ratios. For many of the regions evaluated, this ratio was too low, indicating a value for  $H\beta$  which was too high. Since the  $H\beta$  data is not complete enough to have detected all the regions seen in  $H\alpha$  the most likely explanation is that the  $H\beta$  data is not good enough.

### 5.3 NGC 300

$\frac{[SII]}{H\alpha}$  Ratios for NGC 300

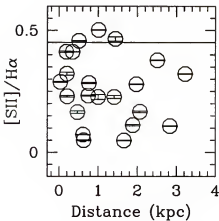


Figure 5.16: The ratio of [SII] to  $H\alpha$  fluxes for each of the 36 regions analyzed in NGC 300. This ratio is used as an indicator of supernova remnants. If the value of the ratio is above 0.45, the object contains a supernova remnant.

$\frac{[OIII]}{H\alpha}$  Ratios for NGC 300

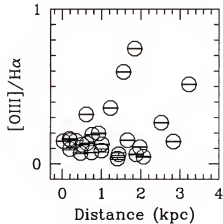


Figure 5.17: The ratio of [OIII] to  $H\alpha$  fluxes for each of the 26 regions analyzed in NGC 300. This ratio can be used to trace supernova remnants and ionization levels. Galactocentric distance is given in kiloparsecs.

For NGC 300, we have  $H\alpha$  and  $Br\gamma$  data, as well as [OIII] and [SII] data. After blurring the images, we identified 38 regions for analysis (see Table 5.7). For 26 of these regions there were data in the  $Br\gamma$ ,  $2.14 \mu m$  continuum, and far infrared bands. We also analyzed these regions, using  $\frac{[SII]}{H\alpha}$  as an indicator for supernova rem-

Table 5.7: Positions and Fluxes for NGC 300

Region	Position	$F_{\text{Br}\gamma}$	$F_{2.14\mu\text{m}}$
1	-14.63, -32.51	0.104492E-10	0.775746E-10
2	-180.31, 6.44	0.115533E-10	0.716766E-11
3	-187.65, -30.60	0.198717E-10	0.383041E-10
4	-228.25, 8.53	0.284999E-10	0.180561E-10
5	-235.05, 48.80	0.193876E-10	...
6	-169.19, 44.01	0.100816E-10	0.571403E-11
7	145.34, 31.21	0.897854E-11	0.184121E-10
8	139.49, -129.32	0.101969E-10	0.656047E-11
9	-218.75, 75.12	0.103806E-10	...
10	-208.41, 114.46	0.971943E-11	...
11	-45.53, -122.73	0.469885E-11	0.240034E-10
12	-13.66, -107.14	0.115975E-10	0.824771E-10
13	-205.27, -100.51	0.431866E-11	0.715735E-11
14	-213.10, -119.72	0.752704E-11	0.240205E-10
15	-117.70, -83.92	...	0.167660E-09
16	-107.07, -56.21	...	0.110923E-09
17	-32.21, -51.33	0.287171E-10	0.265029E-09
18	-154.44, -27.10	0.118122E-10	0.118363E-09
19	-30.57, -10.68	0.232704E-10	0.327197E-09
20	39.91, 2.61	0.102092E-10	0.338428E-09
21	135.96, -8.86	0.613596E-11	0.134413E-09
22	172.63, 51.29	0.143882E-10	0.107715E-09
23	-182.55, 29.22	0.195651E-10	0.218205E-10
24	-181.50, 93.82	0.140272E-10	0.134262E-10
25	-133.37, 116.12	...	0.269850E-09
26	-6.83, 176.90	...	0.413803E-10
27	120.52, 152.45	0.223377E-10	0.379258E-10
28	119.89, 116.29	0.837437E-11	0.573057E-10
29	-45.62, -70.28	0.739548E-11	0.605547E-10
30	33.74, -100.68	...	0.759382E-10
31	3.54, -9.03	0.181073E-10	0.453610E-09
32	-89.80, 127.58	...	0.354136E-09
33	-3.61, 136.01	0.421501E-11	0.150326E-10
34	154.57, 129.16	0.700604E-11	0.152053E-09
35	77.58, -37.32	...	0.286089E-09
36	-12.52, 37.48	0.235337E-10	0.286682E-09
37	-87.08, 33.32	...	0.402154E-09
38	65.15, 164.49	0.297608E-10	...

The columns are as follows: (1) the region number of each object, (2) the position offset from the center in arcseconds for each region (x, y), (3) the Br $\gamma$  flux observed in  $\text{erg sec}^{-1} \text{cm}^{-2}$ , (4) the 2.14  $\mu\text{m}$  flux observed in  $\text{erg sec}^{-1} \text{cm}^{-2}$ .



nants (see Figure 5.16). Clearly, most of the regions analyzed have a  $\frac{[\text{SII}]}{\text{H}\alpha}$  ratio which is *not* indicative of a supernova remnant. (For a supernova remnant,  $\frac{[\text{SII}]}{\text{H}\alpha} \geq 0.45$ .)

Looking at the  $[\text{OIII}]$  data for these 26 regions (Figure 5.17), the  $\frac{[\text{OIII}]}{\text{H}\alpha}$  ratios are normal for typical H II regions ( $0.0 \leq \frac{[\text{OIII}]}{\text{H}\alpha} \leq 1.0$ ). In fact, they may even be considered quite low ratios for typical, evolved H II regions.

Since we have data for only two hydrogen emission lines, we have plotted the  $\frac{\text{H}\alpha}{\text{Br}\gamma}$  corrected flux ratio versus galactocentric distance in Figure 5.18. Our data indicate that the  $\frac{\text{H}\alpha}{\text{Br}\gamma}$  ratios are, within the errors, exactly what is expected. Also, there is no trend of increasing or decreasing ratio with galactocentric distance.

Additionally, we have calculated the star formation rates for each of  $\text{H}\alpha$  and  $\text{Br}\gamma$  using the method outlined in Section 5.1. In Figure 5.19, we show the star formation rate for  $\text{H}\alpha$  and  $\text{Br}\gamma$  plotted versus galactocentric distance. The squares represent the  $\text{H}\alpha$  data and the triangles represent the  $\text{Br}\gamma$  data. The star formation rates calculated from the  $\text{Br}\gamma$  data are similar to those calculated using the  $\text{H}\alpha$  data.

Hydrogen Line Ratio vs. Distance for NGC 300

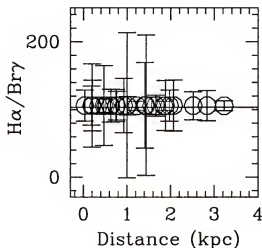


Figure 5.18: The  $\text{H}\alpha/\text{Br}\gamma$  ratio versus galactocentric distance in kiloparsecs. This ratio does not exhibit a trend with distance.

Table 5.8: Extinctions for NGC 300

Region	$A_V$	Error
1	6.453	0.0536
2	7.657	0.0878
3	6.394	0.0668
4	6.610	0.0808
5	7.304	0.1095
6	8.296	0.1422
7	6.497	0.0619
8	7.914	0.1130
9	5.399*	0.0121
10	8.807	0.1994
11	5.373	0.0729
12	3.934	0.0519
13	5.470	0.0809
14	4.759	0.0894
15	5.399*	0.0121
16	5.399*	0.0121
17	4.365	0.0357
18	3.355	0.0685
19	4.898	0.0477
20	3.535	0.0802
21	2.884	0.1279
22	4.421	0.0653
23	5.546	0.0478
24	5.140	0.0556
25	5.399*	0.0121
26	5.399*	0.0121
27	3.584	0.0390
28	3.020	0.0658
29	6.033	0.0604
30	5.399*	0.0121
31	4.732	0.0568
32	5.399*	0.0121
33	6.335	0.1130
34	2.684	0.1111
35	5.399*	0.0121
36	5.179	0.0514
37	5.399*	0.0121
38	5.399*	0.0121

The columns are as follows: (1) the region number, (2) the extinction,  $A_V$  in magnitudes and (3) the error in  $A_V$ . The asterisks denote regions for which we have substituted an average value for  $A_V$ .

## Star Formation Rates for NGC 300

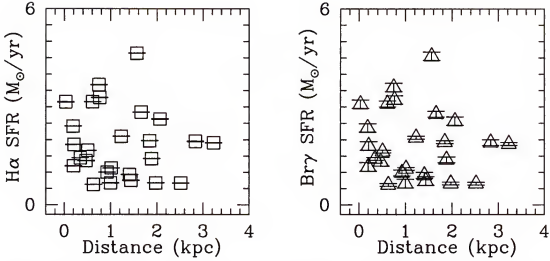


Figure 5.19: The star formation rates calculated from both hydrogen recombination lines. It is easy to see that the star formation rates are similar, regardless of which line is used for the calculation.

The energy balance analysis, using the  $\text{Br}\gamma$  data to represent the “very young” population is performed through a comparison of population ratios defined in Section 5.1. The result of this analysis is that all 26 regions analyzed are heated predominantly by a “very young” population. We have listed the population ratios for each of the regions analyzed in Table 5.9. If we use  $\text{H}\alpha$  instead of  $\text{Br}\gamma$  to represent the “very young” population, we find that all 26 regions are still heated by the “very young” population.

In addition to the above energy balance analysis, we test the relationship between dominant heating population and color temperature. In Figure 5.20, we plot the log of the population ratio for each region versus the  $F_{60\ \mu\text{m}}/F_{100\ \mu\text{m}}$  ratio. The squares represent the  $\text{Br}\gamma$  data and the circles represent the continuum ( $2.14\ \mu\text{m}$ ) data. Clearly, there is no relationship between color temperature and dominant heating population. For NGC 300, color temperature can not be used to determine a dominant heating population.

Table 5.9: Population Ratios for NGC 300

Region	VYP	OP
1	0.325702E+22	11636.9
2	0.813529E+25	4617.03
3	0.111675E+22	1407.88
4	0.297468E+22	400.995
5	0.646047E+24	. . .
6	0.431678E+27	8086.26
7	0.342719E+22	2685.89
8	0.104571E+27	16240.2
9	0.932602E+19	. . .
10	. . .	. . .
11	0.224410E+19	1514.33
12	0.241728E+15	375.862
13	0.815851E+19	1077.89
14	0.256400E+17	259.199
15	. . .	762.736
16	. . .	1128.13
17	0.132137E+16	294.331
18	0.243658E+13	100.416
19	0.371071E+17	806.861
20	0.547194E+13	300.488
21	0.695075E+11	65.2271
22	0.792952E+15	107.203
23	0.568838E+19	341.325
24	0.599861E+18	253.493
25	. . .	168.221
26	. . .	. . .
27	0.293529E+14	64.6920
28	0.637879E+12	95.2734
29	0.127521E+21	4482.54
30	. . .	2128.47
31	0.129452E+17	1178.64
32	. . .	577.845
33	0.127787E+22	4048.26
34	0.534878E+11	132.527
35	. . .	2008.98
36	0.423966E+18	1868.01
37	. . .	559.241
38	0.917058E+16	. . .

The columns are as follows: (1) the region number, (2) the “very young” population ratio, ( $\frac{F_{\text{bol,ext}}(\text{Br}\gamma)}{F_{\text{FIR}}}$ ), (3) the “old” population ratio ( $\frac{F_{\text{bol,ext}}(2.14 \mu\text{m})}{F_{\text{FIR}}}$ )

Color Temperature vs. Population Ratio  
for NGC 300

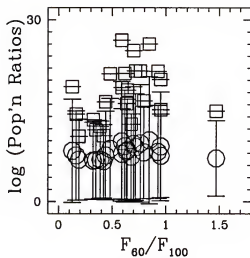


Figure 5.20: The population ratios versus color temperature for NGC 300.

Color Temperature vs. Distance for  
NGC 300

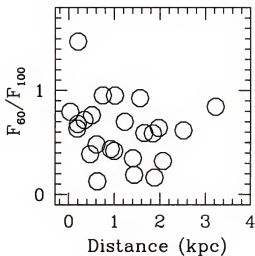


Figure 5.21: The color temperature plotted versus distance for NGC 300.

Luminosity Function for NGC 300

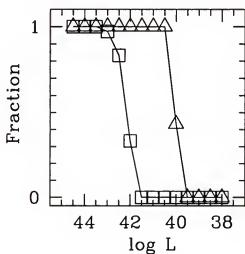


Figure 5.22: The luminosity functions for the three different recombination lines of hydrogen used in the analysis for NGC 300.

Further, we have plotted in Figure 5.21 the  $F_{60\ \mu m}/F_{100\ \mu m}$  ratio versus galactocentric distance to investigate the possibility of a trend of decreasing color temperature with increasing distance. For NGC 300, there may be a slight decrease in color temperature with increasing distance. The slope of a linear fit is  $-0.069 \pm 0.006$ ; while it is slightly negative, it is also nearly flat.

Lastly, we compare the luminosity functions for  $H\alpha$  and  $Br\gamma$ . We plot the luminosity functions for the 26 regions in Figure 5.22. Here, we can see that, as expected, the  $Br\gamma$  data are  $\approx 100$  times deeper than the  $H\alpha$  data.

#### 5.4 NGC 628

$\frac{[SII]}{H\alpha}$  Plot for NGC 628

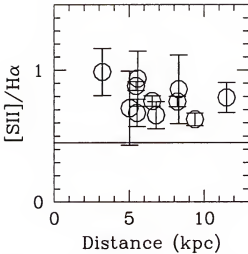


Figure 5.23: The  $\frac{[SII]}{H\alpha}$  flux ratios for the 11 regions analyzed in NGC 628. The line in the plot indicates where  $\frac{[SII]}{H\alpha} = 0.45$ . Regions with a value greater than 0.45, contain supernova remnants.

$\frac{[OIII]}{H\alpha}$  Plot for NGC 628

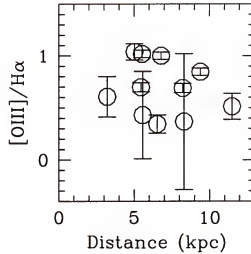


Figure 5.24: The  $\frac{[OIII]}{H\alpha}$  flux ratio's for the 11 regions analyzed in NGC 628. This ratio can be used to trace metallicity and ionization levels. Galactocentric distance is given in kiloparsecs.

For this galaxy we have data in  $H\alpha$ ,  $Br\gamma$ ,  $[OIII]$ ,  $[SII]$  and UV. After blurring the images, we identified 14 regions for analysis (see Table 5.10). For 11 of these

Table 5.10: Positions and Fluxes for NGC 628

Region	Position	$F_{\text{Br}\gamma}$	$F_{\text{UV}}$	$F_{2.14\mu\text{m}}$
1	-6.49, -84.89	0.224064E-09	0.101836E-13	0.714756E-09
2	44.39, 54.58	0.452434E-09	0.990297E-14	0.651994E-09
3	10.65, 162.39	0.912258E-10	0.710053E-14	. . .
4	-89.69, 11.46	0.706381E-09	0.151740E-13	0.196421E-08
5	0.38, -6.28	0.106545E-08	0.185181E-13	0.279448E-08
6	-16.93, 81.03	0.179764E-09	0.466330E-14	0.245430E-09
7	-92.66, -77.90	0.293216E-09	0.868040E-14	0.582719E-09
8	73.02, -113.64	. . .	0.870341E-14	0.253349E-09
9	-108.88, 102.67	0.312058E-09	0.987262E-14	0.652347E-09
10	71.35, -35.64	0.380098E-09	0.104617E-13	0.121268E-08
11	-24.05, -143.69	0.210344E-09	0.993128E-14	0.237110E-09
12	83.90, 108.91	0.101426E-09	0.404592E-14	0.476628E-10
13	131.40, -66.11	. . .	0.465505E-14	0.266743E-09
14	-196.11, 18.89	0.414734E-10	0.297076E-14	0.185932E-09

The columns are as follows: (1) the region number of each object, (2) the position offset from the center in arcseconds for each region (x, y), (3) the observed Br $\gamma$  flux in  $\text{erg sec}^{-1} \text{cm}^{-2}$ , (4) the observed UV flux in  $\text{erg sec}^{-1} \text{cm}^{-2}$ , (5) the observed i2.14  $\mu\text{m}$  flux in  $\text{erg sec}^{-1} \text{cm}^{-2}$ .

regions there were data for each of the bands: Br $\gamma$ , UV, 2.14  $\mu\text{m}$  continuum, 60  $\mu\text{m}$  and 100  $\mu\text{m}$ .

We analyzed these 11 regions using the  $\frac{[\text{SII}]}{\text{H}\alpha}$  as a tracer of supernova remnants (see Figure 5.23). Clearly, all the regions analyzed have a  $\frac{[\text{SII}]}{\text{H}\alpha}$  ratio which is indicative of a supernova remnant. (For a supernova remnant,  $\frac{[\text{SII}]}{\text{H}\alpha} \geq 0.45$ .) Such an effect is probably due to the large aperture sizes used. Regions with an  $\frac{[\text{SII}]}{\text{H}\alpha}$  ratio  $\leq 0.6$  probably contain a significant amount of diffuse ionized gas.

Looking at the [OIII] data for the same 11 regions (Figure 5.24) the  $\frac{[\text{OIII}]}{\text{H}\alpha}$  ratios are normal for typical H II regions ( $0.0 \leq \frac{[\text{OIII}]}{\text{H}\alpha} \leq 1.0$ ). As mentioned above, a high value for the  $\frac{[\text{OIII}]}{\text{H}\alpha}$  ratio may be indicative of a low ionization state or a high metallicity.

# Hydrogen Line Ratio vs. Distance for NGC 628

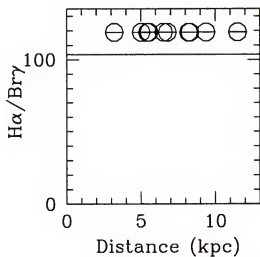


Figure 5.25: The  $\frac{H\alpha}{Br\gamma}$  ratio versus galactocentric distance in kiloparsecs.

# Star Formation Rates for NGC 628

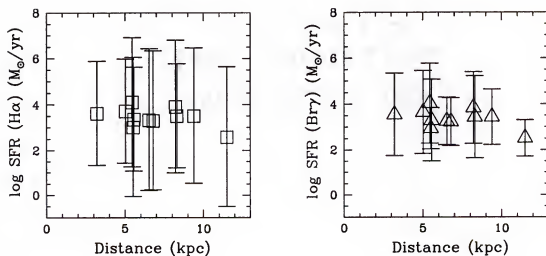


Figure 5.26: The star formation rates calculated from  $H\alpha$  and  $Br\gamma$ .



Table 5.11: Extinctions for NGC 628

Region	$A_V$	Error
1	14.798	0.0520
2	15.918	0.0467
3	13.651	0.0851
4	15.920	0.0823
5	16.271	0.0677
6	15.560	0.0329
7	15.419	0.0535
8	12.463	0.1580
9	14.881	0.1104
10	15.457	0.0436
11	14.768	0.1144
12	14.754	0.0361
13	15.171	0.0150
14	13.826	0.0543

The columns are as follows: (1) the region number, (2) the extinction,  $A_V$  in magnitudes and (3) the error in  $A_V$ . In each case, the  $A_V$  was calculated from the  $\text{Br}\gamma/\text{H}\alpha$  flux ratio.

We have plotted the  $\frac{\text{H}\alpha}{\text{Br}\gamma}$  ratio versus galactocentric distance in Figure 5.25. We can see that all 11 regions have ratios only slightly larger than expected. There does not seem to be a trend in the  $\frac{\text{H}\alpha}{\text{Br}\gamma}$  value with distance. In Table 5.11 we list the extinction derived for each region in NGC 628.

Also, we have calculated the star formation rates for both  $\text{H}\alpha$  and  $\text{Br}\gamma$ . In Figure 5.26, we show the star formation rate for  $\text{H}\alpha$  and  $\text{Br}\gamma$  plotted versus distance. The triangles represent the  $\text{Br}\gamma$  data and the squares represent the  $\text{H}\alpha$  data. As expected, the star formation rates calculated using  $\text{Br}\gamma$  are about the same as those calculated using  $\text{H}\alpha$ .

A comparison of the population ratios, using  $\text{Br}\gamma$  to represent the “very young” population, results in the conclusion that all 11 regions are heated by a “very young”

Table 5.12: Population Ratios for NGC 628

Region	VYP	YP	OP
1	0.157093E+34	0.180119E+15	0.399081E+11
2	0.890560E+36	0.519336E+16	0.193113E+12
3	0.707238E+31	0.139355E+14	. . .
4	0.617806E+36	0.351947E+16	0.256398E+12
5	0.276132E+37	0.629654E+16	0.312928E+12
6	0.223538E+36	0.317025E+16	0.163121E+12
7	0.541325E+35	0.116094E+16	0.944932E+11
8	. . .	0.622293E+12	0.218978E+10
9	0.459010E+34	0.309723E+15	0.567846E+11
10	0.626089E+35	0.115690E+16	0.153401E+12
11	0.198244E+34	0.250452E+15	0.197505E+11
12	0.444650E+34	0.488493E+15	0.194341E+11
13	. . .	0.493547E+16	0.501995E+12
14	0.716720E+32	0.914036E+14	0.815740E+11

The columns are as follows: (1) the region number, (2) the “very young” population ratio, ( $\frac{F_{\text{bol,ext}}(\text{Br}\gamma)}{F_{\text{FIR}}}$ ), (3) the “young” population ratio ( $\frac{F_{\text{bol,ext}}(\text{UV})}{F_{\text{FIR}}}$ ), (4) the “old” population ratio ( $\frac{F_{\text{bol,ext}}(2.14\mu\text{m})}{F_{\text{FIR}}}$ ). The population ratios are described in detail in Section 5.1.

population. Also, one can see from Table 5.12 that the “very young” population is dominant over the other populations by several orders of magnitude so that a small error in extinction or in our assumptions would not change the outcome of this analysis. If we use  $\text{H}\alpha$  instead of  $\text{Br}\gamma$  to represent the very young population, we arrive at the same conclusion as above: all 11 regions are heated by the very young population.

In Figure 5.4, we plot the log of the population ratios for each region versus  $\frac{F_{60\mu\text{m}}}{F_{100\mu\text{m}}}$ . The squares represent the  $\text{Br}\gamma$  data, the stars represent the UV data and the circles represent the continuum ( $2.14\mu\text{m}$ ) data. It is easy to see that the range in co-

Population Ratio vs. Color Temperature

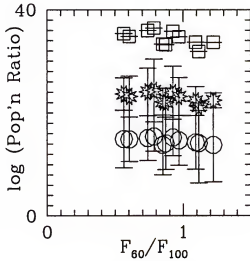


Figure 5.27: The log of the population ratios versus color temperature for NGC 628. Squares represent the “very young” population, stars represent the “young” population and circles represent the “old” population.

Color Temperature vs. Distance

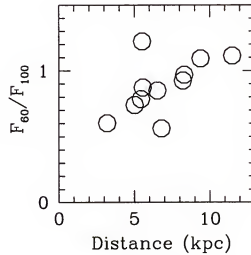


Figure 5.28: The  $\frac{F_{60\mu m}}{F_{100\mu m}}$  ratio plotted versus galactocentric distance (in kiloparsecs) for the 11 regions analyzed in NGC 628. Note the slightly increasing trend in the data with increasing galactocentric distance.

lor temperature is large; whereas, the dominant heating population is always the “very young” population by several orders of magnitude.

Further, we plot in Figure 5.28 the  $\frac{F_{60\mu m}}{F_{100\mu m}}$  ratio versus galactocentric distance to investigate the possibility of a trend of decreasing color temperature with increasing distance. For NGC 628, there may be a slight *increase* in color temperature with radial distance. The slope of a linear fit is  $0.052 \pm 0.001$ ; so while it is slightly positive, it is also nearly flat.

Lastly, we compare the luminosity functions for  $H\alpha$  and  $Br\gamma$ . We plot the luminosity functions for the 11 regions in Figure 5.29. It is easy to see that the  $Br\gamma$  data is not as deep as it should be. The  $Br\gamma$  data goes *only*  $\approx 10$  times deeper than the  $H\alpha$  data which is *not* sufficient to be sure that we have detected the same regions in  $Br\gamma$  as we did in  $H\alpha$ .

## Luminosity Function for NGC 628

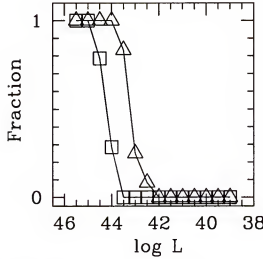


Figure 5.29: The luminosity functions for  $H\alpha$  and  $Br\gamma$ . The triangles represent the  $Br\gamma$  data and the squares represent the  $H\alpha$  data.

## 5.5 NGC 1068

For this galaxy, we have data for each of the four hydrogen recombination lines, as well as [OIII] and UV data. After blurring the images, we identified 25 regions for analysis (see Table 5.13). Of these, 9 regions had data in the  $Br\gamma$ , UV and  $2.14 \mu m$  continuum regimes.

Looking at the [OIII] data for the same 9 regions, (Figure 5.30), the  $\frac{[OIII]}{H\alpha}$  ratios are within the range, for the most part, for typical H II regions ( $0.0 \leq \frac{[OIII]}{H\alpha} \leq 3.0$ ).

Since we have data for  $H\beta$ ,  $H\alpha$ ,  $Pa\beta$  and  $Br\gamma$ , we have plotted the  $\frac{H\alpha}{H\beta}$ ,  $\frac{H\alpha}{Pa\beta}$ ,  $\frac{H\alpha}{Br\gamma}$  and  $\frac{Pa\beta}{Br\gamma}$  line ratios relative to one another, in Figure 5.31.

In Figure 5.32, we show the  $\frac{H\alpha}{H\beta}$ ,  $\frac{H\alpha}{Pa\beta}$ ,  $\frac{H\alpha}{Br\gamma}$  and  $\frac{Pa\beta}{Br\gamma}$  ratios plotted versus galactocentric distance. There seems to be a trend of increasing value for increasing distance for the  $\frac{H\alpha}{H\beta}$ ,  $\frac{Pa\beta}{Br\gamma}$  and  $\frac{H\alpha}{Br\gamma}$  ratios. However, the  $\frac{H\alpha}{Pa\beta}$  ratio shows a *decrease* in value with increasing galactocentric distance. An increase in the  $\frac{H\alpha}{Br\gamma}$  and  $\frac{Pa\beta}{Br\gamma}$  ratios with distance indicates an overestimate of extinction with increasing distance since increases in the

$\frac{[\text{OIII}]}{\text{H}\alpha}$  Plot for NGC 1068

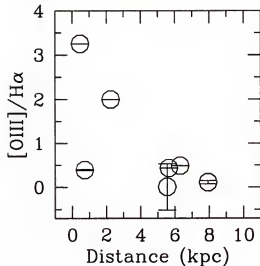


Figure 5.30: The ratio of  $[\text{OIII}]$  to  $\text{H}\alpha$  fluxes for each of the 9 regions analyzed in NGC 1068.

values of these ratios put them in the nonphysical regime. However, an increase in the  $\frac{\text{H}\alpha}{\text{H}\beta}$  ratio and a decrease in the  $\frac{\text{H}\alpha}{\text{Pa}\beta}$  ratio with distance would indicate the opposite trend: a *underestimate* in extinction with increasing distance, since the changes in the values of these ratios put them in the *physical* regime.

The  $\frac{\text{H}\alpha}{\text{H}\beta}$ ,  $\frac{\text{Pa}\beta}{\text{H}\beta}$  and  $\frac{\text{Br}\gamma}{\text{H}\beta}$  ratios were used to calculate an extinction for each region analyzed. The calculated extinctions are listed in Table 5.14.

Additionally, we have calculated the star formation rates for each of the four hydrogen emission lines. In Figure 5.33, we show the star formation rate for  $\text{H}\beta$ ,  $\text{H}\alpha$ ,  $\text{Pa}\beta$  and  $\text{Br}\gamma$  plotted versus galactocentric distance. In each band, one region, located on the nucleus of the galaxy, stands out. In our data, at the resolution of the PIXON enhanced IRAS HIRES images, we do resolve the active galactic nucleus (AGN). This aperture, with an anomalously high star formation rate in all bands is located on the AGN. It is interesting to note that the star formation rates for all regions calculated using  $\text{Pa}\beta$  are the lowest, while the star formation rates calculated using  $\text{H}\beta$  are the highest.

Table 5.13: Positions and Fluxes for NGC 1068

Region	Position	$F_{\text{Br}\gamma}$	$F_{\text{UV}}$	$F_{2.14\mu\text{m}}$
1	-4.01, -3.77	0.725513E-10	0.763459E-13	0.154495E-09
2	-123.23, -27.27	. . .	0.626587E-15	0.109322E-11
3	-58.80, 108.65	. . .	0.469350E-15	0.102074E-11
4	102.75, 80.53	0.253380E-13	0.849198E-15	0.548710E-12
5	87.30, -89.10	. . .	0.766999E-15	0.656867E-12
6	49.16, 17.02	0.310762E-12	0.657651E-15	0.101351E-11
7	51.07, -16.74	0.267158E-12	0.116713E-14	0.123606E-11
8	24.51, -51.39	0.564477E-12	0.160925E-14	0.182940E-11
9	6.27, -59.74	0.547866E-12	0.140447E-14	0.175276E-11
10	-123.17, -107.73	0.348119E-13	0.848516E-15	0.254616E-12
11	-86.43, -60.01	. . .	0.640749E-15	0.962778E-12
12	-141.15, -79.70	. . .	. . .	. . .
13	-30.34, -107.76	0.495570E-13	0.775416E-15	0.934799E-12
14	-17.88, -66.13	0.268381E-12	0.603851E-15	0.962811E-12
15	-25.67, 59.35	0.434225E-11	0.756771E-14	0.124126E-10
16	28.75, 110.30	0.120566E-13	0.144762E-15	0.234788E-12
17	26.28, -4.54	0.186411E-11	0.461717E-14	0.514510E-11
18	6.26, -28.83	0.398132E-11	0.728430E-14	0.965303E-11
19	22.08, 56.73	0.290284E-12	0.513427E-15	0.862298E-12
20	-45.71, 15.42	0.856136E-12	0.149084E-14	0.225372E-11
21	-69.16, -76.65	0.118131E-13	0.198127E-15	0.254273E-12
22	72.30, -24.11	0.235234E-12	0.971631E-15	0.108472E-11
23	45.25, 73.85	0.212828E-12	0.664152E-15	0.705491E-12
24	74.39, -94.69	0.177004E-13	0.623366E-15	0.531508E-12
25	-63.65, -165.09	. . .	. . .	. . .

The columns are as follows: (1) the region number of each object, (2) the position offset from the center in arcseconds for each region (x, y), (3) the Br $\gamma$  flux observed in  $\text{erg sec}^{-1} \text{cm}^{-2}$ , (4) the UV flux observed in  $\text{erg sec}^{-1} \text{cm}^{-2}$ , (5) the 2.14  $\mu\text{m}$  flux observed in  $\text{erg sec}^{-1} \text{cm}^{-2}$ .

## Hydrogen Line Ratios for NGC 1068

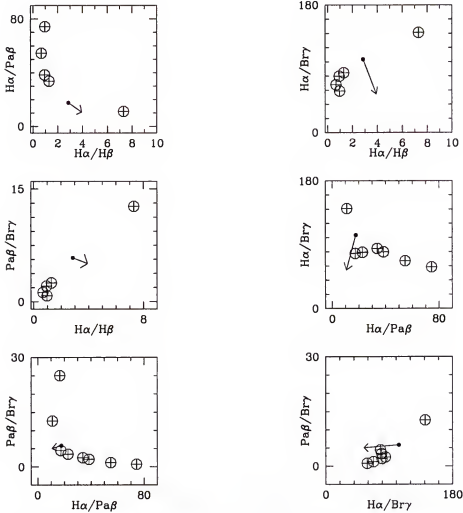


Figure 5.31: The  $\frac{H\alpha}{H\beta}$ ,  $\frac{H\alpha}{Pa\beta}$ ,  $\frac{H\alpha}{Bry}$ , and  $\frac{Pa\beta}{Bry}$  ratios used in determining the extinction. The filled circles indicate the theoretical expected values for the ratios, assuming case B recombination. The arrows indicate the effect of one magnitude of extinction on the ratios.

The energy balance analysis using the  $Bry$  flux to represent the “very young” population results in the conclusion that all 9 regions are heated predominantly by a “very young” population. In Table 5.15 we list the population ratios, as defined in Section 5.1, for each region in NGC 1068. If we use  $H\alpha$  instead of  $Bry$  to represent the “very young” population, we still find that all 9 regions are heated by the “very young” population.

In addition to the above energy balance analysis, we plot the log of the pop-

## Hydrogen Lines Ratios vs. Distance for NGC 1068

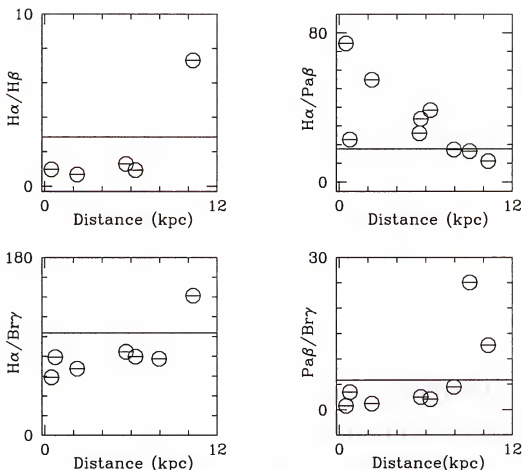


Figure 5.32: The  $\frac{H\alpha}{H\beta}$ ,  $\frac{H\alpha}{Pa\beta}$ ,  $\frac{H\alpha}{Br\gamma}$  and  $\frac{Pa\beta}{Br\gamma}$  ratios versus galactocentric distance in kiloparsecs.

ulation ratio versus the  $\frac{F_{60\ \mu m}}{F_{100\ \mu m}}$  ratio for each region in Figure 5.34. The squares represent the  $Br\gamma$  data, the stars represent the UV data, and the circles represent the  $2.14\ \mu m$  continuum data. Clearly, the range in color temperature is large; whereas, the dominant heating population is always the “very young” population by a factor of two to ten. For NGC 1068, color temperature cannot be used to determine a dominant heating population.

Further, we have plotted in Figure 5.35 the  $\frac{F_{60\ \mu m}}{F_{100\ \mu m}}$  versus galactocentric distance to investigate the possibility of a trend of cooling with increasing galactocentric distance. For NGC 1068, there is no trend in color temperature with radial distance



Table 5.14: Extinctions for NGC 1068

Region	$A_V$	Error	N
1	4.935	0.0006	3.0
2	2.736	0.0000	0.0
3	2.736	0.0000	0.0
4	2.736	0.0000	0.0
5	2.736	0.0000	0.0
6	4.620	0.0002	3.0
7	4.125	0.0002	3.0
8	4.757	0.0004	3.0
9	4.877	0.0004	3.0
10	1.020	0.0004	3.0
11	2.736	0.0000	2.0
12	2.736	0.0000	0.0
13	1.196	0.0002	3.0
14	4.466	0.0003	3.0
15	4.609	0.0004	3.0
16	1.299	0.0003	3.0
17	5.058	0.0003	3.0
18	5.225	0.0005	3.0
19	4.619	0.0003	3.0
20	5.177	0.0004	3.0
21	2.736	0.0000	0.0
22	2.736	0.0000	0.0
23	2.736	0.0000	0.0
24	2.736	0.0000	0.0
25	2.736	0.0000	0.0

The columns are as follows: (1) the region number, (2) the extinction,  $A_V$  in magnitudes, (3) the error in  $A_V$ , and (4) the the number of ratios used in the calculation. In cases where this number is zero, we have substituted an average value for  $A_V$ .

## Star Formation Rates for NGC 1068

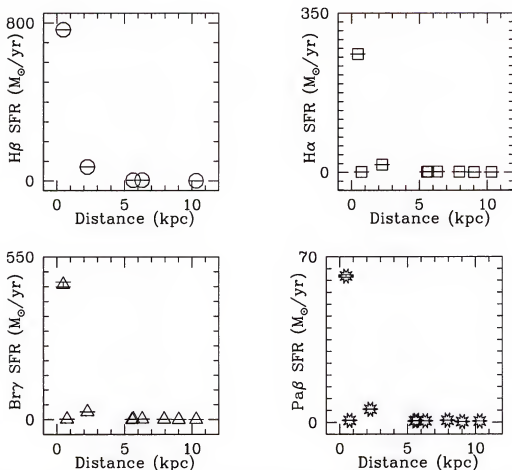


Figure 5.33: The star formation rates calculated from H $\beta$ , H $\alpha$ , Pa $\beta$  and Br $\gamma$ . The circles represent the H $\beta$  data, the squares represent the H $\alpha$  data, the stars represent the Pa $\beta$  data and the triangles represent the Br $\gamma$  data.

from the center. (The points with values for  $F_{60}/F_{100}$  of 5.0, are artificial, the actual ratios are absurdly high and probably erroneous.)

Lastly, we compare the luminosity functions for H $\beta$ , H $\alpha$ , Pa $\beta$  and Br $\gamma$ . In Figure 5.36, we plot the luminosity functions for the 9 regions. The circles represent the H $\beta$  data, the squares represent the H $\alpha$  data, the triangles represent the Br $\gamma$  data, and the stars represent the Pa $\beta$  data. Here, we can see that, the Br $\gamma$  and Pa $\beta$  data are  $\approx 10000$  times deeper than the H $\alpha$  and H $\beta$  data.

Table 5.15: Population Ratios for NGC 1068

Region	VYP	YP	OP
1	0.664658E+12	1318.82	23118.9
2	...	831.975	8952.93
3	...	...	...
4	...	...	...
5	...	...	...
6	...	...	...
7	...	...	...
8	...	...	...
9	...	...	...
10	...	...	...
11	...	830.782	7699.37
12	...	...	...
13	0.727365E+12	502.889	2531.32
14	0.131693E+14	13375.6	195944.
15	...	...	...
16	...	...	...
17	...	...	...
18	0.156801E+14	9574.04	96453.1
19	0.159045E+16	438940.	0.675859E+07
20	...	...	...
21	0.611319E+13	3252.35	25744.4
22	0.156802E+13	205.448	1414.64
23	0.409872E+13	405.726	2658.19
24	0.727612E+12	812.836	4274.64
25	...	...	...

The columns are as follows: (1) the region number, (2) the “very young” population ratio, ( $F_{\text{bol,ext}}(\text{Br}\gamma)/F_{\text{FIR}}$ ), (3) the “young” population ratio ( $F_{\text{bol,ext}}(\text{UV})/F_{\text{FIR}}$ ), (4) the “old” population ratio ( $F_{\text{bol,ext}}(2.14 \mu\text{m})/F_{\text{FIR}}$ )

Population Ratio vs. Color Temperature  
for NGC 1068

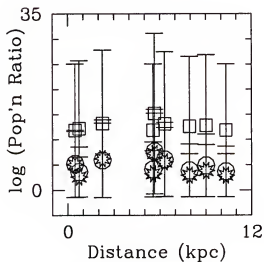


Figure 5.34: The population ratios versus  $\frac{F_{60 \mu m}}{F_{100 \mu m}}$  for each region in NGC 1068.

Color Temperature vs. Distance for  
NGC 1068

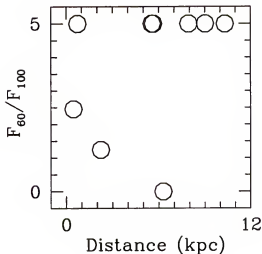


Figure 5.35: The  $\frac{F_{60 \mu m}}{F_{100 \mu m}}$  plotted versus galactocentric distance for each region in NGC 1068.

Luminosity Functions for NGC 1068

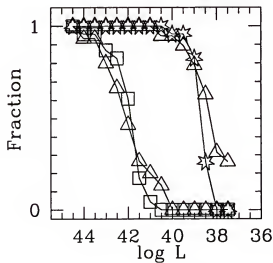


Figure 5.36: The luminosity functions of  $H\beta$ ,  $H\alpha$ ,  $Pa\beta$  and  $Br\gamma$  for the regions in NGC 1068.

## 5.6 NGC 4725

For this galaxy, we have data in  $H\alpha$ ,  $Pa\beta$  and  $Br\gamma$ . After blurring the images, we identified 26 regions for analysis (see Table 5.16). Of these, 21 had data in the  $Br\gamma$ , 2.14  $\mu\text{m}$  and FIR regimes.

Since we have data for three hydrogen emission lines, we have plotted the line ratios relative to one another to investigate the problem of larger and smaller than expected ratios. In Figure 5.37, we have a montage of several possible ratios plotted

Hydrogen Line Ratios for NGC 4725

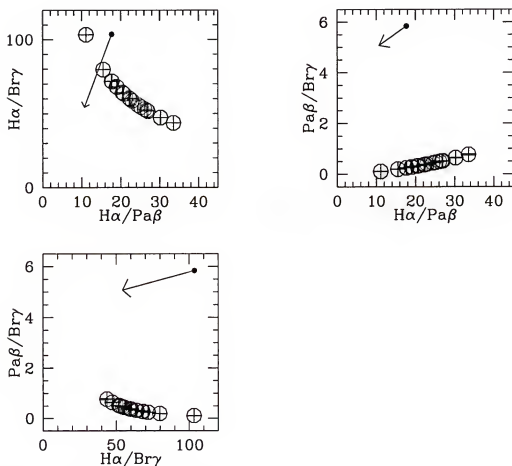


Figure 5.37: The  $\frac{H\alpha}{Br\gamma}$ ,  $\frac{H\alpha}{Pa\beta}$  and  $\frac{Pa\beta}{Br\gamma}$  line ratios. These were used in determining the extinction. In each image, the filled circle represents the theoretical expected values for the ratios, assuming case B recombination; and the arrow indicates the direction in which reddening would affect the ratio.

Table 5.16: Positions and Fluxes for NGC 4725

Region	Position	$F_{\text{Br}\gamma}$	$F_{2.14\mu\text{m}}$
1	82.96, -7.91	0.627662E-10	0.137777E-09
2	78.69, -65.98	0.214989E-09	0.483577E-09
3	-15.20, -94.61	0.251705E-09	0.271129E-09
4	-50.00, -28.64	0.320577E-10	0.142746E-09
5	-76.08, 71.06	0.226569E-09	0.782394E-09
6	-1.46, 1.07	0.356338E-08	0.111915E-07
7	55.57, -46.26	0.123659E-09	0.364151E-09
8	-2.75, 89.10	0.301875E-10	0.900876E-10
9	-46.90, 42.70	0.186090E-09	0.704390E-09
10	-58.92, -114.16	0.927512E-11	0.627923E-11
11	-82.42, -68.71	0.301420E-11	0.511417E-10
12	-53.58, -50.91	0.254017E-10	0.141313E-09
13	-112.06, -26.52	0.878465E-11	0.525516E-10
14	88.37, -40.77	0.557886E-10	0.136920E-09
15	107.98, -7.23	. . .	0.183205E-10
16	-113.81, 44.73	0.279655E-10	0.109767E-09
17	-108.71, 61.86	0.337395E-10	0.133670E-09
18	-130.39, 67.76	0.350253E-11	0.232998E-10
19	-98.92, 25.57	0.205790E-10	0.896236E-10
20	-103.99, 82.64	0.438049E-10	0.147287E-09
21	-129.61, 94.06	0.716416E-11	0.463771E-10
22	-60.74, 116.31	0.260027E-10	0.869324E-10
23	45.39, -112.49	0.366587E-09	0.153293E-08
24	-99.09, -133.45	. . .	. . .
25	-145.15, 36.14	0.940224E-11	. . .
26	15.56, 124.95	. . .	. . .

The columns are as follows: (1) the region number of each object, (2) the position offset from the center in arcseconds for each region (x, y), (3) the Br $\gamma$  flux observed in  $\text{erg sec}^{-1} \text{ cm}^{-2}$ , (4) the 2.14  $\mu\text{m}$  flux observed in  $\text{erg sec}^{-1} \text{ cm}^{-2}$ .

## Hydrogen Line Ratios vs. Distance for NGC 4725

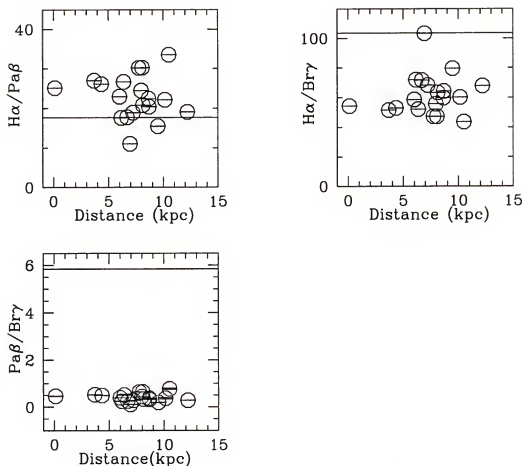


Figure 5.38: The  $\frac{H\alpha}{Br\gamma}$ ,  $\frac{H\alpha}{Pa\beta}$  and  $\frac{Pa\beta}{Br\gamma}$  line ratios versus galactocentric distance in kiloparsecs.

against one another. In each plot, the filled circle represents the theoretical expected values for the ratios, assuming case B recombination. The arrow indicates the effect of one magnitude of extinction on the ratio.

In Figure 5.38 we show the  $\frac{H\alpha}{Br\gamma}$ ,  $\frac{H\alpha}{Pa\beta}$  and  $\frac{Pa\beta}{Br\gamma}$  ratios plotted versus galactocentric distance. There is no trend with the values of the ratios with distance.

We have used the  $\frac{Pa\beta}{H\alpha}$  and  $\frac{Br\gamma}{H\alpha}$  ratios to calculate extinction using the method described in Section 5.1. The resulting extinctions for the regions in NGC 4725 are listed in Table 5.17.

In Figure 5.39, we show the log of the star formation rate for  $H\alpha$ ,  $Pa\beta$  and

Table 5.17: Extinctions for NGC 4725

Region	$A_V$	Error	N
1	20.580	0.0363	2.0
2	20.860	0.0451	2.0
3	21.024	0.0326	2.0
4	19.707	0.0422	2.0
5	20.199	0.0381	2.0
6	20.875	0.0282	2.0
7	20.949	0.0400	2.0
8	20.594	0.0474	2.0
9	20.609	0.0369	2.0
10	19.077	0.0098	1.0
11	19.077	0.0098	1.0
12	18.933	0.0533	2.0
13	16.536	0.0761	2.0
14	18.373	0.0317	2.0
15	19.077	0.0098	1.0
16	17.837	0.0425	2.0
17	18.343	0.0365	2.0
18	17.743	0.0811	2.0
19	18.529	0.0464	2.0
20	19.108	0.0362	2.0
21	16.820	0.0867	2.0
22	17.741	0.0573	2.0
23	18.400	0.0404	2.0
24	19.077	0.0098	0.0
25	19.077	0.0098	0.0
26	19.077	0.0098	0.0

The columns are as follows: (1) the region number, (2) the extinction,  $A_V$  in magnitudes, (3) the error in  $A_V$ , and (4) the number of ratios used in the calculation. In cases where this number is zero, we have substituted an average value for  $A_V$ .



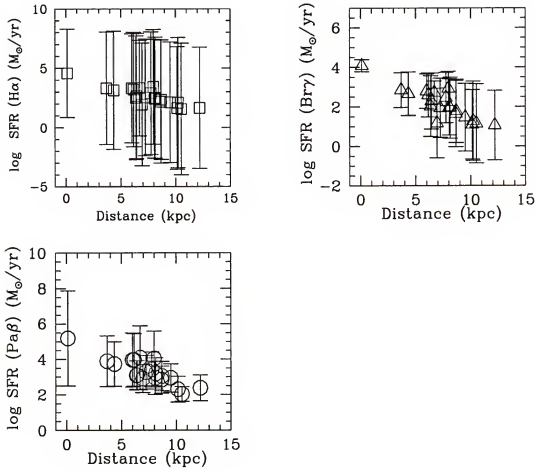


Figure 5.39: Star formation Rates for NGC 4725. In this figure we have plotted the star formation rates calculated from each of the three hydrogen recombination lines. It is easy to see that the star formation rates are similar, regardless of which line is used for the calculation.

$\text{Br}\gamma$  plotted versus galactocentric distance. As expected, all star formation rates calculated for this galaxy are, within the errors, similar.

Using the  $\text{Br}\gamma$  data to represent the “very young” population, we find that all 21 regions are heated predominantly by a “very young” population (see Table 5.18). If we use  $\text{H}\alpha$  instead of  $\text{Br}\gamma$  to represent the very young population, we still find that all 21 regions are heated by the very young population.

In Figure 5.40, we have plotted the log of the population ratios for each region versus the  $\frac{F_{60\ \mu\text{m}}}{F_{100\ \mu\text{m}}}$  ratio. The squares represent the  $\text{Br}\gamma$  data and the circles represent

Table 5.18: Population Ratios for NGC 4725

Region	VYP	OP
1	0.273859E+33	0.859725E+16
2	0.113762E+33	0.224543E+16
3	0.742131E+33	0.526518E+16
4	0.451456E+31	0.132967E+16
5	0.535052E+31	0.515627E+15
6	0.684892E+32	0.183750E+16
7	0.213548E+33	0.472308E+16
8	. . .	. . .
9	0.435309E+32	0.223918E+16
10	0.854865E+30	0.111724E+15
11	0.246889E+30	0.808662E+15
12	0.162684E+30	0.234390E+15
13	0.187131E+27	0.206837E+14
14	0.220832E+30	0.377956E+15
15	. . .	0.136731E+16
16	0.111500E+29	0.790493E+14
17	0.517038E+29	0.150759E+15
18	0.631255E+28	0.896553E+14
19	0.724712E+29	0.166906E+15
20	0.647705E+30	0.413951E+15
21	0.262746E+27	0.188636E+14
22	0.154847E+29	0.110950E+15
23	0.301098E+28	0.837425E+13
24	. . .	. . .
25	0.131809E+29	. . .
26	. . .	. . .

The columns are as follows: (1) the region number, (2) the “very young” population ratio,  $(\frac{F_{\text{bol,ext}}(\text{Br}\gamma)}{F_{\text{FIR}}})$ , (3) the “old” population ratio  $(\frac{F_{\text{bol,ext}}(2.14 \mu\text{m})}{F_{\text{FIR}}})$

Population Ratio vs. Color  
Temperature for NGC 4725

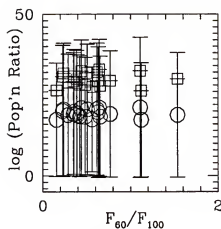


Figure 5.40: The log of the population ratio versus the  $\frac{F_{60\ \mu m}}{F_{100\ \mu m}}$  ratio for NGC 4725.

Color Temperature vs. Distance  
for NGC 4725

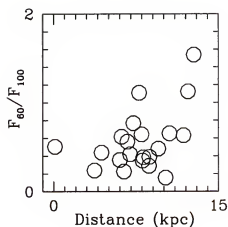


Figure 5.41: The  $\frac{F_{60\ \mu m}}{F_{100\ \mu m}}$  ratio plotted versus galactocentric distance for NGC 4725.

Luminosity Function for NGC 4725

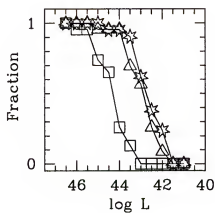


Figure 5.42: The luminosity functions for  $H\alpha$ ,  $Pa\beta$  and  $Br\gamma$  for NGC 4725.

the continuum ( $2.14\mu\text{m}$ ) data. Clearly, the range in color temperature is large; whereas, the dominant heating population is always the “very young” population by a factor of two to ten. For NGC 4725, color temperature cannot be used to determine a dominant heating population.

Further, in Figure 5.41, we have plotted the  $\frac{F_{60\mu\text{m}}}{F_{100\mu\text{m}}}$  ratio versus galactocentric distance. For NGC 4725, there seems to be an increase in color temperature with increasing radial distance from the center. The slope of a linear fit to these data is  $0.052 \pm 0.001$ . While this is a positive increase, it is also nearly flat.

Lastly, we compare the luminosity functions for the different hydrogen recombination line bands. We plot the luminosity functions for the 21 regions in Figure 5.42. The triangles represent the  $\text{H}\alpha$  data, the squares represent the  $\text{Br}\gamma$  data, and the stars represent the  $\text{Pa}\beta$  data. Here, we can see that, as expected, both the  $\text{Br}\gamma$  and  $\text{Pa}\beta$  data go  $\approx 100$  times deeper than the  $\text{H}\alpha$  data, indicating that we have gone as deep as needed to observe in  $\text{Br}\gamma$  and  $\text{Pa}\beta$  those objects detected in  $\text{H}\alpha$ .

### 5.7 NGC 3359

For this galaxy we have  $\text{H}\alpha$ ,  $\text{Br}\gamma$  and  $\text{Pa}\beta$  data. After blurring the images, we selected 16 regions to analyze (see Table 5.19). Of these regions, 5 contained data in the  $\text{Br}\gamma$ ,  $2.14\mu\text{m}$ , and FIR regimes and were consequently completely analyzed.

Since we have data for  $\text{H}\alpha$ ,  $\text{Pa}\beta$  and  $\text{Br}\gamma$ , we have plotted the  $\frac{\text{H}\alpha}{\text{Br}\gamma}$ ,  $\frac{\text{H}\alpha}{\text{Pa}\beta}$  and  $\frac{\text{Pa}\beta}{\text{Br}\gamma}$  ratios relative to one another in Figure 5.43. The  $\frac{\text{H}\alpha}{\text{Br}\gamma}$  and  $\frac{\text{H}\alpha}{\text{Pa}\beta}$  ratios indicate that we have underestimated the extinction.

In Figure 5.44, we show the  $\frac{\text{H}\alpha}{\text{Br}\gamma}$ ,  $\frac{\text{H}\alpha}{\text{Pa}\beta}$  and  $\frac{\text{Pa}\beta}{\text{Br}\gamma}$  ratios plotted versus galactocentric distance. There may be a trend of increasing value for increasing distance which would indicate that we are overestimating the extinction at large distances from the galaxy.

Additionally, we have calculated the star formation rates for  $\text{H}\alpha$ ,  $\text{Pa}\beta$  and  $\text{Br}\gamma$ . In Figure 5.45, these are plotted versus galactocentric distance. The squares

Table 5.19: Positions and Fluxes for NGC 3359

Region	Position	$F_{\text{Br}\gamma}$	$F_{2.14\mu\text{m}}$
1	3.20, -39.00	0.297905E-12	0.439815E-12
2	-41.90, -50.63	0.256004E-13	0.137150E-12
3	50.27, -70.16	. . .	0.392156E-13
4	20.34, -87.87	. . .	0.398745E-13
5	46.58, 4.67	. . .	0.515141E-13
6	38.70, 23.83	. . .	0.613359E-13
7	-56.28, 68.75	. . .	0.978230E-13
8	-26.69, 119.54	. . .	0.804587E-13
9	-9.26, 43.35	0.134456E-12	0.192204E-12
10	66.49, 71.43	. . .	0.877994E-13
11	-24.31, -92.65	. . .	0.965348E-13
12	-37.52, 16.74	0.648519E-13	0.146617E-12
13	-44.71, -22.63	0.755531E-14	0.580872E-13
14	82.95, 29.80	. . .	0.847961E-13
15	-39.69, -141.24	0.851473E-13	. . .
16	-102.29, -33.36	. . .	0.185967E-12

The columns are as follows: (1) the region number of each object, (2) the position offset from the center in arcseconds for each region (x, y), (3) the Br $\gamma$  flux observed in  $\text{erg sec}^{-1} \text{ cm}^{-2}$ , (4) the 2.14  $\mu\text{m}$  flux observed in  $\text{erg sec}^{-1} \text{ cm}^{-2}$ .

represent the H $\alpha$  data, the triangles represent the Br $\gamma$  data and the stars represent the Pa $\beta$  data. In each band, there seems to be a systematic decrease in star formation rate as distance from the center increases. Also, the star formation rates calculated using the Pa $\beta$  and Br $\gamma$  lines are comparable, while the star formation rates calculated using H $\alpha$  are *at least four times lower*.

The energy balance analysis using the Br $\gamma$  flux to represent the “very young” population results in the conclusion that all 5 regions are heated by a “very young” population. If we use H $\alpha$  instead of Br $\gamma$  to represent the “very young” population, we still find that all 5 regions are heated by the “very young” population.

## Hydrogen Line Ratios for NGC 3359

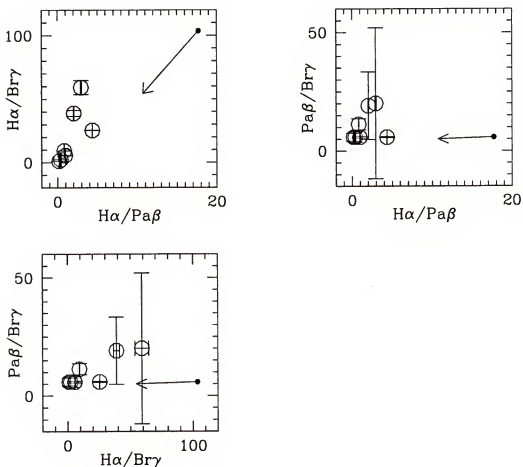


Figure 5.43: The  $\frac{H\alpha}{Br\gamma}$ ,  $\frac{H\alpha}{Pa\beta}$  and  $\frac{Pa\beta}{Br\gamma}$  line ratios used in determining the extinction. The filled circles indicate the theoretically predicted values for these ratios, assuming case B recombination. The arrows show the effect of one magnitude of extinction on each ratio.

In Figure 5.46, we plot the population ratios for each region versus the  $\frac{F_{60\ \mu m}}{F_{100\ \mu m}}$  ratio, which is representative of the color temperature. The circles represent the  $2.14\ \mu m$  continuum data and the squares represent the  $Br\gamma$  data. Clearly, there is no relationship between color temperature and dominant heating population. For NGC 3359, the color temperature can not be used to determine a dominant heating population. Such a lack of correlation between color temperature and dominant heating source implies that the dust which is emitting in the far infrared is comprised of a range of sizes of grains.

## Hydrogen Line Ratios vs. Distance for NGC 3359

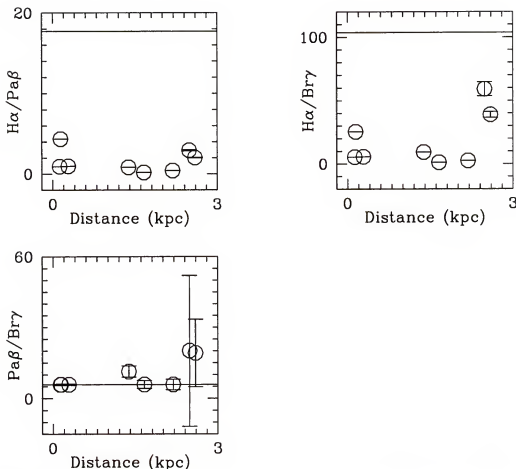


Figure 5.44: The  $\frac{H\alpha}{Br\gamma}$ ,  $\frac{H\alpha}{Pa\beta}$  and  $\frac{Pa\beta}{Br\gamma}$  ratios versus galactocentric distance in kiloparsecs.

We have plotted in Figure 5.47 the  $\frac{F_{60\ \mu m}}{F_{100\ \mu m}}$  ratio versus galactocentric distance to investigate the possibility of a trend of cooling with increasing distance. For NGC 3359, there may be an increase in color temperature with increasing radial distance from the center. There are too few points to perform a linear fit on these data.

Finally, we compare the luminosity functions in  $H\alpha$ ,  $Pa\beta$  and  $Br\gamma$  for the 5 regions analyzed. In Figure 5.48 we plot the luminosity functions for the 5 regions analyzed in NGC 3359. The squares represent the  $H\alpha$  data, the triangles represent the  $Br\gamma$  data, and the stars represent

Table 5.20: Extinctions for NGC 3359

Region	$A_V$	Error	N
1	8.925	0.0346	2.0
2	6.453	0.1127	2.0
3	6.339	0.1142	1.0
4	7.539	0.0187	0.0
5	8.291	0.0498	1.0
6	8.628	0.0429	1.0
7	7.539	0.0187	0.0
8	7.539	0.0187	0.0
9	8.121	0.0392	2.0
10	7.539	0.0187	0.0
11	7.539	0.0187	0.0
12	7.330	0.0634	2.0
13	6.228	0.2192	2.0
14	7.539	0.0187	0.0
15	7.539	0.0187	0.0
16	7.539	0.0187	0.0

The columns are as follows: (1) the region number, (2) the extinction,  $A_V$  in magnitudes, (3) the error in  $A_V$ , and (4) the the number of ratios used in the calculation. In cases where this number is zero, we have substituted an average value for  $A_V$ .



## Star Formation Rates for NGC 3359

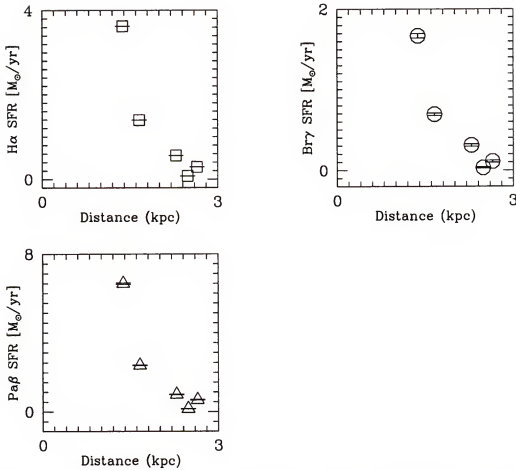


Figure 5.45: The star formation rates calculated from H $\alpha$ , Pa $\beta$  and Br $\gamma$ . The squares represent the H $\alpha$  data, the triangles represent the Br $\gamma$  data and the stars represent the Pa $\beta$  data.

the Pa $\beta$  data. We note that the Br $\gamma$  data *is not* the necessary 100 times deeper than the H $\alpha$  data. Nor is the Pa $\beta$  data 18 times deeper than the H $\alpha$  data. It is likely that our data for this galaxy are poor. Interestingly, however, we did not find anything unusual in our analysis of this galaxy, despite the poor data quality.

Table 5.21: Population Ratios for NGC 3359

Region	VYP	YP	OP
1	0.820922E+25	657713.	
2	0.385179E+19	424649.	
3	. . .	0.155787E+07	
5	. . .	0.238353E+07	
6	. . .	0.214658E+07	
7	. . .	557666.	
8	. . .	0.170775E+07	
9	0.851433E+23	426848.	
10	. . .	0.338211E+07	
11	. . .	552494.	
12	0.346508E+21	168242.	
13	0.366126E+18	186768.	
14	. . .	. . .	
15	0.187803E+23	. . .	
16	. . .	. . .	

The columns are as follows: (1) the region number, (2) the “very young” population ratio, ( $F_{\text{bol,ext}}(\text{Br}\gamma)/F_{\text{FIR}}$ ), (3) the “old” population ratio ( $F_{\text{bol,ext}}(2.14\ \mu\text{m})/F_{\text{FIR}}$ )

Population Ratio vs. Color Temperature  
for NGC 3359

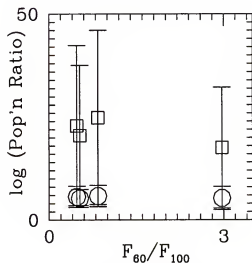


Figure 5.46: The population ratios versus color temperature for NGC 3359.

Color Temperature vs. Distance for  
NGC 3359

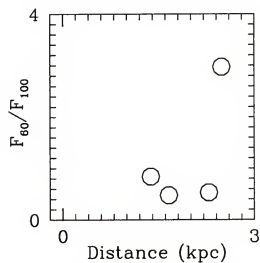


Figure 5.47: The color temperature plotted versus distance for NGC 3359.

Luminosity Functions for NGC 3359

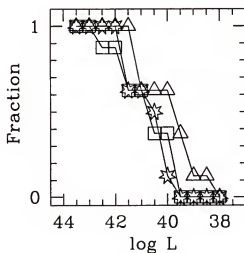


Figure 5.48: The luminosity functions for  $H\alpha$ ,  $Pa\beta$  and  $Br\gamma$ .

Table 5.22: Positions and Fluxes for NGC 4535

Region	Position	$F_{\text{Br}\gamma}$	$F_{2.14\mu\text{m}}$
1	54.79, 26.82	0.803220E-11	0.165904E-09
2	26.59, 51.29	0.842257E-11	0.178168E-09
3	6.94, 86.26	. . .	0.172622E-09
4	-0.05, 124.17	. . .	0.114141E-09
5	-1.50, -0.56	0.311298E-09	0.154213E-08
6	-41.63, 23.71	0.301706E-10	0.361110E-09
7	-45.22, -45.37	0.307590E-10	0.579072E-09
8	40.39, -16.64	0.120866E-09	0.800072E-09
9	57.15, 51.90	0.108860E-10	0.334074E-09
10	21.90, -69.00	0.857527E-10	0.578772E-09

The columns are as follows: (1) the region number of each object, (2) the position offset from the center in arcseconds for each region (x, y), (3) the Br $\gamma$  flux observed in  $\text{erg sec}^{-1} \text{cm}^{-2}$ , (4) the 2.14  $\mu\text{m}$  flux observed in  $\text{erg sec}^{-1} \text{cm}^{-2}$ .

### 5.8 NGC 4535

For this galaxy, we have data in H $\alpha$  and Br $\gamma$ . After blurring the images, we identified 10 regions for analysis (see Table 5.22). Of these, 8 regions had data in the Br $\gamma$ , 2.14  $\mu\text{m}$  continuum, 60  $\mu\text{m}$  and 100  $\mu\text{m}$  bands. Therefore, we analyze only these 8 regions.

In Figure 5.49, we have plotted the  $\frac{\text{H}\alpha}{\text{Br}\gamma}$  ratio versus galactocentric distance to demonstrate that there is no trend between the ratio and distance. Using the  $\frac{\text{Br}\gamma}{\text{H}\alpha}$  ratio, we have calculated the extinction for each of the regions (see Table 5.23).

Additionally, we have calculated the star formation rates using H $\alpha$  and Br $\gamma$ . In Figure 5.50, we show the log of the star formation rate for these lines plotted versus galactocentric distance. In each band, there seems to be a systematic decrease in star formation rate with increasing distance from the center. Also, the Br $\gamma$  star formation rate is similar to the H $\alpha$  star formation rate.

## Hydrogen Line Ratio vs. Distance for NGC 4535

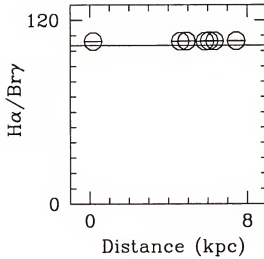


Figure 5.49: The  $\frac{H\alpha}{Br\gamma}$  ratio versus galactocentric distance in kiloparsecs.

The energy balance using the  $Br\gamma$  flux to represent the “very young” population leads to the conclusion that all 8 regions are heated by a “very young” population. In Table 5.24, we list the population ratios (as defined in Section 5.1) for each region in NGC 4535. If we use  $H\alpha$  instead of  $Br\gamma$  to represent the “very young” population, we still find that all 8 regions are heated by the “very young” population.

In addition, in Figure 5.51, we plot the log of the population ratios for each region versus the  $\frac{F_{60\ \mu m}}{F_{100\ \mu m}}$  ratio. The squares represent the  $Br\gamma$  data and the circles represent the  $2.14\ \mu m$  continuum data. Clearly, the range in color temperature is large; whereas, the dominant heating population is always the “very young” population by several orders of magnitude. For NGC 4535, color temperature cannot be used to determine a dominant heating population.

Further, we have plotted in Figure 5.52 the  $\frac{F_{60\ \mu m}}{F_{100\ \mu m}}$  ratio versus galactocentric distance. For NGC 4535, there may be a slight decrease in color temperature with increasing radial distance from the center. The slope of a linear fit to these data is  $-0.042 \pm 0.002$ . So, while there is a negative trend, it is also nearly flat.

Table 5.23: Extinctions for NGC 4535

Region	$A_V$	Error
1	16.128	0.0542
2	16.003	0.0519
3	16.752*	0.0112
4	16.752*	0.0112
5	18.323	0.0206
6	17.050	0.0305
7	15.245	0.0349
8	18.172	0.0250
9	15.054	0.0765
10	18.040	0.0278

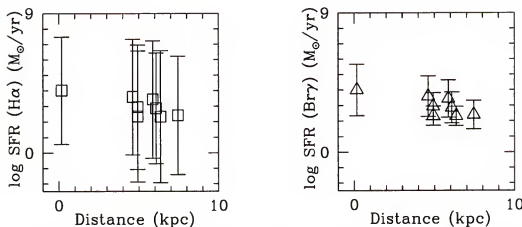
The columns are as follows: (1) the region number, (2) the extinction,  $A_V$  in magnitudes, (3) the error in  $A_V$ . The asterisks indicate where we could not calculate  $A_V$  and have substituted an average value for  $A_V$ .

Table 5.24: Population Ratios for NGC 4535

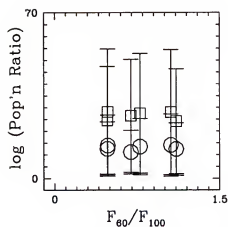
Region	VYP	OP
1	0.161526E+25	0.620214E+12
2	0.425466E+25	0.853032E+12
3	. . .	0.260456E+13
4	. . .	0.604409E+13
5	0.113335E+29	0.203851E+14
6	0.680231E+29	0.598837E+14
7	0.893204E+28	0.139307E+13
8	0.366015E+28	0.442245E+13
9	0.334820E+27	0.419738E+11
10	0.160670E+29	0.133719E+14

The columns are as follows: (1) the region number, (2) the “very young” population ratio,  $(F_{\text{bol,ext}}(\text{Br}\gamma)/F_{\text{FIR}})$ , (3) the “old” population ratio  $(F_{\text{bol,ext}}(2.14 \mu\text{m})/F_{\text{FIR}})$

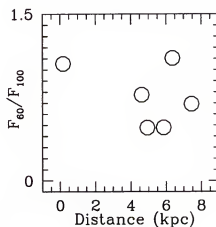
## Star Formation Rates for NGC 4535

Figure 5.50: The star formation rates calculated from the H $\alpha$  and Br $\gamma$  data.

## Population Ratio vs. Color Temperature for NGC 4535

Figure 5.51: The  $\log$  of the population ratios versus  $\frac{F_{60 \mu\text{m}}}{F_{100 \mu\text{m}}}$  for NGC 4535.

## Color Temperature vs. Distance for NGC 4535

Figure 5.52: The  $\frac{F_{60 \mu\text{m}}}{F_{100 \mu\text{m}}}$  ratio plotted versus galactocentric distance for NGC 4535.

## Luminosity Function for NGC 4535

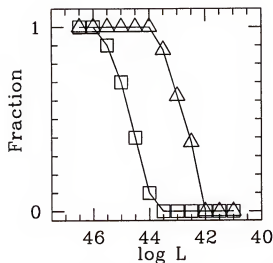


Figure 5.53: The luminosity functions of  $H\alpha$  and  $Br\gamma$  for the regions in NGC 4535.

Lastly, in Figure 5.53 we plot the luminosity functions in  $H\alpha$  and  $Br\gamma$  for the 8 regions in NGC 4535. The squares represent the  $H\alpha$  data and the triangles represent the  $Br\gamma$  data. As expected, the data in  $Br\gamma$  is  $\approx 100$  times deeper than the data in  $H\alpha$ .



## CHAPTER 6 DISCUSSION

In this chapter, we discuss the results presented in the previous chapter and their relevance in the general field of extragalactic astronomy and particularly in the understanding of far infrared radiation. Most importantly, we discuss the results in the context of previous works and future prospects.

### 6.1 Comparison of Results With Previous Works

As mentioned in the introduction, much work has been done on this topic. The main differences between this work and previous works are as follows

- we used Br $\gamma$  rather than H $\alpha$  as a star formation indicator
- we evaluated the extinction for each region using several recombination lines of hydrogen
- we used different extinction laws to evaluate different stellar populations
- we used very recent stellar models which include an empirical analysis of stellar spectra for early type stars in the ultraviolet regime
- we enhanced the resolution of the *IRAS* HIRES images using PIXON image reconstruction

Originally, it was thought that far infrared radiation was directly related to star formation (Rieke & Lebofsky 1979, Telesco & Harper 1980, Stein & Soifer 1983). It is only since these first claims, that the source of far infrared radiation must be related to star formation, that others have done studies and tried to prove otherwise.

Many of these more recent tests were done using a global approach, where the global flux of the galaxy is examined in several bands each of which indicates a different heating source. With the advent of HIRES image processing and other techniques developed mainly to deal with deconvolution of Hubble Space Telescope data, more recent studies have been able to examine this problem using spatial data, evaluating the energy budget of individual regions within a galaxy.

#### 6.1.1 Agreement

Our results agree with the following studies. The works described below share some overlap with our sample. The overlap is clearly identified in the summary of each paper.

The first study which included an analysis of the source of far infrared radiation was that of Rieke & Lebofsky (1979). In their paper, they suggest that the far infrared radiation observed in spiral galaxies originates in or near star forming regions. The good correlation observed in the few galaxies for which there exist data (including NGC 6946 and NGC 1068) between the mid-infrared and far infrared, the nonthermal radio continuum and far infrared and the near infrared hydrogen line fluxes and far infrared implies that the far infrared radiation is associated with star formation.

A study by Telesco & Harper (1980) indicates that the energy observed in the far infrared is *inconsistent* with an "old" population, and *consistent* with a "very young" population heating the dust which produces the far infrared. Through a comparison of radio data with far infrared data for their sample (including NGC 6946 and NGC 1068), these authors found that the implied Lyman continuum emission and the infrared luminosity are equivalent to that which would be generated by a large number of very young stars.

Sanders, et al. (1986) studied the molecular gas content in high luminosity *IRAS* galaxies. They find that the correlation between molecular gas mass and far

infrared luminosity is very good. From this, and the fact that all of the galaxies in their sample (which includes NGC 1068) have emission line spectra, they conclude that the high infrared luminosity originates from star formation.

Solomon & Sage (1988) studied the  $L_{FIR}/L_{CO}$  ratio. For their sample of galaxies which are not interacting strongly (which includes NGC 6946), they conclude that the far infrared radiation observed can be understood as a result of star formation at a rate similar to that of galactic molecular clouds.

Bicay, Helou & Condon (1989) examined the infrared to radio ratio in NGC 6946. They note the tight coupling between the origins of the dust-heating radiation and the radio-emitting cosmic ray electrons. Further, they state that this coupling is strongly suggested by the remarkable constancy of the global infrared to radio ratio in galaxies displaying various levels of star formation activity. This implies that the radio and infrared disks reflect the same source distribution, implying that the two sources are the same: star formation.

Young, et al. (1989) studied a sample of 182 galaxies (in which NGC 2403, NGC 628, NGC 4725, NGC 1068 and NGC 4535 are included) and found a good correlation between the far infrared luminosity and  $H\alpha$  luminosity

$$L_{IR} \propto L(H\alpha)^{1.0 \pm 0.1} \quad (6.1)$$

This implies that the far infrared luminosity is a measure of the star formation rate for these galaxies.

Chi & Wolfendale (1990) find from an analysis of their sample (which includes NGC 2403, NGC 300 and NGC 628) a tight correlation between radio and far infrared with a nonunity slope. They conclude that this can be explained by a model which attributes the sum of the far infrared radiation and the cosmic ray radiation to the star formation rate. This implies that the far infrared radiation is dominated by heating from a "very young" population.

Bicay & Helou (1990) perform an analysis of the radio to far infrared correlation as a follow-up to their previous paper (Bicay & Helou, 1989). They note once again, the tight coupling between the radio and far infrared sources. This time, they performed a scale length analysis of the galaxies in their sample (which includes NGC 6946) and find that the scale lengths of the radio disks are comparable to the scale lengths of the far infrared disks. This evidence, in addition to the abovementioned coupling, implies that far infrared radiation is caused by dust heated by a "very young" population of stars.

Telesco, Dressel, & Wolstencroft (1993) studied a sample of galaxies (which include NGC 6946 and NGC 1068) in the mid-infrared regime. They find that the mid-infrared radiation is directly related to the far infrared radiation and tightly correlated with Br $\gamma$  radiation, implying a connection between far infrared radiation and star formation.

Devereux & Young (1993) analyzed NGC 6946. In this study, they used H $\alpha$  as a star formation indicator and did a spatial analysis of the heating source. Their finding was that all 137 regions analyzed were dominated by very young stellar population heating due to the similarities in the radial distributions of the far infrared and H $\alpha$  luminosities, and the correlation between the far infrared luminosity measured and that expected from the stars needed to ionize the gas. The biggest shortcoming of this work is that the apertures used are more than two times smaller in radius than the point spread function of the far infrared image. This means that in their analysis, many regions are missing far infrared flux.

In an analysis of the far infrared - radio correlation seen in galaxies, Xu, et al (1994) find that their sample of 114 late-type spiral galaxies (in which NGC 2403, NGC 4725, NGC 3359 and NGC 4535 are included) show that the correlation between radio and far infrared radiation is independent of old population, implying a relationship between the far infrared and star formation.

Lu, et al. (1996) present results from the as yet unreleased ISOPHOT data for NGC 6946. In a comparison of  $60\mu\text{m}$  and radio fluxes, these authors find that their data can be fit to either a model which is dominated by “very young” population heating, or one which is similar to that proposed by Bica & Helou (1990). Both models imply a strong relationship between radio and far infrared which implies that far infrared radiation is related to star formation.

Finally, Goldader, et al. (1997) looked at a spectrum of NGC 1068 in which includes the Br $\gamma$  emission line. From their data, they find that simple starburst models are able to explain the observed Br $\gamma$  and far infrared luminosities, implying that the far infrared radiation is dominated by heating by the “very young” population.

#### 6.1.2 Contradiction

The following works draw conclusions contradictory to ours. Each of these papers contains a subset of our sample which is clearly indicated in each summary. Of course, others have come to contradictory conclusions, but this subset of papers includes analyses of some of the galaxies in our sample.

Bothun & Rogers (1992) conclude from their analysis of 28 galaxies (which includes NGC 2403, NGC 6946, NGC 300 and NGC 628) that far infrared radiation is dominated by an “old” population. This conclusion is reached from a comparison of  $B$  band scale lengths to far infrared scale lengths.

In a study which focuses mainly on the radio continuum radiation as compared to the far infrared radiation, Mayya & Rengarajan (1997a) find that the far infrared radiation is dominated by “very young” population stars in the inner parts of the galaxy; whereas, in the outer parts, the far infrared radiation seems to be coming from a general interstellar radiation field. This is evidenced by the fact that the contribution to the total  $60\mu\text{m}$  emission from big grains decreases dramatically away from the center of the galaxies in their sample (which includes NGC 2403, NGC 6946, NGC 628 and NGC 4535). According to their models, this implies that the far

infrared radiation is *not* as closely tied to star formation, but rather to a general interstellar radiation field.

Mayya & Rengarajan (1997b) did a study of the source of far infrared radiation in spiral galaxies where they evaluated possible heating sources by examining the observed dust temperatures. They find that for their sample (which includes NGC 2403, NGC 6946, NGC 628 and NGC 4535), the dust temperature gradient can be reproduced well using a dust mixture described by D'esert et al. (1990) with an enhancement of very small grain content. That is, the general flux levels *do not* indicate a significant contribution from the very young population (recent star formation). However, they do find that in order to reproduce the observed dust temperature distribution at all radii, it is necessary to use more elaborate models which incorporate heating by ionizing photons in addition to a general interstellar radiation field.

## 6.2 Summary of Our Results

For NGC 2403, we studied 13 different regions and found that all 13 regions are dominated by heating by the “very young” population. This result is inconsistent with the Mayya & Rengarajan (1997b) study where they find that the general flux levels do not indicate a significant contribution from the “very young” population. However, our findings agree with the result that there is no significant decrease in dust temperature (which is directly proportional to the  $\frac{F_{60 \mu m}}{F_{100 \mu m}}$  ratio).

In NGC 6946, we found that all 13 regions were heated by a “very young” population. These results do not agree with the Mayya & Rengarajan (1997a) and the Bothun & Rogers (1992) studies. Additionally, we did not find an obvious decrease in the  $\frac{F_{60 \mu m}}{F_{100 \mu m}}$  ratio (dust temperature), in contradiction with the findings of Mayya & Rengarajan (1997b).

For NGC 300, we found that all 26 regions we evaluated were heated by a “very young” population. There are no studies which contradict our results.

In NGC 628, we find that all 11 regions in NGC 628 are heated by a “very young” population. Our results do not agree with the Mayya & Rengarajan (1997a) and the Bothun & Rogers (1992) studies. Further, we did not find an obvious decrease in the  $\frac{F_{60\ \mu m}}{F_{100\ \mu m}}$  ratio (dust temperature), in contradiction with the findings of Mayya & Rengarajan (1997b).

In NGC 1068, we find all 9 regions are heated by a “very young” population. Our results for this galaxy agree with all previous studies.

For NGC 4725, we find all 21 regions are heated by a “very young” population. There are no studies which contradict our results.

In NGC 3359, we find all 8 regions are heated by a “very young” population when we use Br $\gamma$  as a star formation indicator. Our results, for this galaxy agree with the previous study.

For NGC 4535, we found that all 8 regions studied are dominated by “very young” population heating. This result is inconsistent with the Mayya & Rengarajan (1997b) study where they find that the general flux levels do not indicate a significant contribution from the “very young” population. However, our findings agree with those of Mayya & Rengarajan (1997b), in that we do not see a trend of decrease in dust temperature (which is directly proportional to the  $\frac{F_{60\ \mu m}}{F_{100\ \mu m}}$  ratio).

Our analysis was for the case where we evaluated the extinction in each region and used Br $\gamma$  to represent the “very young” population. If we use H $\alpha$ , our result do not change. However, if we use a global extinction law, like the one described by Israel & Kennicutt (1980), our results change. In this case, if we use Br $\gamma$  to trace the “very young” population, we get the same results as before; however, if we use H $\alpha$  to trace the “very young” population, we find that our results vary from galaxy to galaxy (see Table 6.1).

Table 6.1: Energy Balance Analysis Using Global Extinction Law and H $\alpha$

Galaxy	N	VYP(gH $\alpha$ )	OP(gH $\alpha$ )
NGC 2403	13	10	3
NGC 6946	13	0	13
NGC 300	26	26	0
NGC 628	11	0	11
NGC 1068	9	5	4
NGC 4725	21	0	21
NGC 3359	5	0	5
NGC 4535	8	0	8

The columns are as follows: (1) the galaxy name, (2) the number of regions analyzed, (3) the “very young” population ratio,  $\frac{F_{\text{bol,ext}}(\text{H}\alpha)}{F_{\text{FIR}}}$ ), where we have used  $A_V=1.1$  for all regions analyzed and (4) the “old” population ratio  $\frac{F_{\text{bol,ext}}(2.14 \mu\text{m})}{F_{\text{FIR}}}$ ), where we have used  $A_V=1.1$  for all regions analyzed.

The reason for this variation is due to the longer wavelength of Br $\gamma$ . Underestimating the extinction, even by several magnitudes, does not change the interpretation of the Br $\gamma$  data very much. The longer wavelength of Br $\gamma$  makes it *much* less sensitive to errors in extinction estimates. Therefore, if it is not possible to estimate extinction and a global extinction law is necessary, using Br $\gamma$ , rather than H $\alpha$  to trace the “very young” population, would result in a correct analysis.

In addition to the main analysis of heating population, we used the other data in our study to investigate other interesting trends. In Tables 6.2 and 6.3, we present a summary of the results of these studies.

In Table 6.2, columns (2) and (3), we present the results of the  $\frac{[\text{SII}]}{\text{H}\alpha}$  and  $\frac{[\text{OIII}]}{\text{H}\alpha}$  trends. We notice that for the three galaxies for which we have [SII] data, only one displays unusually high values for this ratio, namely, NGC 628. The high values may be due to several reasons. First, and most likely, the large apertures may include a considerable amount of diffuse ionized medium which can raise the  $\frac{[\text{SII}]}{\text{H}\alpha}$  ratio to  $\approx 0.6$ . This does not completely explain the data, however. There are five galaxies for which



Table 6.2: Summary Table Part 1

Object	$\frac{[\text{SII}]}{\text{H}\alpha}$	$\frac{[\text{OIII}]}{\text{H}\alpha}$	$\frac{\text{H}\alpha}{\text{H}\beta}$	$\frac{\text{H}\alpha}{\text{Pa}\beta}$	$\frac{\text{H}\alpha}{\text{Br}\gamma}$	$\frac{\text{Pa}\beta}{\text{Br}\gamma}$
NGC 2403	lo, ↓	OK, ↓	mostly lo, ↑	mostly lo, ↓	hi, ↑	<b>hi, ↑</b>
NGC 6946	. . .	hi, ↑	lo, ↓	. . .	hi, ↓	. . .
NGC 300	lo, ↓	<b>lo, ↑</b>	. . .	. . .	OK, ↓	. . .
NGC 628*	<b>hi, ↓</b>	OK, ↓	. . .	. . .	hi, ↑	. . .
NGC 1068	. . .	hi, ↓	mostly lo, ↑	mostly hi, ↓	mostly lo, ↑	mostly lo, ↑
NGC 4725	. . .	. . .	. . .	hi, ↑	<b>lo, ↑</b>	lo, ↓
NGC 3359*	. . .	. . .	. . .	lo, ↑	<b>lo, ↓</b>	OK, ↑
NGC 4535	. . .	. . .	. . .	. . .	OK, ↑	. . .

The columns are as follows: (1) the object name, (2) the  $\frac{[\text{SII}]}{\text{H}\alpha}$  ratio, (3) the  $\frac{[\text{OIII}]}{\text{H}\alpha}$  ratio, (4) the  $\frac{\text{H}\alpha}{\text{H}\beta}$  ratio, (5) the  $\frac{\text{H}\alpha}{\text{Pa}\beta}$  ratio, (6) the  $\frac{\text{H}\alpha}{\text{Br}\gamma}$  ratio and (7) the  $\frac{\text{Pa}\beta}{\text{Br}\gamma}$  ratio. Arrows indicate the direction of the trend with distance, words indicate the value calculated with respect to the value expected. Trends which are different from the majority in this sample are highlighted.

Table 6.3: Summary Table Part 2

Object	N	SFR(H $\beta$ )	SFR(H $\alpha$ )	SFR(Pa $\beta$ )	SFR(Br $\gamma$ )	Color Temp
NGC 2403	13	hi-est, ↓	OK, ↓	lo-est, ↓	OK, ↓	hi, ↓
NGC 6946	13	hi-est, ↓	OK, ↓	. . .	lo-est, ↓	wide, ↑
NGC 300	26	. . .	OK, ↓	. . .	OK, ↓	wide, ↓
NGC 628*	11	. . .	hi, ↓	. . .	hi, ↓	hi, ↑
NGC 1068	9	hi-est, ↓	hi, ↓	lo-est, ↓	hi, ↓	too high, ↑
NGC 4725	21	. . .	hi, ↓	hi-est, ↓	lo-est, ↓	wide, ↑
NGC 3359*	5	. . .	lo-est, ↓	hi-est, ↓	hi, ↓	too high, ↑
NGC 4535	8	. . .	hi-est, ↓	. . .	lo-est, ↓	OK, ↓

The columns are as follows: (1) the object name, (2) the number of regions analyzed, (3) the H $\beta$  star formation rate trend with galactocentric distance, (4) the H $\alpha$  star formation rate trend with distance, (5) the Pa $\beta$  star formation rate trend with distance, (6) the Br $\gamma$  star formation rate trend with distance and (7) the color temperature trend with distance. Arrows indicate the direction of the trend with distance, words indicate the value calculated with respect to the value expected. Trends which are different from the majority in this sample are highlighted.

we have  $\frac{[\text{OIII}]}{\text{H}\alpha}$  data. Of these, one has unusually low values for the  $\frac{[\text{OIII}]}{\text{H}\alpha}$  ratio and two show increasing, rather than decreasing trends. The low ratio may indicate a high ionization state of the gas or a low metallicity. Without other diagnostic lines, it is impossible to tell which is the reason for the trend in values. This ratio, however, usually *decreases* with increasing radius, since it is more sensitive to metallicity than ionization state. The observed *increase* in NGC 6946 and NGC 300 is probably due to a decreasing ionization state, and not an increasing metallicity.

Columns (4) through (7) of Table 6.2 show trends of the values of the hydrogen recombination ratios and trends of the values with galactocentric distance. A *low* value for the  $\frac{\text{H}\alpha}{\text{H}\beta}$  ratio and a *high* value for the  $\frac{\text{H}\alpha}{\text{Pa}\beta}$ ,  $\frac{\text{H}\alpha}{\text{Br}\gamma}$  and  $\frac{\text{Pa}\beta}{\text{Br}\gamma}$  ratios is indicative of an overestimate of extinction.

For NGC 2403, the  $\frac{\text{H}\alpha}{\text{H}\beta}$ ,  $\frac{\text{H}\alpha}{\text{Br}\gamma}$  and  $\frac{\text{Pa}\beta}{\text{Br}\gamma}$  ratios all indicate that we have overestimated the extinction throughout the galaxy. Only the  $\frac{\text{H}\alpha}{\text{Pa}\beta}$  ratio indicates the opposite trend: that we have *underestimated* the extinction throughout the galaxy. Both the  $\frac{\text{H}\alpha}{\text{H}\beta}$  and  $\frac{\text{H}\alpha}{\text{Br}\gamma}$  ratios for NGC 6946 indicate that we have *overestimated* the extinction in the inner parts of the galaxy. For NGC 300, we only have the  $\frac{\text{H}\alpha}{\text{Br}\gamma}$  ratio and it indicates that we may have a trend of *increasing* extinction with galactocentric distance. The  $\frac{\text{H}\alpha}{\text{Br}\gamma}$  ratio for NGC 628 indicates that we have overestimated the extinction throughout this galaxy. For NGC 1068, the  $\frac{\text{H}\alpha}{\text{H}\beta}$  and  $\frac{\text{Pa}\beta}{\text{Br}\gamma}$  ratios indicate an overestimate in extinction in the inner regions of the galaxy while the  $\frac{\text{H}\alpha}{\text{Br}\gamma}$  and  $\frac{\text{Pa}\beta}{\text{Br}\gamma}$  ratios indicate an *underestimate* in the inner regions of the galaxy. The three ratios for NGC 4725 each indicate different trends: the  $\frac{\text{H}\alpha}{\text{Pa}\beta}$  ratio indicates an *overestimate* throughout the galaxy, the  $\frac{\text{H}\alpha}{\text{Br}\gamma}$  ratio indicates an *underestimate* in the inner regions of the galaxy, and the  $\frac{\text{Pa}\beta}{\text{Br}\gamma}$  ratio indicates an *underestimate* in the inner regions of the galaxy. For NGC 3359, we have a similar conundrum with all three ratios indicating different and conflicting trends: the  $\frac{\text{H}\alpha}{\text{Pa}\beta}$  ratio indicates *underestimate* in the inner regions of the galaxy, the  $\frac{\text{H}\alpha}{\text{Br}\gamma}$  ratio indicates an underestimate throughout the galaxy,

and the  $\frac{\text{Pa}\beta}{\text{Br}\gamma}$  ratio indicates that the extinction *increases* with galactocentric distance. Finally, for NGC 4535 the only ratio, the  $\frac{\text{H}\alpha}{\text{Br}\gamma}$  ratio indicates that the extinction *decreases* with distance in this galaxy.

In Table 6.3, the second column indicates the number of regions evaluated, for reference. Columns (3) through (6) indicate values and trends of values of star formation rate with distance, where star formation rate is calculated using each of the four hydrogen recombination lines ( $\text{H}\beta$ ,  $\text{H}\alpha$ ,  $\text{Pa}\beta$  and  $\text{Br}\gamma$ ). We expect all trends of star formation to decrease with distance if we are primarily sampling regions of star formation. We see this trend in every galaxy in our sample. Low values for star formation rates are a result of undercorrection of the fluxes. Therefore, low values indicate underestimates in extinction; whereas, high values of star formation rate indicate overestimates in extinction.

In every casewhere we have  $\text{H}\beta$  data, the star formation rates calculated using those data give the highest values of any of the lines. In these three galaxies, judging from the emission line ratios in the analysis above, the extinction may have been overestimated. Such a scenario would cause an overcorrection to the  $\text{H}\beta$  flux and would result in a higher star formation rate value. Since  $\text{H}\beta$  is the line with the shortest wavelength, it is the most sensitive to errors in extinction estimates.

Column (7) of Table 6.3 lists the trends in color temperature as measured by the  $\frac{F_{60\ \mu\text{m}}}{F_{100\ \mu\text{m}}}$  ratio. We expect this ratio to decrease with galactocentric distance if the amount of dust decreases with distance, or if the amount of small dust grains decreases with distance. An increase with distance would indicate that either the amount of dust increases or the amount of small dust grains increases with distance. There were three cases where the hydrogen recombination line ratios indicate something about the trend of extinction with distance: NGC 300 - increasing with distance, NGC 3359 - increasing with distance and NGC 4535 - decreasing with distance. We see that for NGC 4535 and NGC 3359, the trends in color temperature match what

the line ratios indicate. However, for NGC 300, this is not the case; rather we see the opposite trend in color temperature. For this reason, we interpret the trend in color temperature for NGC 300 as a trend in small dust grain distribution. The wide range in values of the  $\frac{F_{60\ \mu m}}{F_{100\ \mu m}}$  ratio indicate that the dominant heating population is not correlated with color temperature, since every region in every galaxy is “very young” population dominated.

## CHAPTER 7 CONCLUSIONS

In this chapter we summarize the conclusions of our investigation of the source of the far infrared radiation in nearby spiral galaxies. We have analyzed eight nearly face-on, nearby spiral galaxies with the purpose of addressing the question: What stars heat the dust in normal spiral galaxies?

Our main conclusions are as follows:

- far infrared radiation traces star formation
- evaluation of extinction is essential for this kind of analysis if optical recombination lines of hydrogen (i.e.,  $H\alpha$ ) are used
- $Br\gamma$  is an excellent star formation indicator which, if used in place of  $H\alpha$  can obviate the need for extinction assessment
- color temperature *does not* trace dominant heating population

Our method of analysis has improved upon previous methods in the following ways:

- we used  $Br\gamma$  rather than  $H\alpha$  as a star formation indicator
- we evaluated the extinction for each region using several recombination lines of hydrogen
- we used different extinction laws to evaluate different stellar populations
- we used very recent stellar models which include an empirical analysis of stellar spectra for early type stars in the ultraviolet regime

- we enhanced the resolution of the *IRAS* HIRES images using PIXON image reconstruction

The use of  $\text{Br}\gamma$  rather than  $\text{H}\alpha$  as a star formation indicator has not affected the outcome of our analysis. It is clear, however, that the use of  $\text{Br}\gamma$  as a tracer of the “very young” population would matter if we had used a global extinction law (see Table 6.1).

The evaluation of the extinction for each region using several recombination lines of hydrogen has not been used before in this kind of analysis. Our results indicate that this analysis is essential to determining the dominant heating population consistently. This is evidenced by the fact that, when the extinction is evaluated for each region, the results do not change when the tracer of the “very young” population is changed. In our evaluation of the extinction for each region, the  $\text{Br}\gamma$  data provide a large baseline, making our calculations more accurate.

The use of the Cardelli Law for the “very young” population and the Calzetti Law for the “old” and “young” populations is a unique treatment of the problem for studies of this problem. While using the traditional method of using a single extinction law for the entire analysis process does not change our results, the treatment used here agrees best with observations.

The use of very recent stellar models is also significant. Other works which have used an energy balance approach have used the standard GISELL96 models (Bruzual & Charlot 1993). Our population models are from the STARBURST99 software which include empirical data in the form of stellar spectra in the ultraviolet regime (Leitherer et al. 1999). The change in population models does influence our results. The GISELL96 models include a significant amount of ultraviolet radiation in the “old” population models that is not present in the STARBURST99 models. This is due to a difference in interpretation about the contribution of the red horizontal branch (a significant contributor to the “old” population, proportionally). It

is not yet clear which interpretation is correct. If we redo the analysis using the GISELL96 models instead of the STARBURST99 models, our results are the same unless we use the GISELL96 models and the traditional single extinction law. Of course, if we use the GISELL96 models and a global extinction law, we also see a variation in our results from galaxy to galaxy.

Finally, we enhanced the resolution of the *IRAS* HIRES images using PIXON image reconstruction. The enhancement allowed us to analyze more regions than we would have been able to distinguish otherwise. Clearly, in order to really understand the heating source of the far infrared radiation, high resolution far infrared data is needed. Our use of PIXON image reconstruction does not affect the outcome of our analysis for individual regions, but it allows us to evaluate smaller regions over which we are more confident that our assumptions hold true.

Our data indicate that we have correctly assessed and evaluated this problem. One way to see this is in the luminosity function plots in Chapter 5. The luminosity function show that in most cases we have achieved the depth needed in  $\text{Br}\gamma$  to ensure detection of all  $\text{H}\alpha$  sources. In cases where our depth may have been too shallow, we still arrive at conclusions such that our results agree with those of others.

In addition, it is noteworthy that there are many more studies which agree with our findings for the galaxies in our sample than those which contradict them. For half our sample, there are no previous studies which disagree with our conclusions.

### 7.1 Possible Sources of Error and Bias

In the search for possible sources of error, we must examine the assumptions made in this work. The main assumptions that we have made are

- case B recombination applies to all regions analyzed
- $\text{Br}\gamma$  and  $\text{H}\alpha$  are tracing *only* star formation
- the extinction we determine is applicable over the region to which it is applied



- the extinction can be calculated accurately from a minimum of one line ratio with a long baseline (namely, the  $\frac{H\alpha}{Br\gamma}$  ratio)
- the fraction of extinguished light which is reprocessed into far infrared radiation is the same for the different populations

The first assumption listed is a typical assumption. It is possible that case B recombination does not apply in some of the regions we analyze either because we are integrating over too large an area and are, therefore, including a considerable amount of diffuse ionized gas and shocked material. Such a scenario should not change the results of our analysis, since it would merely change the theoretical values for our flux ratios. The fact that our results are consistent from  $H\alpha$  to  $Br\gamma$  compels one to believe that the results are correct. If case B is not correct, it would probably explain the nonphysical ratios we observe in some regions.

The assumption that  $Br\gamma$  and  $H\alpha$  are tracing *only* star formation is also a typical assumption. It is a good assumption, usually, since these emission lines are associated with hot gas. In galaxies, typically, the  $Br\gamma$  and  $H\alpha$  emission which is not directly associated with ongoing star formation (i.e., supernova remnants, diffuse ionized gas) is not very significant.

The extinction determined for a given region is probably *not* applicable over the region to which it is applied. However, we are at a loss to come up with something better. Most likely, we are overestimating the extinction. Lacking the detail in the far infrared bands, it is unlikely that this problem can be resolved. In the end, however, it should not affect the outcome of our analysis since we use the same base extinction for all populations.

The extinction is probably *most* accurately calculated from a line ratio with a long wavelength baseline, like  $\frac{H\alpha}{Br\gamma}$ . More line ratios are preferable, but the  $\frac{H\alpha}{Br\gamma}$  ratio is a better choice than the  $\frac{H\alpha}{H\beta}$  ratio merely due to its longer wavelength baseline.

This is implicit in the theory behind the method of using emission lines to calculate extinction. The idea is to sample light at different points on the extinction curve to accurately assess the change in extinction from one point to the other. The greater the difference in wavelength, the better the assessment.

The last assumption, that the fraction of the extinguished light which is re-processed into far infrared radiation is the same for the different populations, is the hardest to assess. The problem, here, is that we know so little about the composition and size of the dust grains which produce far infrared light. If we are incorrect in this assumption, it could feasibly change our results. However, the most likely scenario is that if there is a bias, it would be towards the “very young” population since its contribution to the ultraviolet is considerably more than that of the “old” population (regardless of population model).

We conclude, therefore, that the possible biases and sources of error would not change the interpretation of our results. Most the possible biases we can think of would only push the interpretation more strongly in the direction it already is.

## 7.2 Improvements for Future Work

For future works in this area, we would recommend pushing further into the near infrared. Brackett Alpha ( $\text{Br}\alpha$ ,  $\lambda = 4.05 \mu\text{m}$ ) is a line that would be interesting to study. While it is observationally challenging, we feel that there may be great rewards in those data.

Of course, high resolution ( $< 1$  arcminute) far infrared data would be the best way to solve the problem since one would be able examine smaller regions and assess the contribution of the cirrus directly. Possibly, this will come from the future launch of the Space Infrared Telescope Facility (SIRTF) in 2006.

APPENDIX A  
NEAR INFRARED REDUCTION IMAGES

Dark Frame

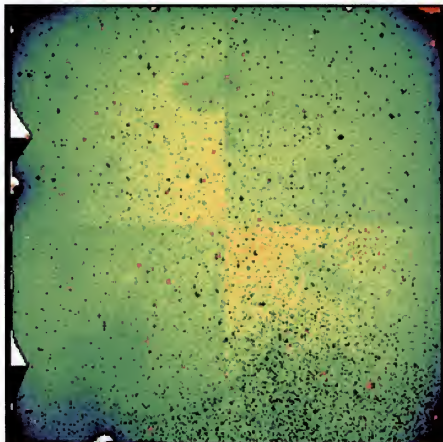


Figure A.1: A typical 100 second dark frame from the near infrared image sets. This image is taken with the dark slide in as described in Section 3.1.2.

Dark Mask Frame

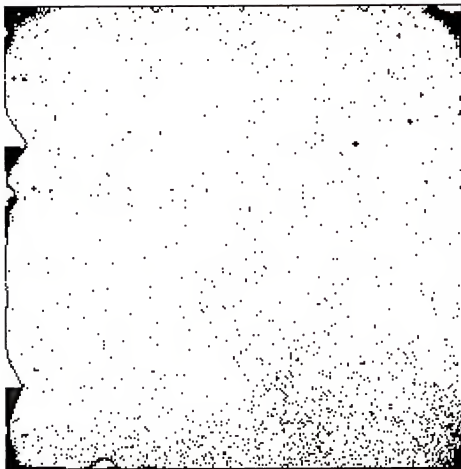


Figure A.2: A typical dark mask frame from the near infrared image sets. This image is formed by taking the dark image from the previous page and setting the bad pixels to a value of zero and the good pixels to one. This is done using the IRAF task `imreplace` as described in Section 3.1.5.

Flat Frame

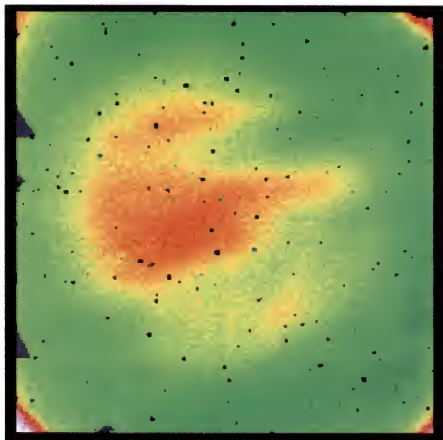


Figure A.3: A typical flat frame from the near infrared image sets. This image is created from the 16 off-source frames taken in a 32-frame cycle, as described in Section 3.1.3.

Flat Mask Frame

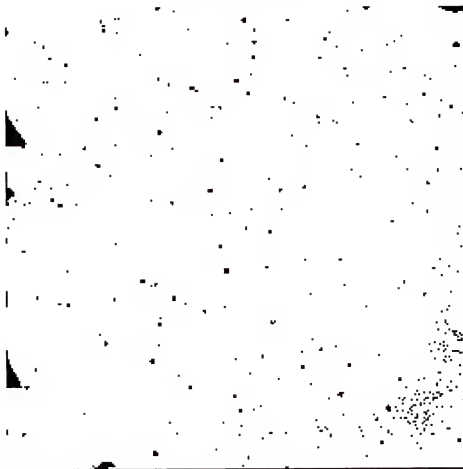


Figure A.4: A typical flat mask frame from the near infrared image sets. This image is formed by setting the bad pixels in the flat from the previous page to zero and the good pixels to one. This is done using the IRAF task `imreplace` as described in Section 3.1.5.

Mask Frame

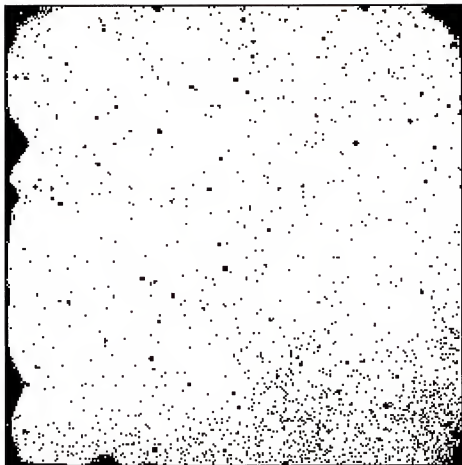


Figure A.5: A typical mask frame from the near infrared image sets. This mask is produced by multiplying the flat mask by the dark mask, as described in Section 3.1.5.

Sky Frame

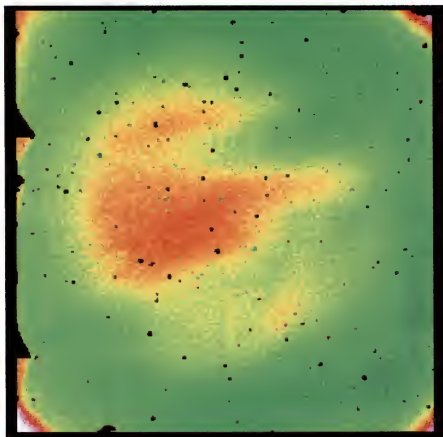


Figure A.6: A typical sky frame from the near infrared image sets. This images is formed from the four nearest off-source images, as described in Section 3.1.4.



Raw Frame

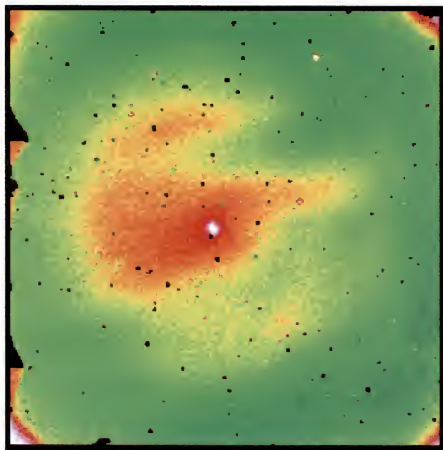


Figure A.7: A typical raw frame from the near infrared image sets.

Final Frame

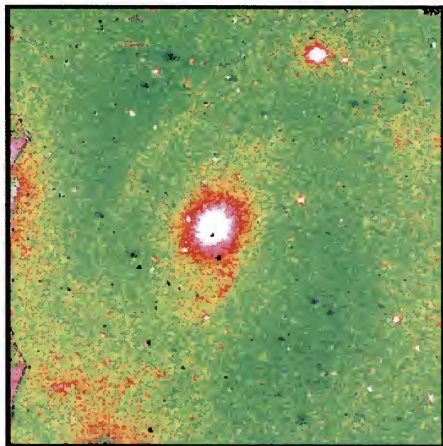


Figure A.8: A typical reduced frame from the near infrared image sets. This image is reduced as described in Section 3.1.

APPENDIX B  
OPTICAL REDUCTION IMAGES

Bias Frame



Figure B.1: A typical bias from the optical data sets, as described in Section 3.2.

Flat Frame

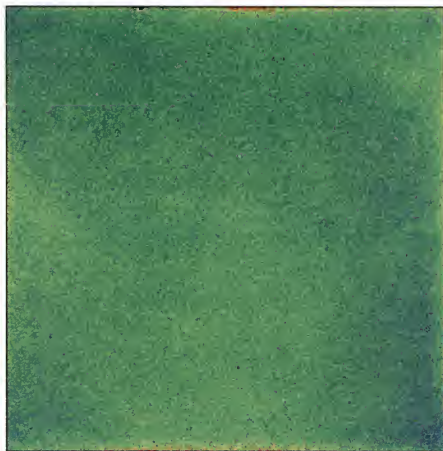


Figure B.2: A typical flat from the optical data sets, as described in Section 3.2.

Raw Frame

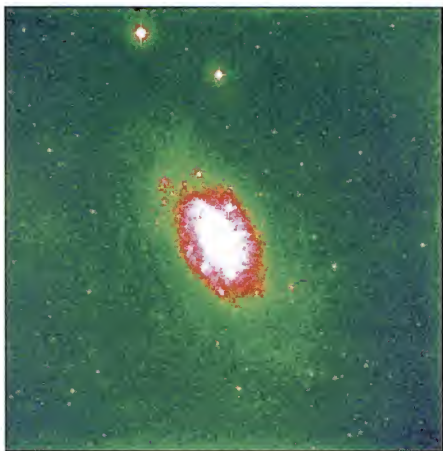


Figure B.3: A typical raw image from the optical data sets.

Final Frame

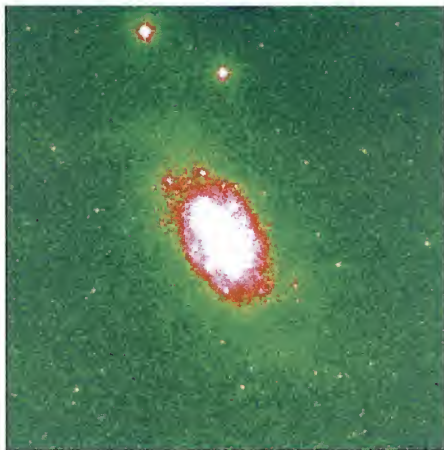


Figure B.4: A reduced image from the optical data sets, created as described in Section 3.2.

## APPENDIX C APERTURES

### Apertures for NGC 2403

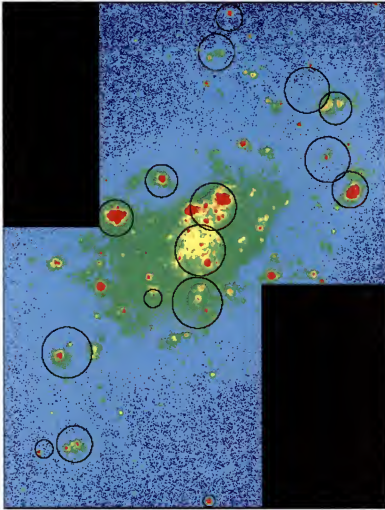
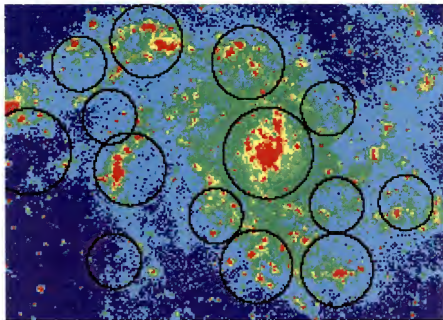
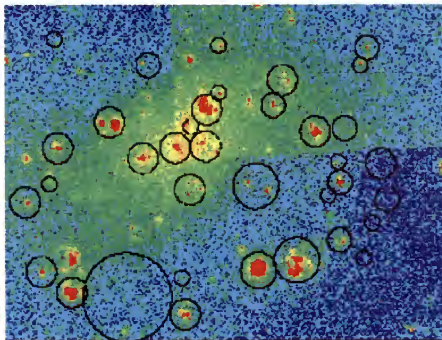


Figure C.1: These are the apertures for NGC 2403 overlaid on the  $H\alpha$  image.

Apertures for NGC 6946

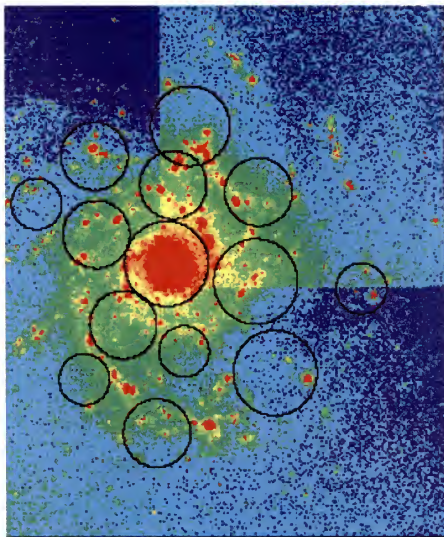
Figure C.2: These are the apertures for NGC 6946 overlaid on the H $\alpha$  image.

Apertures for NGC 300

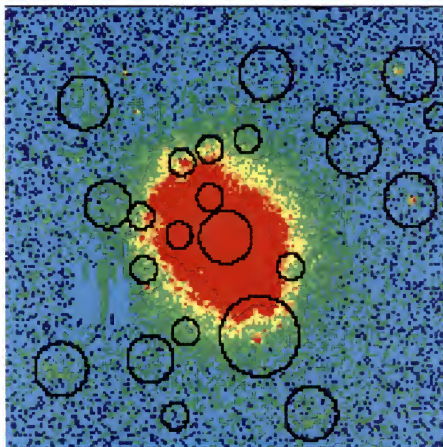
Figure C.3: These are the apertures for NGC 300 overlaid on the H $\alpha$  image.



Apertures for NGC 628

Figure C.4: These are the apertures for NGC 628 overlaid on the  $H\alpha$  image.

Apertures for NGC 1068

Figure C.5: These are the apertures for NGC 1068 overlaid on the  $H\alpha$  image.

Apertures for NGC 4725

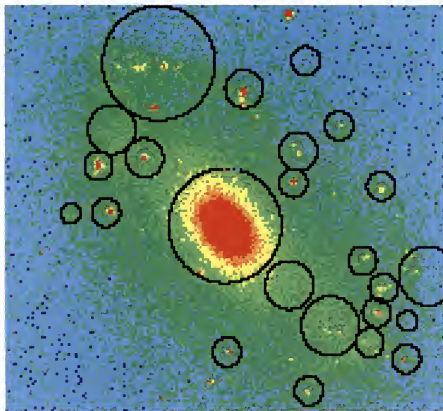


Figure C.6: These are the apertures for NGC 4725 overlaid on the H $\alpha$  image.

Apertures for NGC 3359

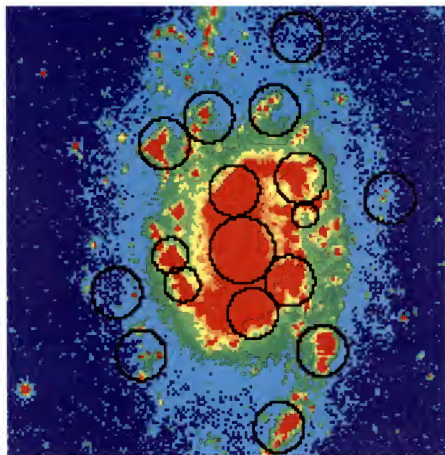


Figure C.7: These are the apertures for NGC 3359 overlaid on the  $H\alpha$  image.

Apertures for NGC 4535

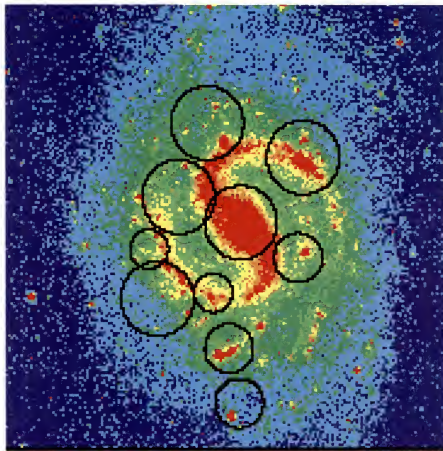


Figure C.8: These are the apertures for NGC 4535 overlaid on the  $H\alpha$  image.

## REFERENCES

- Aumann, H.H., Fowler, J.W., Melnyk, M. 1990. *Astronomical Journal*, **99**, 1674–1681.
- Baker, J.G., Menzel, D.H. 1938. *Astrophysical Journal*, **88**, 52–64.
- Bicay, M.D., Helou, G. 1990. *Astrophysical Journal*, **362**, 59–73.
- Bicay, M.D., Helou, G., Condon, J.J. 1988. *Astrophysical Journal Letters*, **338**, L53–L56.
- Bothun, G.D., Lonsdale, C.J., Rice, W. 1989. *Astrophysical Journal*, **341**, 129–150.
- Boulanger, F., Perault, M. 1988. *Astrophysical Journal*, **330**, 964–985.
- Bruzual, A.G., Charlot, S. 1993. *Astrophysical Journal*, **405**, 538–553.
- Calzetti, D., Armus, L., Bohlin, R.C., Kinney, A.L., Koornneef, J., Storchi-Bergmann, T. 2000. *Astrophysical Journal*, **533**, 682–695.
- Calzetti, D., Kinney, A.L., Storchi-Bergmann, T. 1996. *Astrophysical Journal*, **458**, 132–135.
- Caplan, J., Ye, T., Deharveng, L., Turtle, A.J., Kennicutt, R.C. 1996. *Astronomy and Astrophysics*, **307**, 403–416.
- Cardelli, J.A., Clayton, G.C., Mathis, J.S. 1989. *Astrophysical Journal*, **345**, 245–256.
- Chi, X., Wolfendale A.W. 1990. *Monthly Notices of the Royal Astronomical Society*, **245**, 101–107.
- Desert, F.-X., Boulanger, F., Puget, J.L. 1990. *Astronomy and Astrophysics*, **237**, 215–236.
- Devereux, N.A., Scowen, P.A. 1994. *Astronomical Journal*, **108**, 1244–1255.
- Devereux, N.A., Young, J.S. 1993. *Astronomical Journal*, **106**, 948–963.
- Elias, J.H., Frogel, J.A., Matthews, K., Neugebauer, G. 1982. *Astronomical Journal*, **87**, 1029–1034.
- Giovanelli, R., Haynes, M.P., Salzer, J.J., Wegner, G., da Costa, L.N., Freudling, W. 1995. *Astronomical Journal*, **110**, 1059–1070.
- Goldader, J.D., Joseph, R.D., Doyon, R., Sanders, D.B. 1997. *Astrophysical Journal*, **474**, 104–120.

- Gondhalekar, P.M., Phillips, A.P., Wilson, R. 1980. *Astronomy and Astrophysics*, **85**, 272–280.
- Hummer, D.G., Storey, P.J. 1987. *Monthly Notices of the Royal Astronomical Society*, **224**, 801–820.
- Israel, F.P., Kennicutt, R.C. 1980. *Astrophysical Letters*, **21**, 1–9.
- Jones, L.V., Keel, W.C. 2000. *Astronomical Journal*, submitted.
- Jones, L.V., Zasov, A.V. 1995. *Astronomical and Astrophysical Transactions*, **8**, 201.
- Joyce, R., Merrill, M. 1999. *The IRIM User's Manual*, Kitt Peak National Observatories, Tucson, AZ.
- Kennicutt, R.C. 1983. *Astrophysical Journal*, **272**, 54–67.
- Kurucz, R.L. 1996. *Model Atmospheres and Spectrum Synthesis ASP Conference Series*, **108**, ed. Adelman, S.J., Kupka, F., Weiss, W.W. p. 2.
- Leitherer, C., Schaerer, D., Goldader, J.D., Delgado, R.M.G., Robert, C., Kune, D.F., de Mello, D.F., Devost, D., Heckman, T.M. 1999. *Astrophysical Journal Supplement Series*, **123**, 3–40.
- Lonsdale Persson, C.J., Helou, G. 1987. *Astrophysical Journal*, **314**, 513–524.
- Low, F.J., Young, E., Beintema, D.A., Gautier, T.N., Beichman, C.A., Aumann, H.H., Gillett, F.C., Neugebauer, G., Boggess, N., Emerson, J.P. 1984. *Astrophysical Journal Letters*, **278**, L19–L22.
- Lu, N.Y., Helou, G., Tuffs, R., Xu, C., Malhotra, S., Werner, M.W., Thronson, H. 1996. *Astronomy and Astrophysics*, **315**, L153–L156.
- Mathis, J.S., Mezger, P.G., Panagia, N. 1983. *Astronomy and Astrophysics*, **128**, 212–229.
- Mezger, P.G., Mathis, J.S., Panagia, N. 1982. *Astronomy and Astrophysics*, **105**, 372–388.
- Petersen, L., Gammelgaard, P. 1996. *Astronomy and Astrophysics*, **308**, 49–54.
- Rieke, G. H., Lebofsky, M. J. 1979. *Annual Review of Astronomy and Astrophysics*, **17**, 477–511.
- Sanders, D.B., Scoville, N.Z., Young, J.S., Soifer, B.T., Schloerb, F.P., Rice, W.L., Danielson, G.E. 1986. *Astrophysical Journal Letters*, **305**, L45–L49.
- Scheffler, H., Elsässer, H. 1988. *Physics of the Galaxy and Interstellar Matter*, Springer-Verlag, Berlin-Heidelberg, p. 156.
- Sivan, J.-P., Maucherat, A.J., Petit, H., Comte, G. 1990. *Astronomy and Astrophysics*, **237**, 23–35.
- Solomon, P.M., Sage, L.J. 1988. *Astrophysical Journal*, **334**, 613–625.
- Stein, W.A., Soifer, B.T. 1983. *Annual Reviews of Astronomy and Astrophysics*, **21**, 177–207.

- Telesco, C.M., Dressel, L.L., Wolstencroft, R.D. 1993. *Astrophysical Journal*, **414**, 120–143.
- Telesco, C. M., Harper, D. A. 1980. *Astrophysical Journal*, **235**, 392–404.
- Walterbos, R.A.M., Greenawalt, B. 1996. *Astrophysical Journal*, **460**, 696–710.
- Walterbos, R.A.M., Schwing, P.B.W. 1987. *Astronomy and Astrophysics*, **180**, 27–49.
- Xu, C., Lisenfeld, U., Voelk, H.J. 1994. *Astronomy and Astrophysics*, **285**, 19–26.
- Young, J.S., Kenney, J., Lord, S.D., Schloerb, F.P. 1984. *Astrophysical Journal Letters*, **287**, L65–L68.
- Young, J.S., Xie, S. Kenney, J.D.P., Rice, W.L. 1989. *Astrophysical Journal Supplement Series*, **70**, 699–722.



## BIOGRAPHICAL SKETCH

My first experience with astronomy was on July 20, 1969, when Neil Armstrong and Buzz Aldrin landed on the moon. I was not fully aware of the experience, but my mother woke me from my nap, at the ripe old age of just 5 months, so that I could see it.

My first introduction to the field of astronomy was in Mr. Norton's 3rd grade class at Swarthmore Elementary School in 1977. We learned some northern constellations, the planets, and about how a solar eclipse happens. We also made pinhole cameras to view the solar eclipse that year. That year my parents gave me a small telescope which I used to view the moon.

The next encounter between myself and astronomy was in Mr. Stuppy's 8th grade science class at Swarthmore High School in 1981. He taught us all the constellations in the northern hemisphere. We also observed Venus through portable telescopes which he brought to our school one evening. The second half of that year, Dr. Dinero took over the class. That was when things got very interesting for me. He taught us about the planets and the stars. We learned the electromagnetic spectrum, stellar evolution, and the H-R Diagram; we even learned about galaxies and their morphological classifications.

Finally, in Mrs. Stanfield's 10th grade English class on career day in 1986, an astronomer had been invited to talk about astronomy as a career. Up until then, I thought astronomy could only be a hobby. When I found out that someone would

actually *pay* me to do what I loved most, I knew that was what I wanted to do. That day, I decided to chart the course I have since taken.

I went to Vassar College in 1987 for undergraduate school and majored in physics and astronomy (a double major). I spent every summer, including the first, as an undergraduate research assistant in astronomy. In the summer of 1988 I worked with Dr. Emilia Belserene at the Maria Mitchell Observatory in Nantucket, Massachusetts. The summer of 1989 I worked with Dr. Alan Harris at Jet Propulsion Laboratories in Pasadena, California. The summer of 1990, I worked with Dr. John Gaustad at Swarthmore College in Swarthmore, Pennsylvania. In my junior year of college, I went to the (then) Soviet Union as an exchange student for one year. I studied at Moscow State University in the physics Department with the astronomy group at the Sternberg Astronomical Institute. My advisors at Vassar College were Dr. Cindy Schwartz for physics and Dr. Deborah Elmegreen for astronomy.

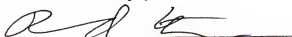
After graduating from Vassar College in 1991, with departmental honors in both physics and astronomy, I returned to the Soviet Union to pursue a master's degree in physics and mathematics with specialization in astronomy at Moscow State University and the Sternberg Astronomical Institute. There, I studied with Dr. Anatoly V. Zasov. I received awards from Vassar College for achievements in physics and astronomy. Also, I was awarded a Presidential scholarship to cover my travel to the Soviet Union for study there, in addition to a postgraduate scholarship which covered half of my tuition the first year at Moscow State University.

Following the completion of my degree at Moscow State University, I attended the University of Alabama pursuant of another master's degree in 1993. I worked with Dr. William Keel for my masters thesis. In my second year at Alabama, I worked at the Center for Communications and Education Technology under Jennifer Robinson. I wrote textbooks, created demonstrations, scripted telecasts, and wrote exams and teachers manuals for 6th, 7th and 8th grade Integrated Science.

Finally, I came to the University of Florida in 1995. I have worked with Dr. Richard Elston since October 1997 and he has been the best advisor. He has always been supportive and concerned about my well-being. He allowed me to be independent, as I wanted, and yet, he never let me feel that I wasn't getting enough attention from him. In the last year, since my grant ran out, he has been very supportive of me, encouraging me to attend meetings and contact people who may be important in my research. When he agreed to be my advisor, he insisted that he was not an expert in my field; however, in the years that I have worked with him, he has never left me hanging on a question. He has a breadth of knowledge of which I am envious and a depth which I can only hope to achieve one day. Dr. Elston has made my nine long years of graduate school worthwhile in the less than three years that we have worked together.

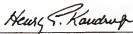
So, I have finally finished the work necessary to receive my PhD. I credit everyone I have mentioned here with helping me through the process, especially my mother for first introducing me to astronomy and then supporting me in my endeavors throughout my life. In the acknowledgements, I have mentioned others who supported me in nonacademic ways.

I certify that I have read this study and that in my opinion it conforms to acceptable standards of scholarly presentation and is fully adequate, in scope and quality, as a dissertation for the degree of Doctor of Philosophy.



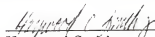
Richard J. Elston , Chairman  
Professor of Astronomy

I certify that I have read this study and that in my opinion it conforms to acceptable standards of scholarly presentation and is fully adequate, in scope and quality, as a dissertation for the degree of Doctor of Philosophy.



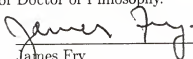
Henry E. Kandrup  
Professor of Astronomy

I certify that I have read this study and that in my opinion it conforms to acceptable standards of scholarly presentation and is fully adequate, in scope and quality, as a dissertation for the degree of Doctor of Philosophy.



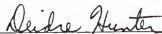
Haywood Smith  
Associate Professor of Astronomy

I certify that I have read this study and that in my opinion it conforms to acceptable standards of scholarly presentation and is fully adequate, in scope and quality, as a dissertation for the degree of Doctor of Philosophy.



James Fry  
Professor of Physics

I certify that I have read this study and that in my opinion it conforms to acceptable standards of scholarly presentation and is fully adequate, in scope and quality, as a dissertation for the degree of Doctor of Philosophy.



Deidre Hunter  
Astronomer, Lowell Observatory

This dissertation was submitted to the Graduate Faculty of the Department of Astronomy in the College of Liberal Arts and Sciences and to the Graduate School and was accepted as partial fulfillment of the requirements for the degree of Doctor of Philosophy.

May 2000



Dean, Graduate School